

Additive manufacturing of high-strength continuous fiber reinforced polymer composites

by

Pedram Parandoush

B.S., Central Tehran Azad University, 2011

M.S., University of Malaya, 2014

AN ABSTRACT OF A DISSERTATION

submitted in partial fulfillment of the requirements for the degree

DOCTOR OF PHILOSOPHY

Department of Industrial and Manufacturing Systems Engineering
Carl R. Ice College of Engineering

KANSAS STATE UNIVERSITY

Manhattan, Kansas

2019

Abstract

Additive manufacturing (AM), also referred to as 3D printing, of polymer-fiber composites has transformed AM into a robust manufacturing paradigm and enabled producing highly customized parts with significantly improved mechanical properties compared to un-reinforced polymers. 3D printing of continuous carbon fiber reinforced thermoplastics (CFRTP) composites is increasingly under development owing to its unparalleled flexibility of manufacturing 3D structures over traditional manufacturing processes. However, key issues, such as weak interlayer bonding, voids between beads and layers, and low volume ratio of carbon fiber, in the mainstream fused deposition modeling (FDM) and extrusion suppress the applications of these techniques in mission-critical applications, such as aerospace and defense industries. In this work, we proposed a new laser assisted AM method that utilizes prepreg composites with continuous fiber reinforcement as feedstock to fabricate 3D objects by implementing laser assisted bonding and laser cutting. This technique is inspired by laminated object manufacturing (LOM), for AM of continuous CFRTPs using prepreg composite sheets. AM of continuous glass and carbon fiber reinforced thermoplastic composites is demonstrated using this technique. The continuous fiber reinforced prepreg is laser cut and laser bonded layer upon layer to produce 3D composite objects. Microstructure and mechanical properties (strength, modulus, interfacial, and shear properties) of the additively manufactured continuous fiber composites are studied and compared to other additive and conventional manufacturing methods. The interlayer properties of these additively manufactured composites was superior to other AM technologies, resulting to an excellent mechanical properties relative to other AM techniques. The microstructure analysis, by micro computed tomography (CT) scans, scanning electron microscopy (SEM), and optical microscopy, showed low void content and full consolidation of prepreg layers. The temperature at the material

interface during the 3D process is crucial to achieve a strong bonding strength. This temperature can be predicted via the developed finite element (FE) heat transfer model in this work. This numerical model is able to predict the temperature history during the laser bonding process with great accuracy when compared to the experimental values. The surface quality of the additively manufactured CFRTPs were also studied and compared with the FDM technology. In addition, mechanical finishing methods, namely CNC milling and rotary ultrasonic machining (RUM), were employed to improve the surface quality of the 3D printed composites and drill precise holes in the structures. Overall, the proposed AM method can be broadly beneficial for industries requiring high performance and lightweight structural materials with complex geometries. This method is also easily scalable for high volume productions and could additionally reduce the waste associated with current CFRTP production techniques and improve the process from the production time standpoint by automation.

Additive manufacturing of high-strength continuous fiber reinforced polymer composites

by

Pedram Parandoush

B.S., Central Tehran Azad University, 2011

M.S., University of Malaya, 2014

A DISSERTATION

submitted in partial fulfillment of the requirements for the degree

DOCTOR OF PHILOSOPHY

Department of Industrial and Manufacturing Systems Engineering
Carl R. Ice College of Engineering

KANSAS STATE UNIVERSITY

Manhattan, Kansas

2019

Approved by:

Major Professor
Dr. Dong Lin

Copyright

© Pedram Parandoush 2019.

Abstract

Additive manufacturing (AM), also referred to as 3D printing, of polymer-fiber composites has transformed AM into a robust manufacturing paradigm and enabled producing highly customized parts with significantly improved mechanical properties compared to un-reinforced polymers. 3D printing of continuous carbon fiber reinforced thermoplastics (CFRTP) composites is increasingly under development owing to its unparalleled flexibility of manufacturing 3D structures over traditional manufacturing processes. However, key issues, such as weak interlayer bonding, voids between beads and layers, and low volume ratio of carbon fiber, in the mainstream fused deposition modeling (FDM) and extrusion suppress the applications of these techniques in mission-critical applications, such as aerospace and defense industries. In this work, we proposed a new laser assisted AM method that utilizes prepreg composites with continuous fiber reinforcement as feedstock to fabricate 3D objects by implementing laser assisted bonding and laser cutting. This technique is inspired by laminated object manufacturing (LOM), for AM of continuous CFRTPs using prepreg composite sheets. AM of continuous glass and carbon fiber reinforced thermoplastic composites is demonstrated using this technique. The continuous fiber reinforced prepreg is laser cut and laser bonded layer upon layer to produce 3D composite objects. Microstructure and mechanical properties (strength, modulus, interfacial, and shear properties) of the additively manufactured continuous fiber composites are studied and compared to other additive and conventional manufacturing methods. The interlayer properties of these additively manufactured composites was superior to other AM technologies, resulting to an excellent mechanical properties relative to other AM techniques. The microstructure analysis, by micro computed tomography (CT) scans, scanning electron microscopy (SEM), and optical microscopy, showed low void content and full consolidation of prepreg layers. The temperature at the material

interface during the 3D process is crucial to achieve a strong bonding strength. This temperature can be predicted via the developed finite element (FE) heat transfer model in this work. This numerical model is able to predict the temperature history during the laser bonding process with great accuracy when compared to the experimental values. The surface quality of the additively manufactured CFRTPs were also studied and compared with the FDM technology. In addition, mechanical finishing methods, namely CNC milling and rotary ultrasonic machining (RUM), were employed to improve the surface quality of the 3D printed composites and drill precise holes in the structures. Overall, the proposed AM method can be broadly beneficial for industries requiring high performance and lightweight structural materials with complex geometries. This method is also easily scalable for high volume productions and could additionally reduce the waste associated with current CFRTP production techniques and improve the process from the production time standpoint by automation.

Table of Contents

List of Figures	xi
List of Tables	xviii
Acknowledgements	xix
Dedication	xx
Chapter 1 - Introduction.....	1
References.....	3
Chapter 2 - Literature Review.....	5
Fused Deposition Modeling (FDM)	5
Laminated object manufacturing (LOM).....	8
Stereolithography (SL)	9
Extrusion.....	11
Selective laser sintering (SLS).....	12
Modeling and Analytical Techniques	13
Short Fiber Composite Theories	14
Classical Laminate Plate Theory (CLPT)	16
Finite Element Method (FEM).....	18
Final Remarks	19
References.....	21
Chapter 3 - Additive Manufacturing of Continuous Glass Fiber Thermoplastic Composites.....	30
Experimental	34
Materials	34
Laser assisted additive manufacturing	35
Characterization	37
Results and discussion	37
Cross-sectional microstructure.....	38
Bonding Strength	41
T-peel testing	42
Lap shear strength (LSS)	44
Mechanical properties.....	46

Tensile properties	46
Flexural properties	49
Overall picture	51
Conclusions.....	52
References.....	53
Chapter 4 - Additive manufacturing of High Strength Carbon Fiber Composites	58
Experimental.....	64
Materials	64
Laser Assisted 3D printing.....	64
Characterization	64
Microstructure.....	67
Mechanical Properties.....	69
Finite Element Simulation	75
Practical Applications	84
Conclusions.....	86
References.....	88
Chapter 5 - Finishing Operation for Additively Manufactured Carbon Fiber Composites	93
Experimental.....	96
Materials	96
LA- LOM	97
FDM 3D Printing	98
CNC Machining	99
Rotary Ultrasonic Machining.....	100
Characterization	102
CNC Machining Results	103
Surface Roughness	104
LA-LOM Surface Morphology.....	107
FDM Surface Morphology.....	109
RUM Results.....	112
Cutting Force	112
Surface Morphology	116

Surface Roughness	122
Cutting Temperature	126
Conclusions.....	129
References.....	131
Chapter 6 - Conclusions.....	135
Appendix A - Additional Micro CT Scans for continuous carbon fiber reinforced PA6.....	138

List of Figures

Figure 3-1 3D schematic of the proposed additive manufacturing method.....	36
Figure 3-2 Camera pictures of the laser assisted AM setup.....	36
Figure 3-3 Optical microscope pictures of (a) bidirectional and (b) unidirectional GF/PP prepreg tapes before laser assisted AM, demonstrating the thickness and fiber orientation difference in them.	38
Figure 3-4 Bonding mechanism in laser assisted bonding of PP matrix	39
Figure 3-5 Cross-sectional SEM images of unidirectional samples demonstrating interfacial bonding after laser assisted additive manufacturing. (a) cross-ply fiber orientation (0/90) evident from cross-sectional micrograph, (b, c) interfacial area between two layers with 90° angle of fiber orientation, and (d) fibers in unidirectional tape.	40
Figure 3-6 Cross-sectional SEM images of bidirectional samples demonstrating interfacial bonding after laser assisted additive manufacturing. (a) Cross section of the sample showing bonding structure of two tapes, (b, c) interfacial area between two tapes, and (d) fiber orientation and distribution in the bidirectional tape.	41
Figure 3-7 T-Peel test results and configuration using various laser powers and roller speeds for laser assisted AM parts; (a, b) the effect of laser power on peel strength of (a) unidirectional and (b) bidirectional samples; (c, d) the effect of roller speed on peel strength of (c) unidirectional and (d) bidirectional samples.	43
Figure 3-8 SEM images of T-peel test surface after adhesive failure. (a, b) The pulled out fibers from the surface resulted from T-peel test and (c, d) the thermoplastic matrix adhesive failure.	44
Figure 3-9 Lap shear strength of the laser bonded prepreg as a function of (a) laser power and (b) roller speed as compared with compression moulding [40].	46
Figure 3-10 Tensile bars used for tensile strength measurement prepared with bidirectional and unidirectional prepreg tapes.	47
Figure 3-11 Tensile properties of 3D printed samples fabricated by our proposed method. (a) Stress-strain curve showing the ultimate tensile strength of 3D printed samples, and (b) tensile modulus versus strength in comparison with FDM (SF) [14], compression molding	

(SF) [14], continuous GF compression molding and stamped [2], injection molding with SF and LF [3], FDM (ABS/CF-carbon) [42], and FDM (PLA/CF-carbon) [26].	49
Figure 3-12 Cross-sectional microstructure of the tensile fracture surface: (a) bidirectional prepreg and (b) unidirectional prepreg.	49
Figure 3-13 Flexural properties obtained from 3-point bending test. (a) Flexural stress-strain curve indicating flexural strength, and (b) comparison of flexural strength and modulus of our method (using unidirectional and bidirectional prepregs) with compression molding (CF-glass) [2], stamping (CF-glass) [2], injection molding (LF-glass) [3], FDM (ABS/CF-carbon) [42], and FDM (PLA/CF-carbon) [28].	51
Figure 4-1 Schematic illustration of the laser assisted 3D printing for carbon fiber reinforced thermoplastic composites. a) Laser cutting of prepreg composite sheet using a focused CO ₂ laser beam based on the sliced shape. b) Adding the pre-cut layer on top of the previous printed layers. c) Laser assisted bonding of composite prepreg sheets using a tilted CO ₂ laser beam and a consolidation roller. High temperature above the resin melting point from the laser irradiation and pressure from the consolidation roller causes full consolidation of the prepreg layers. d) Optical picture of final 3D laminated structures produced by 3D printing (scale bar: 10 mm). e) DSC curves of polyamide 6 PA6/CF and polypropylene /GF prepreg composite sheets used in our 3D printing method.	62
Figure 4-2 Lap shear strength for the test laser bonded unidirectional carbon fiber laminates. 5 samples with similar condition were tested.	63
Figure 4-3 Fracture surface of the lap shear test samples	63
Figure 4-4 Some of the tensile bars used for tensile testing (scale bar: 14 mm).	66
Figure 4-5 Some of the flex bars used for 3-point bending testing (scale bar: 10 mm)	66
Figure 4-6 Overall layout and dimensions of the ASTM D5868 lap shear test specimens	67
Figure 4-7 Optical image of lap shear test samples (Scale bar: 25 mm)	67
Figure 4-8 Micro CT scans of the 3D printed CFRTPs with various fiber orientations, namely, a) unidirectional [0] _s , b) cross-ply [0/90] _s , c) [0/-45/0/45] _s , and d) unidirectional with both GF and CF. The continuous carbon fiber reinforcement can be achieved in any desired angle at any given layer. The insets show the cross sectional slices of the CT scans and demonstrate the fiber orientation in 3D printed composite structure.	69

Figure 4-9 Tensile properties of the 3D printed carbon fiber composites. a) Representative tensile stress versus strain curves for 3D printed tensile bars of varying fiber materials and alignments. d) Property space map of tensile modulus versus tensile strength that compare our 3D printed CFRTP with other CF reinforced polymer 3D printing methods, namely, FDM [6-8, 16, 18], extrusion [12], SLS [12, 35], inkjet [12], and SLA [12, 36, 37]. Tensile fracture surface of the tensile bars with b) unidirectional $[0]_s$, c) cross-ply $[0/90]_s$, and e) $[0/-45/0/45]_s$ with CF reinforcement. f) Tensile fracture surface of a multi material tensile bar with unidirectional $[0]_s$ glass and carbon fiber reinforcement. The inset in (b) shows the fiber pullout resulted from the tensile test. Scale bars are 30 μm for (b), (c), (e), and (f). The scale bar for the inset in (b) is 5 μm 72

Figure 4-10 Flexural properties of the 3D printed CFRTP flex bars. a) Typical flexural stress versus strain curves from 3-point bending test of flex bars with varying fiber alignments. b) Property space map of flexural modulus versus flexural strength in comparison with CFRTPs fabricated by FDM [16, 17] and SLS [14, 35]. 74

Figure 4-11 SEM images from sides of the flex bars after 3-point bending test for (a) unidirectional, (b) cross-ply, (c) $[0/-45/0/45]_s$, and (d) unidirectional G-CF laminates (Scale bar: 1 mm)..... 75

Figure 4-12 Meshed geometry used in COMSOL simulation 77

Figure 4-13 Elliptical Gaussian boundary heat source 78

Figure 4-14 (a) Transverse and (b) longitudinal temperature dependent thermal conductivity of PA6/CF 78

Figure 4-15 Heat transfer analysis of the CFRP laser assisted bonding process using FE simulations. a) Temperature distribution in the CFRP laminate during the laser bonding process computed from the FE simulation. Isothermal contours show the temperature profile in the entire geometry; the temperature distribution on the top surface, 1st, 2nd, and 3rd interface are presented due to their importance in the consolidation process. The temperature at the 1st interface is well above the PA6's melting point (220 °C). The image from thermal IR camera shows the experimental temperature distribution on the top surface. b) Comparison of the temperature history obtained by thermocouples during the experiment with FE simulation at 1st, 2nd, and 3rd interface. c) Schematics of the thermal sensor locations for the experimental temperature measurements..... 80

Figure 4-16 The temperature profile obtained from FE simulations at the cross section for various process parameters, namely, (a) P=25 W, v=6 mm/s, (b) P=29 W, v=6 mm/s, (c) P=25 W, v=12 mm/s, (d) P=29 W, v=12 mm/s, (e) P=25 W, v=18 mm/s, and (f) P=29 W, v=18mm/s.....	82
Figure 4-17 The experimental temperature history obtained from thermocouples, at interface 1-3, for the laser powers of (a) 25 W and (b) 29 W.	83
Figure 4-18 The comparison of maximum temperature at interface 1-3 between the FE simulations and experimental results for the laser powers of (a) 25 W and (b) 29 W.....	84
Figure 4-19 Some practical implications of the developed additive manufacturing technique. The 3D printed CFRTP structure with [0/-45/0/45°] _s fiber orientation can support the weight of P. Parandoush in both a) axial and b) transverse direction. This strength is enabled by having a variety of continuous fiber reinforcement directions and exceptional interfacial bonding. c) This 3D printing methods method was also used to print the chassis of a remote control car. d) The printed under body of the car was replaced the original Aluminum parts without sacrificing the rigidity of the structure.....	85
Figure 5-1 Schematic of the LA-LOM process for each layer: a) laser cutting of the prepreg CFRP sheets, b) adding the pre-cut cross section on top of the previous layers, and c) laser assisted bonding of the prepreg CFRP layer using a laser beam and a consolidation roller.	98
Figure 5-2 The Markforged FDM 3D printer used for CFRP fabrication showing the 3d printing configuration. The printing head consists of two nozzles, one for continuous carbon fiber and one for nylon composite filament.....	99
Figure 5-3 The CNC milling machine used for finishing the 3D printed CFRP composites.	100
Figure 5-4 Schematic of the RUM of the fabricated CFRP plate with LA-LOM and FDM showing the RUM tool and cutting mechanism.....	101
Figure 5-5 RUM experimental setup	102
Figure 5-6 Surface roughness of the 3D printed CFRPs before and after finishing with varying cutting depths. Surface roughness of the horizontal and vertical surfaces for a) LA-LOM and b) FDM method is presented.....	105
Figure 5-7 The surface morphology of the original and finished horizontal surfaces for LA-LOM structures. 3D surface profiles of the a) original unfinished surface and finished surfaces	

with b) 0.4 mm and c) 0.8 mm cutting depth. Microscopic images of d) the unfinished surface and finished surfaces with e) 0.4 mm and f) 0.8 mm cutting depth	108
Figure 5-8 The surface morphology of the original and finished vertical surfaces for LA-LOM structures. 3D surface profiles of the a) original unfinished surface and finished surfaces with b) 0.4 mm and c) 0.8 mm cutting depth. Microscopic images of d) the unfinished surface and finished surfaces with e) 0.4 mm and f) 0.8 mm cutting depth.	109
Figure 5-9 The surface morphology of the original and finished horizontal surfaces for FDM structures. 3D surface profiles of the a) original unfinished surface and finished surfaces with b) 0.4 mm and c) 0.8 mm cutting depth. Microscopic images of d) the unfinished surface and finished surfaces with e) 0.4 mm and f) 0.8 mm cutting depth	110
Figure 5-10 The surface morphology of the original and finished vertical surfaces for FDM structures. 3D surface profiles of the a) original unfinished surface and finished surfaces with b) 0.4 mm and c) 0.8 mm cutting depth. Microscopic images of d) the unfinished surface and finished surfaces with e) 0.4 mm and f) 0.8 mm cutting depth	111
Figure 5-11 The effect of RUM machining conditions, namely, a) feedrate, b) tool rotation speed, and c) ultrasonic power, on the maximum cutting force.....	115
Figure 5-12 The digital photographs and SEM micrographs of the drilled holes in the LA-LOM parts for various feedrates. The optical images of the enter and exit surfaces of drilled holes for FRs of a) 0.02, f) 0.04, and l) 0.06 mm/s. The SEM micrograph of the surface morphology for the FRs of b, c, d, e) 0.02, g, h, i, k) 0.04, m, n, o, p) 0.06 mm/s. The scale bar in b, g, and m are 1 mm and the scale bar in the rest of SEM images are 200 μ m.....	116
Figure 5-13 The digital photographs and SEM micrographs of the drilled holes in the FDM parts for various feedrates. The optical images of the enter and exit surfaces of drilled holes for FRs of a) 0.02, f) 0.04, and l) 0.06 mm/s. The SEM micrograph of the surface morphology for the FRs of b, c, d, e) 0.02, g, h, i, k) 0.04, m, n, o, p) 0.06 mm/s. The scale bar in b, g, and m are 1 mm and the scale bar in the rest of SEM images are 200 μ m.	117
Figure 5-14 The digital photographs and SEM micrographs of the drilled holes in the LA-LOM parts for various tool rotation speeds. The optical images of the enter and exit surfaces of drilled holes for TRSs of a) 2000, f) 4000, and l) 6000 rpm. The SEM micrograph of the surface morphology for the TRSs of b, c, d, e) 2000, g, h, i, k) 4000, m, n, o, p) 6000 rpm.	

The scale bar in b, g, and m are 1 mm and the scale bar in the rest of SEM images are 200 μm	118
Figure 5-15 The digital photographs and SEM micrographs of the drilled holes in the FDM parts for various tool rotation speeds. The optical images of the enter and exit surfaces of drilled holes for TRSs of a) 2000, f) 4000, and l) 6000 rpm. The SEM micrograph of the surface morphology for TRSs of b, c, d, e) 2000, g, h, i, k) 4000, m, n, o, p) 6000 rpm. The scale bar in b, g, and m are 1 mm and the scale bar in the rest of SEM images are 200 μm	119
Figure 5-16 The digital photographs and SEM micrographs of the drilled holes in the LA-LOM parts for various ultrasonic powers. The optical images of the enter and exit surfaces of drilled holes for UPs of a) 20, f) 40, and l) 60 %. The SEM micrograph of the surface morphology for the UPs of b, c, d, e) 20, g, h, i, k) 40, m, n, o, p) 60 %. The scale bar in b, g, and m are 1 mm and the scale bar in the rest of SEM images are 200 μm	120
Figure 5-17 The digital photographs and SEM micrographs of the drilled holes in the FDM parts for various ultrasonic powers. The optical images of the enter and exit surfaces of drilled holes for UPs of a) 20, f) 40, and l) 60 %. The SEM micrograph of the surface morphology for the UPs of b, c, d, e) 20, g, h, i, k) 40, m, n, o, p) 60 %. The scale bar in b, g, and m are 1 mm and the scale bar in the rest of SEM images are 200 μm	121
Figure 5-18 3D surface profile and the corresponding surface roughness of the RUM surface for LA-LOM CRFP plates using experimental conditions a) 1, b) 2, c) 3, d) 4, e) 5, f) 6, and g) 7.	123
Figure 5-19 3D surface profile and the corresponding surface roughness of the RUM surface for FDM CRFP plates using experimental conditions a) 1, b) 2, c) 3, d) 4, e) 5, f) 6, and g) 7.	124
Figure 5-20 The influence of machining conditions, namely, a) feedrate, b) tool rotation speed, and c) ultrasonic power, on the average surface roughness of the drill holes.....	125
Figure 5-21 The influence of RUM machining conditions, namely, a) feedrate, b) tool rotation speed, and c) ultrasonic power, on the increased temperature during the RUM process. Temperature increment is defined as the temperature difference between the starting point and the highest temperature occurred during RUM process.	127

Figure 5-22 The thermal images of the highest temperature (°C) occurred during the RUM of LA-LOM parts for conditions a) 1, b) 2, c) 3, d) 4, e) 5, f) 6, and g) 7, acquired from FLIR thermal camera.....	128
Figure 5-23 The thermal images of the occurred highest temperature (°C) occurred during the RUM of FDM parts for conditions a) 1, b) 2, c) 3, d) 4, e) 5, f) 6, and g) 7, acquired from FLIR thermal camera.	129
Figure A-1 3D illustration of continuous fiber reinforcement in the 3D printed unidirectional CFRTPs.....	138
Figure A-2 Cross sectional CT scan of the 3D printed unidirectional CRTPs	138
Figure A-3 3D illustration of continuous fiber reinforcement in the 3D printed cross-ply CFRTPs	139
Figure A-4 Cross sectional CT scan of the 3D printed cross-ply CFRTP	139
Figure A-5 3D illustration of continuous fiber reinforcement in the 3D printed [0/-45/0/45] _s CFRTPs.....	140
Figure A-6 Cross sectional CT scan of the 3D printed [0/-45/0/45] _s CFRTPs.....	140
Figure A-7 3D illustration of continuous fiber reinforcement in the G-CF samples.....	141
Figure A-8 Cross sectional CT scan of the G-CF samples	141

List of Tables

Table 3-1 Mechanical properties of continuous GF/PP by laser assisted AM compared with pure PP manufactured by compression molding.....	52
Table 4-1 Material properties and COMSOL parameters used in the heat transfer simulations ..	79
Table 5-1 The varying cutting depths used in the experimental study.	104
Table 5-2 RUM experimental conditions	112

Acknowledgements

I wish to thank all the professors and students who helped me to conduct this research. Special thanks to my academic advisor, Dr. Dong Lin, for believing in me, giving me ideas, and guiding me through my PhD studies. Thanks to Palamandadige Kasun Fernando for major contributions in rotary ultrasonic machining experiments for Chapter 5. Thanks to Timothy Deines for performing the CNC machining experiments for Chapter 5. Thanks to Levi Tucker for helping me with the experiments for Chapters 3 and 4.

Dedication

I dedicate this dissertation to my father and my family for their continuous support. None of my success in life would be possible without their support.

Chapter 1 - Introduction

Additive manufacturing (AM), also known as 3D printing, is defined as a process of adding materials to fabricate objects from three-dimensional (3D) models in successive layers, versus traditional subtractive manufacturing methods. Numerous novel AM processes have been developed in more than 20 years of AM development with applications in aerospace, automotive, biomedical, digital art, architectural design, etc. [1]. There was an exponential increase in AM technologies in recent years and they continue to grow due to its versatility and low cost for rapid prototyping and manufacturing applications. All these features combined with AM's customizability to fabricate complex monolithic structures and geometries, with micrometer resolution helped AM grow to a multibillion-dollar industry [2, 3].

To date, the dominant part of 3D printing industry immensely has relied on single material printing. This issue paired with limited choice of available resins compatible with commercial printers severely limited variations in the physical and chemical properties of 3D printed objects. This limitation led to development of multi-material printers with partial control on material composition and properties, offering layered composite materials. Furthermore, multiple printing heads allowed printing blended composites with functional and variable features. 3D printing of fiber reinforced composites is currently conducted by stereolithography (SL), laminated object manufacturing (LOM), fused deposition modeling (FDM), selective laser sintering (SLS), and extrusion. It is one of the hottest topics in the field of additive manufacturing and under intense attention and offers significant improvement in mechanical properties, however, it requires a complex procedure to be manufactured and is difficult to be incorporated into processing.

Implementing the traditional methods of composite manufacturing in AM is not practical and new technologies are needed to assist with the development of new AM methods [4].

The advances in development of composite 3D printers have not prevented development in pre-blended materials with fillers such as nanoparticles, carbon nanotubes, fibers and graphene in order to achieve unique characteristics and capabilities [5]. Fiber reinforcement, in particular, appears to be an attractive filler to improve the properties of polymers. Pre-blended materials using discontinuous fibers as additive have been under intensive investigation as a good alternative to multi-head printers with complex and costly designs. These additive based materials exhibit unique characteristics and capabilities, depending on the additive used. Suitable mechanical, electrical, or thermal properties can be accomplished in an inexpensive manner.

Polymers amongst other materials have been in the center of attention due to ease of production and availability. 3D printing industry primarily involves with polymers in various forms such as, reactive, liquid solutions, or thermoplastic melts [6, 7]. These benefits joined by enhancements from fiber reinforcement offer a favorable combination for future development of AM technologies. In addition, almost all of the existing AM methods can be benefited from fiber reinforcement.

Although fiber reinforcement in 3D printing sounds promising, there are numerous issues needed to be resolved, namely the effect of fibers on resolution, agglomerate formation, heterogeneous composite formation, blockage of printer heads, and non-adhesion and increased curing times [5]. The objective of this research is to address the issue with current composite AM technologies by implementing a novel AM technique. The main target of this dissertation is to improve the mechanical properties of the additively manufactured fiber reinforced polymer composites by incorporating new AM processes into composite manufacturing. This improvement

is achievable by enhancing interlayer bonding of additively manufactured continuous fiber reinforced composites. This dissertation is consist of 6 chapters. Chapter 1 is an introduction to AM of fiber reinforced polymer composites followed by chapter 2 which discusses current state of the art of AM techniques capable of producing fiber-polymer composites. In chapter 3, a novel method is introduced for AM of continuous glass fiber reinforced polymers and characterization of the produced composites. Chapter 4 discusses AM of continuous carbon fiber reinforced polymers, characterization of additively manufactured carbon fiber composites, and finite element (FE) modeling of the process. Chapter 5 presents finishing processes for the composites produced via our AM technology. Finally, conclusions of this dissertation and research findings are presented in chapter 6.

References

- [1] N. Guo and M. C. Leu, "Additive manufacturing: technology, applications and research needs," *Frontiers of Mechanical Engineering*, journal article vol. 8, no. 3, pp. 215-243, 2013, doi: 10.1007/s11465-013-0248-8.
- [2] T. J. Horn and O. L. A. Harrysson, "Overview of current additive manufacturing technologies and selected applications," (in English), *Sci. Prog.*, Report vol. 95, p. 255+, 2012. [Online]. Available: <http://go.galegroup.com/ps/i.do?id=GALE%7CA306753585&v=2.1&u=ksu&it=r&p=ONE&sw=w&asid=df22f7ab4e5ffd044649fa8ee9daf4e0>.
- [3] K. V. Wong and A. Hernandez, "A Review of Additive Manufacturing," *ISRN Mechanical Engineering*, vol. 2012, p. 10, 2012, Art no. 208760, doi: 10.5402/2012/208760.
- [4] S. Kumar and J.-P. Kruth, "Composites by rapid prototyping technology," *Materials & Design*, vol. 31, no. 2, pp. 850-856, 2010.
- [5] U. Kalsoom, P. N. Nesterenko, and B. Paull, "Recent developments in 3D printable composite materials," *RSC Advances*, vol. 6, no. 65, pp. 60355-60371, 2016.
- [6] D. D. Gu, W. Meiners, K. Wissenbach, and R. Poprawe, "Laser additive manufacturing of metallic components: materials, processes and mechanisms," *Int. Mater. Rev.*, vol. 57, no. 3, pp. 133-164, 2012, doi: 10.1179/1743280411Y.0000000014.

- [7] M. Hofmann, "3D printing gets a boost and opportunities with polymer materials," *ACS Macro Letters*, vol. 3, no. 4, pp. 382-386, 2014.

Chapter 2 - Literature Review

Fiber reinforcement can greatly improve the properties of 3D printed parts with polymer matrix. Fiber orientation and void fraction of composites are main concern in 3D printing of these composites. Most of the commercially available 3D printing techniques would benefit from fiber reinforcement. In this section, all these techniques for 3D printing of polymer-fiber composites are reviewed in detail to demonstrate their strength and weakness in additive manufacturing of polymer-fiber composites. These methods are fused deposition modeling (FDM), laminated object manufacturing (LOM), stereolithography (SL), extrusion, and selected laser sintering (SLS). Fiber orientation and void fraction of composites are main concern in 3D printing of these composites. In this chapter, all these techniques for 3D printing of polymer-fiber composites are discussed in detail to demonstrate their strength and weakness in additive manufacturing of polymer-fiber composites. Potential methods for modelling and analysis of these 3D printed structures are also reviewed.

Fused Deposition Modeling (FDM)

FDM is currently the most applied AM technology, according to Wohler's Report from Stratasys, Inc. Commercial FDM machines held 41.5% of the market share with the total of 15,000 FDM machines sold by the end of 2010. The key elements of FDM system include material feed mechanism, liquefier, print head, gantry, and build surface [1]. Several process parameters are essential in FDM, including bead width, air gap, model build temperature, and raster orientation. The effect of raster orientation on tensile and compression test results have been investigated in detail [2]. The temperature distribution during FDM process can be monitored by IR camera [3]. The surface roughness and cross section shape of FDM fabricated parts are under intense study [4,

5]. Several building rules have been proposed to improve the strength and accuracy of the FDM printed parts, such as build parts to make sure tensile loads will be carried axially along printed directions, take care of the stress concentration at corners, use negative air gap to increase both strength and stiffness, consider that small bead width leading more building time and better surface quality, be aware the part accuracy affected by the build orientation, and realize that tensile loaded area tends to fail easier than compression loaded area [2].

Recently, fiber reinforcement in FDM has been very popular amongst the researchers. Most of the efforts were focused on development of filaments with short fibers additives. Inclusion of fibers in filament reduce tape swelling at the head during deposition and increase the stiffness [6]. Glass fiber reinforced polypropylene (PP) was evaluated by Carneiro, et al. [7] and showed 30% and 40% improvement for the modulus and strength, respectively, compared to pure PP. Vapor grown carbon fibers (VGCFs) and single wall carbon nanotubes (SWNTs) were compounded with acrylonitrile butadiene styrene (ABS) for FDM process. The VGCFs can be easily aligned by extrusion process. Tensile strength of 5 wt. % of VGCFs and SWNTs filled FDM parts increased 18% and 31%, respectively. However, the strain to failure of printed parts reinforced with VGCFs and SWNTs was dramatically decreased [8]. ABS containing oriented VGCFs and SWNTs exhibited modulus improvements up to 93% [9]. Thermotropic liquid crystalline polymers (TLCPs) with excellent tensile strength such as ABS and polypropylene (PP) were used in fiber reinforced FDM parts in order to overcome the drawbacks of low aspect ratio of fiber filled parts [10]. Processing temperature was one of the important parameters, which affects the surface morphology of TLCP and its mechanical behavior. The tensile modulus of 40 wt. % of TLCP filled ABS and PP was increased 100 % and 150 %, respectively. Higher carbon fiber ratio has a high maximum decomposition temperature thus providing high thermal stability. Ning, et al. [11]

evaluated the effect of weight ratio and length of carbon fiber on physical properties of FDM samples with ABS matrix. The 5 and 7.5 wt. % carbon fiber content showed the best improvement in tensile strength and Young's modulus, respectively. They have also concluded that longer carbon fibers can increase tensile strength and Young's modulus at the expense of toughness and ductility. Using aligned carbon fiber during FDM process, 30 wt. % CF-ABS composites showed great improvement in strength (~115%) and Young's modulus (~700%). These printed CF-ABS parts exhibit specific strength higher than Aluminum. The triangular channels between beads decreased by incorporating carbon fibers because of the reduced die-swell and increased thermal conductivity resulted from carbon fiber inclusion. However, inclusion of carbon fiber into the feedstock caused internal voids inside the beads responsible for stress concentration and failing at lower stresses. FDM samples exhibited significant pore formation with internal voids and the voids formed between the deposited beads during printing [12].

Continuous fiber reinforcement is currently one of the biggest challenges for researchers in 3D printing of polymer composites. It offers significant improvement in mechanical properties compared to discontinuous fibers, however, there is still no robust and standard paradigm developed for continuous fiber composites printing. Recently, Matsuzaki, et al. [13] developed an innovative technique for in-nozzle impregnation of continuous fiber and thermoplastic matrix. The resin filament and fiber were supplied separately before heating and mixing in the printing head. The mixture was then ejected to the printing bed. Carbon fibers and twisted yarns of natural jute fibers used as reinforcement. Namiki, et al. [14] implemented the same technique for printing polyactic acid (PLA)/carbon fiber composite parts. Some gaps were reported between PLA filaments which can be reduced by increasing the resolution. Tensile strength of continuous carbon fiber reinforced PLA prepared by FDM, as reported by Li, et al. [15], can reach up to 91 MPa

while in the case of short carbon fiber, it is only 68 MPa. Weak bonding between PLA and carbon fiber [16] can significantly affect the mechanical properties in this method, however, surface modification of carbon fiber bundle with methylene dichloride and PLA particles [15], improved adhesion and increased tensile and flexural strength. Tian, et al. [17] performed a systemic analysis on interface and performance of printed continuous carbon fiber reinforced PLA composites and the effect of process parameters on the temperature and pressure in the process. The demonstrated the capability of this method in 3D printing large curvatures without losing the continuous fiber reinforcement. Melenka, et al. [18] evaluated continuous Kevlar fiber-reinforced 3D printed Nylon structures using commercial desktop printers in order to predict the tensile properties. Stiffness and ultimate strength showed significant increase with high volume of fiber reinforcement. Carbon fibers were placed between layers of 3D printed polymer to improve strength and fatigue life and thermal treatment was performed to further increase the mechanical properties [19]. However, Van Der Klift, et al. [20] showed that increasing the number of layers of carbon fibers results in larger void areas which had negative effect on tensile strength. Impregnation of plastics into the fiber bundle could be achieved in the temperature range of 200-230 °C. Layer thickness of 0.4-0.6 mm and hatch spacing of about 0.6 mm guaranteed bonding strength between lines and layers. These parameters could achieve maximum flexural strength of 335 MPa and flexural modulus of 30 GPa.

Laminated object manufacturing (LOM)

In LOM, which was developed by Helisys of Torrance, CA and shipped in 1991, 3D parts are manufactured by cutting 2D cross-sections with laser or cutter and sequentially laminating the sheets. Paper, metals, plastics, fabrics, synthetic materials, and composites are amongst the

materials that can be used in LOM [21, 22]. Polymer matrix composites of C-shaped panel were directly fabricated by curved LOM [23]. A vacuum thermoforming apparatus was applied to bond commercial prepregs. The deviation of height direction was around 7.9% and the accuracy of most other directions was below 1%. The shear strength of fabricated composites was measured to be approximately 24.8 MPa, which was suggested by the authors that is acceptable for normal applications. LOM process was applied to print 3D parts of unidirectional and continuous glass fibers with 52-55 vol. % with epoxy matrix [24]. Decent interfacial bonding was shown by interlayer microstructures of LOM polymer composites. The major issue for LOM process was that the heat roller was not adequate for bringing parts to full consolidation and cure. It is helpful to increase the interface strength and reduce void contents to under 5% by a post consolidation cycle. Sonmez and Hahn [25] studied heat transfer and stress in LOM to understand the effect of process parameters on the resulting stress and temperature distributions. Large rollers were more favorable for bonding due to less concentrated stress distribution. One of the main advantages of LOM is ability to produce part with high strength, high modulus, low void content, and a strong inter layer interface. However, since the feedstock is in a form sheet, certain internal features cannot be produced as the excess material inside the part is challenging to be removed. In addition, in LOM sheets are needed for each layer and the extra unwanted material is not reusable contributing to an extra material waste.

Stereolithography (SL)

The 3D parts fabricated by SL exhibit weak mechanical properties, which hinders their further applications as functional components under loading conditions [26], however, adding fibers to the resin can increase the potential of SL in 3D printing functional components. Although,

continuous fiber is ideal for reinforcement, high weight ratio of short fibers can yield comparable results, but, their efficiency is limited due to fracture during mixing, random orientation, and uneven length [27].

Multi-wall carbon nanotubes (MWNTs) with low weight ratio were mixed in SL resin by mechanical mixing and ultrasonic dispersion [28]. The tensile strength (TS) and fracture strength (FS) were increased 5.7% and 26%, respectively, by adding 0.025 wt. % MWNTs. Carbon fiber has been successfully applied to reinforce polymers, however the primary issue for utilizing carbon fiber in SL is that it is opaque to the UV light and regions of the resin blocked by carbon fibers remains uncured by UV light. Various methods have been developed to avoid this drawback. Using glass fiber instead of carbon fiber can be beneficial for decreasing the opacity to UV light [27]. SL plus vacuum cast process was investigated to improve the tensile strength [26, 29]. Tensile samples produced by SL and polymer-glass fiber nonwoven-polymer sandwich structures were introduced by vacuum cast. It showed a significant increase of 36% in ultimate tensile strength and 11% increase in stiffness. The viscosity of the resin, especially at low shear rates, increased in the composite resins with significant volume fractions of fibers [30]. The surface coating of fibers can effectively reduce the viscosity, which is an advantage to allow processing of resins with higher fiber concentration. Laser scanning based SL was used to add 20 vol. % of short glass fibers (length: 1.6 mm and diameter: 15.8 μm) into acrylic based photo polymer [31]. Fiber filled composites represents a higher elastic modulus and ultimate tensile strength. The shrinkage of fiber reinforced composites was also observed to be lower than their non-reinforced counterparts. Dual polymerization scheme, including UV radiation and thermal treatments, was proposed to cure resins containing high volume ratio of carbon fibers [32]. It was estimated that one quarter of resin remains uncured, which was primarily inside carbon fibers. After an hour of thermal

treatment, the tensile strength was increased by 95%. Llewellyn-Jones, et al. [33] used ultrasonic manipulation to distribute glass microfibers in the resin. A variety of fiber orientation angles were achieved demonstrating versatility of the process. This method allows smart material fabrication such as resin-filled capsules for self-healing or piezoelectric particles for energy harvesting [34].

Extrusion

Extrusion, as one of the most recent developments in 3D printing, emerged to overcome the limitations of the FDM method with its versatility and cost-effectiveness. In this AM technique, layers of the material solution directly deposited (printed) in a volatile solvent to produce freeform 3D structures [35]. Lightweight cellular carbon fiber (10 μm diameter and 220 μm mean length, $l/d=22$) or SiC whiskers filled composites have been demonstrated by applying 3D extrusion printing method. Epoxy-based inks, which exhibited the desired viscoelasticity and long pot-life (30-day pot-life) in the absence and presence of highly anisotropic carbon fibers, were prepared. The authors claimed that shear induced alignment of fillers occurs along the printing direction. The SiC-filled and SiC/C filled transverse specimens showed a substantial increase in Young's modulus, over the pure resin from 2.66 ± 0.17 GPa to 10.61 ± 1.38 GPa and 8.06 ± 0.45 GPa, respectively. The longitudinal SiC filled and SiC/C filled specimens represent the increase of Young's modulus to 16.10 ± 0.03 GPa and 24.5 ± 0.83 GPa, respectively. Tensile strength of printed composites is comparable to the cast epoxy resin samples (71.1 ± 5.3 MPa), with longitudinal specimens exhibiting slight higher strength (96.6 ± 13.8 and 66.2 ± 6.1 MPa, for SiC-filled and SiC/C filled composites) than that the transverse specimens (69.8 ± 2.9 and 43.9 ± 4.1 MPa, for SiC-filled and SiC/C filled composites) [36]. PLA/MWNTs composite was used to fabricate conductive 3D

microstructures with arbitrary shapes as small as 100 μm with a method so called liquid deposition modeling [37].

Selective laser sintering (SLS)

Selective laser sintering (SLS) is a powder based AM process. The laser scans the powder bed layer by layer to form a 3D structure. It mainly deals with wax, ceramics [38-41], metals [40, 42-48] and polymers [49-54]. Major polymers used by SLS are including nylon, i.e. polyamide (PA) [51, 52, 54-59], (semi-) crystalline thermoplastics: polyethylene [60-62] (PE), PEEK [63], and PCL [64, 65]. SLS can be categorized in solid state sintering (SSS), liquid phase sintering-partial melting, full melting, and chemically induced binding. SSS is a thermal process that occurs at temperatures between $T_{Melt}/2$ and T_{Melt} , where T_{Melt} is the melting temperature. In liquid phase sintering-partial melting usually the binder material liquefied while structural material remains solid. Full melting technique, melt the powder entirely and exhibits properties comparable to those of bulk materials [66]. It can be applied to wide variety of materials, however, the long process time and preheating of powders is necessary.

CNT was added in Polyamide 12 (PA12) in order to improve the mechanical behaviors [51]. The laser sintered parts had 13% greater flexural modulus, 10.9% higher flexural strength, and 54% larger Young's modulus. The crystallization temperature of PA12-CNT powder was increased, which was responsible in hindering the movement of PA12 chains by the interfacial force between CNTs and PA12. However, the porosity also increased in the CNT composites. MWNTs were also mixed with PA 12 for the investigation of its effect on mechanical properties [52]. Goodridge, et al. [54] also confirmed enhancement in mechanical properties of PA12 with inclusion of CNT (3 wt. %) additives with 22% increase in storage modulus. High volume ratio of

carbon fibers (maximum 50%) was added into PA12 [53]. CNT-coated PA12 also improve heat conduction and heat absorption compared with pure PA12 in addition to the reinforcement on mechanical properties of the laser sintered polymeric composites [67]. Simulation results on laser sintering of PA12-CNT also suggested that inclusion of CNT helps the laser heat to conducted wider and deeper into the powder bed [68]

Uniform distribution of carbon fibers and good interfacial adhesion between fibers and matrix was achieved by pre-modification of carbon fibers through oxidation [53]. By adding the maximum weight ratio of carbon fibers, the flexural strength and flexural modulus were enhanced 114% and 243.4%, respectively. Glass beads used as additive in SLS of Nylon powders in order to determine mechanical properties as a function of material composition [69]. Zhu, et al. [70] proposed a novel method to prepare high-performance carbon fibers/PA12/epoxy ternary composites by infiltrating the porous green carbon fibers/PA12 parts built by SLS with high-performance thermosetting epoxy resin prior to curing the resin. The end result is a ternary composite system with novolac epoxy resin reinforced with carbon fibers coated with a thin 595nm layer of PA12. This method with 33% volume fraction of carbon fibers yielded an ultimate tensile strength of 101.03 MPa and a flexural strength of 153.43 MPa.

Modeling and Analytical Techniques

Polymer-fiber composites produced by AM can be analyzed using existing theory and methods based on the manufacturing technique, and reinforcement type. Existing macro and micro mechanical modelling techniques can be applied to AM with slight modifications. Microstructure of 3D printed parts often differ from those prepared by traditional manufacturing methods and

with the immersing of new AM methods, there is a demand for modelling and analysis of these structures.

Short Fiber Composite Theories

There are several theories for predicting the properties of short fiber composites. Depending on their assumptions they can be applied to various 3D printing methods. Fibers alignment, shape, length, and its bonding with matrix are crucial in accuracy of the modelling. The modified rule of mixtures (MROM) is the simplest method to predict the tensile properties of short fiber composites, by assuming perfect fiber –matrix interfacial bonding. MROM is given by [71, 72]

$$\sigma_{cu} = \chi_1 \chi_2 V_f \sigma_{fu} + V_m \sigma_m \quad (2-1)$$

where $\chi_1 \chi_2$ is fiber efficiency factor for the strength of the composite, in which, χ_1 and χ_2 are the fiber orientation and fiber length factors, respectively; σ_{cu} and σ_{fu} are ultimate strength of the composite and fiber, respectively; V_f and V_m represent the volume fraction of the fiber and matrix; and σ_m is the matrix stress at the composite failure. If the fiber length is equal to L and uniform, fiber orientation factor is equal to 1 and fiber length factor is given by [73],

$$\chi_2 = L/2L_c \text{ for } L < L_c \quad (2-2)$$

$$\chi_2 = 1 - L_c/2L \text{ for } L \geq L_c \quad (2-3)$$

where $L_c = r_f \sigma_{cu} / \tau_i$ is the critical fiber length, r_f is fiber radius, and τ_i is interfacial shear stress between matrix and fibers. In order to consider the effect of fiber orientation and non-uniform fiber length in the model, χ_1 and χ_2 should be modified. Modified Kelly and Tyson model proposed for fibers shorter and longer than the critical fiber length with considering fiber orientation, as follows [73, 74],

$$\sigma_{cu} = \chi_1 \left[\sum_{L_i=L_{min}}^{L_c} \frac{V_i \sigma_{fu} L_i}{2L_c} + \sum_{L_i=L_c}^{L_{max}} V_i \sigma_{fu} \left(1 - \frac{L_c}{2L_i}\right) \right] + V_m \sigma_m \quad (2-4)$$

However, fiber orientation factor χ_1 in this model is fitted empirically. Fu and Lauke [73] used two probability density functions for modelling the fiber length and fiber orientation distributions with the intention of predicting the elastic properties.

There are various theories for predicting the stiffness properties of short-fiber composites. Halpin and Tsai developed a famous theory for unidirectional short-fiber composites, in which, the longitudinal and transverse engineering moduli, E_{11} and E_{22} , are expressed in the general form of [75]

$$\frac{E}{E_m} = \frac{1 + \zeta \eta V_f}{1 - \eta V_f} \quad (2-5)$$

where E and E_m represent the Young's modulus of the composite and matrix, respectively, ζ is a shape parameter dependent upon fiber geometry and loading direction, and η is given by

$$\eta = \frac{E_f/E_m - 1}{E_f/E_m - \zeta} \quad (2-6)$$

where E_f represents the Young's modulus of the fiber. The Mori–Tanaka model is another well-known theory that considers a non-dilute composite containing many identical spheroidal particles. It is assumed that the composite experience an average stress different from that of the applied stress. Longitudinal and transverse elastic moduli in Mori–Tanaka model are [76-78]

$$\frac{E_{11}}{E_m} = \frac{A}{A + V_f(A_1 + 2\nu_m A_2)} \quad (2-7)$$

$$\frac{E_{22}}{E_m} = \frac{2A}{2A + V_f(-2\nu_m A_3 + A_4(1 - \nu_m) + AA_5(1 + \nu_m))} \quad (2-8)$$

where V_f is the volume fraction of filler and ν_m is the Poisson's ratio of the matrix; A_1 , A_2 , A_3 , A_4 , A_5 , and A are functions of the Eshelby's tensor and the properties of the fiber and the matrix with more explanation given in [77].

In theory, the aforementioned equations for short fiber composites can be used to model 3D printed parts, however, length and orientation of the fibers used in the process should match the assumptions. FDM, SLS, and extrusion with short fiber reinforcement can be modeled with these analytical methods. However, 3D printed parts often contain considerable fraction of void content and modifications may be necessary when applying these methods on additive manufacturing. Void in composite materials are comprehensively explained in [79].

Classical Laminate Plate Theory (CLPT)

CLPT is an extension of the classical plate theory for isotropic and homogeneous materials with some modifications to reflect the inhomogeneity in thickness direction of orthotropic materials. CLPT is applicable for all the 3D printed parts that exhibit orthogonal behavior. Here, we present a brief summary of CLPT for laminated plates consisting of multiple unidirectional laminae [79, 80]. Basic assumptions of CLPT are given in [79]. The stiffness matrix of each ply can be described as [79],

$$Q_{ij} = \begin{bmatrix} Q_{11} & Q_{12} & 0 \\ Q_{12} & Q_{22} & 0 \\ 0 & 0 & Q_{66} \end{bmatrix} \quad (2-9)$$

where

$$\begin{aligned} Q_{11} &= \frac{E_{11}^2}{E_{11} - \nu_{12}^2 E_{22}}, & Q_{12} &= \frac{\nu_{12} E_{11} E_{22}}{E_{11} - \nu_{12}^2 E_{22}}, \\ Q_{22} &= \frac{E_{11} E_{22}}{E_{11} - \nu_{12}^2 E_{22}}, & Q_{66} &= G_{12}. \end{aligned} \quad (2-10)$$

Transformed reduced stiffness matrix for various fiber orientation can be computed using transformation matrix as follow [79],

$$\bar{Q}_{ij} = T^{-1}Q_{ij}T \quad (2-11)$$

where

$$T = \begin{bmatrix} m^2 & n^2 & 2mn \\ n^2 & m^2 & -2mn \\ -mn & mn & m^2 - n^2 \end{bmatrix} \quad (2-12)$$

in which, $m = \cos \theta$, $n = \sin \theta$, and θ is the angle of the fiber reinforcement. Then, in-plane, coupling, and bending stiffness matrices can be obtained by, respectively [79],

$$A_{ij} = \sum_{k=1}^n \bar{Q}_k (z_k - z_{k-1}) \quad (2-13)$$

$$B_{ij} = \frac{1}{2} \sum_{k=1}^n \bar{Q}_k (z_k^2 - z_{k-1}^2) \quad (2-14)$$

$$D_{ij} = \frac{1}{3} \sum_{k=1}^n \bar{Q}_k (z_k^3 - z_{k-1}^3) \quad (2-15)$$

where z represents the vertical position in the ply from the midplane. Finally, we can write a connection between the applied loads and the associated strains in the laminate, as follows [79],

$$\begin{Bmatrix} N \\ M \end{Bmatrix} = \begin{bmatrix} A & B \\ B & D \end{bmatrix} \begin{Bmatrix} \varepsilon^0 \\ \kappa \end{Bmatrix} \quad (2-16)$$

where N is normal stress resultants, M is moment resultants, ε^0 represent strain term in midplane, and κ is the twist of the laminated plate. The strain along the plate thickness can be given by [79],

$$\begin{Bmatrix} \varepsilon_x \\ \varepsilon_y \\ \gamma_{xy} \end{Bmatrix} = \begin{Bmatrix} \varepsilon_x^0 \\ \varepsilon_y^0 \\ \gamma_{xy}^0 \end{Bmatrix} + z \begin{Bmatrix} \kappa_x \\ \kappa_y \\ \kappa_{xy} \end{Bmatrix} \quad (2-17)$$

Additionally, by using the same principle, CLPT can be applied to evaluate the strength and elastic constants of FDM printed parts with void content. As mentioned earlier, FDM process is associated with void formation between printing beads which needs to be considered in the modeling. In the method developed by Rodriguez, et al. [81] for ABS materials, The FDM part is defined as an unidirectional ABS–void composite with a laminate structure. This structure is consisting of vertically stacked layers with contiguous material “fibers” and voids. The unidirectional elastic constants are given as [82],

$$E_{11} = (1 - \rho_1)E \quad (2-18)$$

$$E_{22} = (1 - \rho_1^{0.5})E \quad (2-19)$$

$$G_{12} = G \frac{(1 - \rho_1)(1 - \rho_1^{0.5})}{(1 - \rho_1) + (1 - \rho_1^{0.5})} \quad (2-20)$$

$$\nu_{12} = (1 - \rho_1)\nu \quad (2-21)$$

$$\nu_{21} = (1 - \rho_1^{0.5})\nu \quad (2-22)$$

where, E , G , and ν represent the elastic modulus, shear modulus and Poisson’s ratio for the extruded polymer used in the FDM process. The ρ_1 is the area void density in the plane normal to filament direction. This method was used in various works for single material FDM parts containing void [82-85], however, certain modifications are needed in order to apply it to multi-material 3D printing. More information regarding void in composite structures can be found in [79].

Finite Element Method (FEM)

FEM is particularly interesting for modelling 3D printed part due to its flexibility in analyzing complex geometries in both macro and micro scale. It can be applied to continuous and short fiber 3D printed composites. The primary distinction of most composites by AM is the

significant void content that need to be incorporated into the respective finite element models. Perhaps the most appealing approaches for mechanical modelling of fiber composites are homogenization, which was described briefly in CLPT, and unit-cell (UC) based methods [86]. Both approaches can be implemented in FEM, thus, applicable to all AM methods. Conversely, there has been a lack of attention to modelling of these processes, and with increasing the popularity of 3D printing among practitioners, the need for simulating 3D printing is certain. UC is a single or multiple fibers embedded in the matrix with the volume fraction similar to those of the composite. A finite element model of this geometry using two different materials is constructed and various loadings are applied to characterize the behavior of the UC. In the case of composites with random fiber orientations the composite behavior is approximated by direct averaging over all orientations [87].

Another commonly used approach is multiscale methods by combining micro level and homogenized macro stress analysis. For many applications, homogenized properties are used to solve the problem, however, sometimes extra accuracy is needed. Microscopic level analysis can increase the accuracy, but are often too expensive to be used in practice. Multiscale modelling takes advantage of the efficiency of macroscopic models and the accuracy of the microscopic models. The microscope analysis is normally performed at the area of interest with high stress concentration [88, 89].

Final Remarks

3D printing of composite structures can be a turning point for AM technology. The potential of fabricating functional devices directly from commercial 3D printers with controllable properties created a huge rush for new development and research in this field. The attractive

combination of endless possibilities in the range of composite materials and extra customization of AM, which offers a uniquely new area in the manufacturing field for researchers and developers to explore. Fiber reinforcement significantly improves the mechanical properties of 3D printed parts. It can be implemented in various AM techniques, such as FDM, SLA, SLS, LOM, and extrusion. The alignment of fibers in 3D printing of composites was one of the major challenges in the reviewed literature and its improvement attracted tremendous research interest in almost all the existing AM methods. Recent advances in FDM printing of continuous fiber reinforced thermoplastics took these improvements one step further to establish AM as a dependable manufacturing method for various industries.

However, most 3D printing methodologies of composite materials still facing major challenges that should be addressed before becoming a mainstream manufacturing method. Void formation during printing, adhesion of fibers and polymer matrix, and challenges in continuous fiber printing are all amongst the existing issues in 3D printing of fiber composites. Moreover, most of the commercial 3D printers designed for specific resins and introduction of fillers can lead to blockage, wear, non-adhesion, and increased curing times.

In conclusion, AM of fiber reinforced polymer composites is tremendously promising in turning 3D printing from a prototyping method to a robust manufacturing technique. The unique characteristics of 3D printing, such as high customization combined with extra strength from fiber reinforcement and the ability to produce functional complex 3D structures with total control over material properties help AM of fiber-polymer composites gain enormous attentions from a broad range of science industries. Aerospace industry, automotive industry, biomedical science, electronic industries, and robotics are only a few examples of those attracted by AM of fiber reinforced polymer composites.

References

- [1] B. N. Turner, R. Strong, and S. A. Gold, "A review of melt extrusion additive manufacturing processes: I. Process design and modeling," *Rapid prototyping journal*, vol. 20, no. 3, pp. 192-204, 2014.
- [2] S.-H. Ahn, M. Montero, D. Odell, S. Roundy, and P. K. Wright, "Anisotropic material properties of fused deposition modeling ABS," *Rapid prototyping journal*, vol. 8, no. 4, pp. 248-257, 2002.
- [3] R. B. Dinwiddie *et al.*, "Infrared imaging of the polymer 3D-printing process," 2014, vol. 9105, pp. 910502-910502-12. [Online]. Available: <http://dx.doi.org/10.1117/12.2053425>. [Online]. Available: <http://dx.doi.org/10.1117/12.2053425>
- [4] Q. Sun, G. Rizvi, C. Bellehumeur, and P. Gu, "Effect of processing conditions on the bonding quality of FDM polymer filaments," *Rapid prototyping journal*, vol. 14, no. 2, pp. 72-80, 2008.
- [5] D. Ahn, J.-H. Kweon, S. Kwon, J. Song, and S. Lee, "Representation of surface roughness in fused deposition modeling," *Journal of Materials Processing Technology*, vol. 209, no. 15, pp. 5593-5600, 2009.
- [6] W. Zhong, F. Li, Z. Zhang, L. Song, and Z. Li, "Short fiber reinforced composites for fused deposition modeling," *Materials Science and Engineering: A*, vol. 301, no. 2, pp. 125-130, 2001.
- [7] O. Carneiro, A. Silva, and R. Gomes, "Fused deposition modeling with polypropylene," *Materials & Design*, vol. 83, pp. 768-776, 2015.
- [8] M. L. Shofner, K. Lozano, F. J. Rodríguez-Macías, and E. V. Barrera, "Nanofiber-reinforced polymers prepared by fused deposition modeling," *J. Appl. Polym. Sci.*, vol. 89, no. 11, pp. 3081-3090, 2003, doi: 10.1002/app.12496.
- [9] M. L. Shofner, F. J. Rodríguez-Macías, R. Vaidyanathan, and E. V. Barrera, "Single wall nanotube and vapor grown carbon fiber reinforced polymers processed by extrusion freeform fabrication," *Composites Part A: Applied Science and Manufacturing*, vol. 34, no. 12, pp. 1207-1217, 12// 2003, doi: <http://dx.doi.org/10.1016/j.compositesa.2003.07.002>.
- [10] R. W. Gray IV, D. G. Baird, and J. H. Bøhn, "Effects of processing conditions on short TLCP fiber reinforced FDM parts," *Rapid prototyping journal*, vol. 4, no. 1, pp. 14-25, 1998.

- [11] F. Ning, W. Cong, J. Qiu, J. Wei, and S. Wang, "Additive manufacturing of carbon fiber reinforced thermoplastic composites using fused deposition modeling," *Composites Part B: Engineering*, vol. 80, pp. 369-378, 2015.
- [12] H. L. Tekinalp *et al.*, "Highly oriented carbon fiber–polymer composites via additive manufacturing," *Composites Science and Technology*, vol. 105, no. 0, pp. 144-150, 2014, doi: <http://dx.doi.org/10.1016/j.compscitech.2014.10.009>.
- [13] R. Matsuzaki *et al.*, "Three-dimensional printing of continuous-fiber composites by in-nozzle impregnation," *Scientific Reports*, vol. 6, p. 23058, 03/11 2016, doi: 10.1038/srep23058.
- [14] M. Namiki, M. Ueda, A. Todoroki, Y. Hirano, and R. Matsuzaki, "3D printing of continuous fiber reinforced plastic," *Proceedings of the Society of the Advancement of Material and Process Engineering*, 2014.
- [15] N. Li, Y. Li, and S. Liu, "Rapid prototyping of continuous carbon fiber reinforced polylactic acid composites by 3D printing," *J. Mater. Process. Technol.*, vol. 238, pp. 218-225, 12// 2016, doi: <http://dx.doi.org/10.1016/j.jmatprotec.2016.07.025>.
- [16] T. Yu, J. Ren, S. Li, H. Yuan, and Y. Li, "Effect of fiber surface-treatments on the properties of poly(lactic acid)/ramie composites," *Composites Part A: Applied Science and Manufacturing*, vol. 41, no. 4, pp. 499-505, 4// 2010, doi: <http://dx.doi.org/10.1016/j.compositesa.2009.12.006>.
- [17] X. Tian, T. Liu, C. Yang, Q. Wang, and D. Li, "Interface and performance of 3D printed continuous carbon fiber reinforced PLA composites," *Composites Part A: Applied Science and Manufacturing*, vol. 88, pp. 198-205, 9// 2016, doi: <http://dx.doi.org/10.1016/j.compositesa.2016.05.032>.
- [18] G. W. Melenka, B. K. Cheung, J. S. Schofield, M. R. Dawson, and J. P. Carey, "Evaluation and prediction of the tensile properties of continuous fiber-reinforced 3D printed structures," *Compos. Struct.*, vol. 153, pp. 866-875, 2016.
- [19] K.-i. Mori, T. Maeno, and Y. Nakagawa, "Dieless forming of carbon fibre reinforced plastic parts using 3D printer," *Procedia Engineering*, vol. 81, pp. 1595-1600, 2014.
- [20] F. Van Der Klift, Y. Koga, A. Todoroki, M. Ueda, Y. Hirano, and R. Matsuzaki, "3D printing of continuous carbon fibre reinforced thermo-plastic (CFRTP) tensile test specimens," *Open Journal of Composite Materials*, vol. 6, no. 01, p. 18, 2015.
- [21] S. H. Huang, P. Liu, A. Mokasdar, and L. Hou, "Additive manufacturing and its societal impact: a literature review," *The International Journal of Advanced Manufacturing Technology*, journal article vol. 67, no. 5, pp. 1191-1203, 2013, doi: 10.1007/s00170-012-4558-5.

- [22] D. Mahindru, S. Priyanka Mahendru, and T. Ganj, "Review of rapid prototyping-technology for the future," *Global Journal of Computer Science and Technology*, vol. 13, no. 4, 2013.
- [23] D. Klosterman *et al.*, "Direct Fabrication of Polymer Composite Structures with Cuwed LOM," 1999.
- [24] D. Klosterman, R. Chartoff, G. Graves, N. Osborne, and B. Priore, "Interfacial characteristics of composites fabricated by laminated object manufacturing," *Composites Part A: Applied Science and Manufacturing*, vol. 29, no. 9, pp. 1165-1174, 1998.
- [25] F. O. Sonmez and H. T. Hahn, "Thermomechanical analysis of the laminated object manufacturing (LOM) process," *Rapid Prototyping Journal*, vol. 4, no. 1, pp. 26-36, 1998, doi: doi:10.1108/13552549810197541.
- [26] D. Karalekas and K. Antoniou, "Composite rapid prototyping: overcoming the drawback of poor mechanical properties," *J. Mater. Process. Technol.*, vol. 153–154, pp. 526-530, 11/10/ 2004, doi: <http://dx.doi.org/10.1016/j.jmatprotec.2004.04.019>.
- [27] L. Lü, J. Y. H. Fuh, and Y. S. Wong, "Improvements of Mechanical Properties by Reinforcements," in *Laser-Induced Materials and Processes for Rapid Prototyping*. Boston, MA: Springer US, 2001, pp. 67-88.
- [28] J. H. Sandoval and R. B. Wicker, "Functionalizing stereolithography resins: effects of dispersed multi-walled carbon nanotubes on physical properties," *Rapid prototyping journal*, vol. 12, no. 5, pp. 292-303, 2006.
- [29] D. E. Karalekas, "Study of the mechanical properties of nonwoven fibre mat reinforced photopolymers used in rapid prototyping," *Materials & Design*, vol. 24, no. 8, pp. 665-670, 2003/12/01/ 2003, doi: [https://doi.org/10.1016/S0261-3069\(03\)00153-5](https://doi.org/10.1016/S0261-3069(03)00153-5).
- [30] G. Zak, A. Chan, C. Park, and B. Benhabib, "Viscosity analysis of photopolymer and glass-fibre composites for rapid layered manufacturing," *Rapid Prototyping Journal*, vol. 2, no. 3, pp. 16-23, 1996.
- [31] C. Cheah, J. Fuh, A. Nee, and L. Lu, "Mechanical characteristics of fiber-filled photopolymer used in stereolithography," *Rapid prototyping journal*, vol. 5, no. 3, pp. 112-119, 1999.
- [32] A. Gupta and A. A. Ogale, "Dual curing of carbon fiber reinforced photoresins for rapid prototyping," *Polym. Compos.*, vol. 23, no. 6, pp. 1162-1170, 2002, doi: 10.1002/pc.10509.
- [33] T. M. Llewellyn-Jones, B. W. Drinkwater, and R. S. Trask, "3D printed components with ultrasonically arranged microscale structure," *Smart Mater. Struct.*, vol. 25, no. 2, p. 02LT01, 2016.

- [34] K. Kim *et al.*, "3D Optical Printing of Piezoelectric Nanoparticle–Polymer Composite Materials," *ACS Nano*, vol. 8, no. 10, pp. 9799-9806, 2014/10/28 2014, doi: 10.1021/nn503268f.
- [35] S.-Z. Guo, F. Gosselin, N. Guerin, A.-M. Lanouette, M.-C. Heuzey, and D. Therriault, "Solvent-Cast Three-Dimensional Printing of Multifunctional Microsystems," *Small*, vol. 9, no. 24, pp. 4118-4122, 2013, doi: 10.1002/sml.201300975.
- [36] B. G. Compton and J. A. Lewis, "3D-Printing of Lightweight Cellular Composites," *Adv. Mater.*, vol. 26, no. 34, pp. 5930-5935, 2014, doi: 10.1002/adma.201401804.
- [37] G. Postiglione, G. Natale, G. Griffini, M. Levi, and S. Turri, "Conductive 3D microstructures by direct 3D printing of polymer/carbon nanotube nanocomposites via liquid deposition modeling," *Composites Part A: Applied Science and Manufacturing*, vol. 76, pp. 110-114, 2015.
- [38] P. Bertrand, F. Bayle, C. Combe, P. Gœuriot, and I. Smurov, "Ceramic components manufacturing by selective laser sintering," *Applied Surface Science*, vol. 254, no. 4, pp. 989-992, 2007.
- [39] I. Shishkovsky, I. Yadroitsev, P. Bertrand, and I. Smurov, "Alumina–zirconium ceramics synthesis by selective laser sintering/melting," *Applied Surface Science*, vol. 254, no. 4, pp. 966-970, 2007.
- [40] D. L. Bourell, H. L. Marcus, J. W. Barlow, and J. J. Beaman, "Selective laser sintering of metals and ceramics," *International Journal of Powder Metallurgy*, vol. 28, no. 4, pp. 369-381, 1992.
- [41] Z. Liu, J. J. Nolte, J. Packard, G. Hilmas, F. Dogan, and M. Leu, "Selective laser sintering of high-density alumina ceramic parts," in *Proceedings of the 35th international matador conference*, 2007: Springer, pp. 351-354.
- [42] M. Agarwala, D. Bourell, J. Beaman, H. Marcus, and J. Barlow, "Direct selective laser sintering of metals," *Rapid prototyping journal*, vol. 1, no. 1, pp. 26-36, 1995.
- [43] A. Chatterjee, S. Kumar, P. Saha, P. Mishra, and A. R. Choudhury, "An experimental design approach to selective laser sintering of low carbon steel," *Journal of Materials Processing Technology*, vol. 136, no. 1, pp. 151-157, 2003.
- [44] S. Das, "Physical aspects of process control in selective laser sintering of metals," *Advanced Engineering Materials*, vol. 5, no. 10, pp. 701-711, 2003.
- [45] X. Wang, T. Laoui, J. Bonse, J.-P. Kruth, B. Lauwers, and L. Froyen, "Direct selective laser sintering of hard metal powders: experimental study and simulation," *The*

- International Journal of Advanced Manufacturing Technology*, vol. 19, no. 5, pp. 351-357, 2002.
- [46] J.-P. Kruth, L. Froyen, J. Van Vaerenbergh, P. Mercelis, M. Rombouts, and B. Lauwers, "Selective laser melting of iron-based powder," *Journal of Materials Processing Technology*, vol. 149, no. 1, pp. 616-622, 2004.
- [47] Y.-A. Song and W. Koenig, "Experimental study of the basic process mechanism for direct selective laser sintering of low-melting metallic powder," *CIRP Annals-Manufacturing Technology*, vol. 46, no. 1, pp. 127-130, 1997.
- [48] T. Childs, C. Hauser, and M. Badrossamay, "Selective laser sintering (melting) of stainless and tool steel powders: experiments and modelling," *Proceedings of the Institution of Mechanical Engineers, Part B: Journal of Engineering Manufacture*, vol. 219, no. 4, pp. 339-357, 2005.
- [49] K. Tan *et al.*, "Scaffold development using selective laser sintering of polyetheretherketone–hydroxyapatite biocomposite blends," *Biomaterials*, vol. 24, no. 18, pp. 3115-3123, 2003.
- [50] T. Childs, M. Berzins, G. R. Ryder, and A. Tontowi, "Selective laser sintering of an amorphous polymer—simulations and experiments," *Proceedings of the Institution of Mechanical Engineers, Part B: Journal of Engineering Manufacture*, vol. 213, no. 4, pp. 333-349, 1999.
- [51] J. Bai, R. D. Goodridge, R. J. M. Hague, and M. Song, "Improving the mechanical properties of laser-sintered polyamide 12 through incorporation of carbon nanotubes," *Polymer Engineering & Science*, vol. 53, no. 9, pp. 1937-1946, 2013, doi: 10.1002/pen.23459.
- [52] G. V. Salmoria, R. A. Paggi, A. Lago, and V. E. Beal, "Microstructural and mechanical characterization of PA12/MWCNTs nanocomposite manufactured by selective laser sintering," *Polymer Testing*, vol. 30, no. 6, pp. 611-615, 2011.
- [53] C. Yan, L. Hao, L. Xu, and Y. Shi, "Preparation, characterisation and processing of carbon fibre/polyamide-12 composites for selective laser sintering," *Composites Sci. Technol.*, vol. 71, no. 16, pp. 1834-1841, 11/14/ 2011, doi: <https://doi.org/10.1016/j.compscitech.2011.08.013>.
- [54] R. D. Goodridge *et al.*, "Processing of a Polyamide-12/carbon nanofibre composite by laser sintering," *Polymer Testing*, vol. 30, no. 1, pp. 94-100, 2011, doi: <http://dx.doi.org/10.1016/j.polymertesting.2010.10.011>.
- [55] U. Ajoku, N. Hopkinson, and M. Caine, "Experimental measurement and finite element modelling of the compressive properties of laser sintered Nylon-12," *Materials Science and Engineering: A*, vol. 428, no. 1, pp. 211-216, 2006.

- [56] B. Caulfield, P. McHugh, and S. Lohfeld, "Dependence of mechanical properties of polyamide components on build parameters in the SLS process," *Journal of Materials Processing Technology*, vol. 182, no. 1, pp. 477-488, 2007.
- [57] T. Childs, C. Hauser, C. Taylor, and A. Tontowi, "Simulation and experimental verification of crystalline polymer and direct metal selective laser sintering," in *Proc. SFF Symp., Austin*, 2000, pp. 100-109.
- [58] J. Kim and T. Creasy, "Selective laser sintering characteristics of nylon 6/clay-reinforced nanocomposite," *Polymer Testing*, vol. 23, no. 6, pp. 629-636, 2004.
- [59] H. Zarringhalam, N. Hopkinson, N. Kamperman, and J. De Vlieger, "Effects of processing on microstructure and properties of SLS Nylon 12," *Materials Science and Engineering: A*, vol. 435, pp. 172-180, 2006.
- [60] J. T. Rimell and P. M. Marquis, "Selective laser sintering of ultra high molecular weight polyethylene for clinical applications," *Journal of biomedical materials research*, vol. 53, no. 4, pp. 414-420, 2000.
- [61] L. Hao, M. Savalani, Y. Zhang, K. Tanner, and R. Harris, "Selective laser sintering of hydroxyapatite reinforced polyethylene composites for bioactive implants and tissue scaffold development," *Proceedings of the Institution of Mechanical Engineers, Part H: Journal of Engineering in Medicine*, vol. 220, no. 4, pp. 521-531, 2006.
- [62] G. V. Salmoria, C. H. Ahrens, P. Klauss, R. A. Paggi, R. G. Oliveira, and A. Lago, "Rapid manufacturing of polyethylene parts with controlled pore size gradients using selective laser sintering," *Materials Research*, vol. 10, no. 2, pp. 211-214, 2007.
- [63] M. Schmidt, D. Pohle, and T. Rechtenwald, "Selective laser sintering of PEEK," *CIRP Annals-Manufacturing Technology*, vol. 56, no. 1, pp. 205-208, 2007.
- [64] J.-P. Kruth, G. Levy, F. Klocke, and T. Childs, "Consolidation phenomena in laser and powder-bed based layered manufacturing," *CIRP Annals-Manufacturing Technology*, vol. 56, no. 2, pp. 730-759, 2007.
- [65] J. M. Williams *et al.*, "Bone tissue engineering using polycaprolactone scaffolds fabricated via selective laser sintering," *Biomaterials*, vol. 26, no. 23, pp. 4817-4827, 2005.
- [66] J.-P. Kruth, P. Mercelis, J. Van Vaerenbergh, L. Froyen, and M. Rombouts, "Binding mechanisms in selective laser sintering and selective laser melting," *Rapid prototyping journal*, vol. 11, no. 1, pp. 26-36, 2005.
- [67] S. Yuan, J. Bai, C. Chua, J. Wei, and K. Zhou, "Material Evaluation and Process Optimization of CNT-Coated Polymer Powders for Selective Laser Sintering," *Polymers*,

- vol. 8, no. 10, p. 370, 2016. [Online]. Available: <http://www.mdpi.com/2073-4360/8/10/370>.
- [68] J. Bai, R. Goodridge, S. Yuan, K. Zhou, C. Chua, and J. Wei, "Thermal Influence of CNT on the Polyamide 12 Nanocomposite for Selective Laser Sintering," *Molecules*, vol. 20, no. 10, p. 19041, 2015. [Online]. Available: <http://www.mdpi.com/1420-3049/20/10/19041>.
- [69] H. Chung and S. Das, "Processing and properties of glass bead particulate-filled functionally graded Nylon-11 composites produced by selective laser sintering," *Materials Science and Engineering: A*, vol. 437, no. 2, pp. 226-234, 2006.
- [70] W. Zhu *et al.*, "A novel method based on selective laser sintering for preparing high-performance carbon fibres/polyamide12/epoxy ternary composites," *Scientific Reports*, Article vol. 6, p. 33780, 09/21/online 2016, doi: 10.1038/srep33780
<https://www.nature.com/articles/srep33780#supplementary-information>.
- [71] M. R. Piggott, "Short Fibre Polymer Composites: a Fracture-Based Theory of Fibre Reinforcement," *J. Compos. Mater.*, vol. 28, no. 7, pp. 588-606, 1994/05/01 1994, doi: 10.1177/002199839402800701.
- [72] P. A. Templeton, "Strength Predictions of Injection Molding Compounds," *J. Reinf. Plast. Compos.*, vol. 9, no. 3, pp. 210-225, 1990/05/01 1990, doi: 10.1177/073168449000900301.
- [73] S.-Y. Fu and B. Lauke, "Effects of fiber length and fiber orientation distributions on the tensile strength of short-fiber-reinforced polymers," *Composites Sci. Technol.*, vol. 56, no. 10, pp. 1179-1190, 1996/01/01 1996, doi: [http://dx.doi.org/10.1016/S0266-3538\(96\)00072-3](http://dx.doi.org/10.1016/S0266-3538(96)00072-3).
- [74] A. Kelly and W. R. Tyson, "Tensile properties of fibre-reinforced metals: Copper/tungsten and copper/molybdenum," *Journal of the Mechanics and Physics of Solids*, vol. 13, no. 6, pp. 329-350, 1965/12/01 1965, doi: [http://dx.doi.org/10.1016/0022-5096\(65\)90035-9](http://dx.doi.org/10.1016/0022-5096(65)90035-9).
- [75] J. Halpin, "Stiffness and expansion estimates for oriented short fiber composites," *J. Compos. Mater.*, vol. 3, no. 4, pp. 732-734, 1969.
- [76] T. D. Fornes and D. R. Paul, "Modeling properties of nylon 6/clay nanocomposites using composite theories," *Polymer*, vol. 44, no. 17, pp. 4993-5013, 8// 2003, doi: [https://doi.org/10.1016/S0032-3861\(03\)00471-3](https://doi.org/10.1016/S0032-3861(03)00471-3).
- [77] G. P. Tandon and G. J. Weng, "The effect of aspect ratio of inclusions on the elastic properties of unidirectionally aligned composites," *Polym. Compos.*, vol. 5, no. 4, pp. 327-333, 1984, doi: 10.1002/pc.750050413.

- [78] T. Mori and K. Tanaka, "Average stress in matrix and average elastic energy of materials with misfitting inclusions," *Acta Metall.*, vol. 21, no. 5, pp. 571-574, 1973/05/01 1973, doi: [http://dx.doi.org/10.1016/0001-6160\(73\)90064-3](http://dx.doi.org/10.1016/0001-6160(73)90064-3).
- [79] E. J. Barbero, *Introduction to composite materials design*. CRC press, 2010.
- [80] J. N. Reddy, "A generalization of two-dimensional theories of laminated composite plates," *Communications in Applied Numerical Methods*, vol. 3, no. 3, pp. 173-180, 1987, doi: 10.1002/cnm.1630030303.
- [81] J. F. Rodriguez, J. P. Thomas, and J. E. Renaud, "Characterization of the mesostructure of fused-deposition acrylonitrile-butadiene-styrene materials," *Rapid Prototyping Journal*, vol. 6, no. 3, pp. 175-186, 2000, doi: doi:10.1108/13552540010337056.
- [82] G. W. Melenka, J. S. Schofield, M. R. Dawson, and J. P. Carey, "Evaluation of dimensional accuracy and material properties of the MakerBot 3D desktop printer," *Rapid Prototyping Journal*, vol. 21, no. 5, pp. 618-627, 2015, doi: doi:10.1108/RPJ-09-2013-0093.
- [83] P. Gu and L. Li, "Fabrication of Biomedical Prototypes with Locally Controlled Properties Using FDM," *CIRP Annals - Manufacturing Technology*, vol. 51, no. 1, pp. 181-184, 2002/01/01/ 2002, doi: [http://dx.doi.org/10.1016/S0007-8506\(07\)61495-4](http://dx.doi.org/10.1016/S0007-8506(07)61495-4).
- [84] J. F. Rodríguez, J. P. Thomas, and J. E. Renaud, "Mechanical behavior of acrylonitrile butadiene styrene fused deposition materials modeling," *Rapid Prototyping Journal*, vol. 9, no. 4, pp. 219-230, 2003, doi: doi:10.1108/13552540310489604.
- [85] L. Li, Q. Sun, C. Bellehumeur, and P. Gu, "Composite Modeling and Analysis for Fabrication of FDM Prototypes with Locally Controlled Properties," *Journal of Manufacturing Processes*, vol. 4, no. 2, pp. 129-141, 2002/01/01/ 2002, doi: [http://dx.doi.org/10.1016/S1526-6125\(02\)70139-4](http://dx.doi.org/10.1016/S1526-6125(02)70139-4).
- [86] D. Notta-Cuvier, F. Lauro, and B. Bennani, "An original approach for mechanical modelling of short-fibre reinforced composites with complex distributions of fibre orientation," *Composites Part A: Applied Science and Manufacturing*, vol. 62, pp. 60-66, 7// 2014, doi: <https://doi.org/10.1016/j.compositesa.2014.03.016>.
- [87] J. Modniks and J. Andersons, "Modeling the non-linear deformation of a short-flax-fiber-reinforced polymer composite by orientation averaging," *Composites Part B: Engineering*, vol. 54, pp. 188-193, 11// 2013, doi: <https://doi.org/10.1016/j.compositesb.2013.04.058>.
- [88] P. Kanouté, D. P. Boso, J. L. Chaboche, and B. A. Schrefler, "Multiscale Methods for Composites: A Review," *Archives of Computational Methods in Engineering*, journal article vol. 16, no. 1, pp. 31-75, 2009, doi: 10.1007/s11831-008-9028-8.

- [89] E. Weinan, B. Engquist, X. Li, W. Ren, and E. Vanden-Eijnden, "Heterogeneous multiscale methods: a review," *Commun. Comput. Phys*, vol. 2, no. 3, pp. 367-450, 2007.

Chapter 3 - Additive Manufacturing of Continuous Glass Fiber Thermoplastic Composites

Continuous fiber reinforced thermoplastic polymer composites (CFRTPCs) exhibit superior properties, including mechanical performance, versatility, recyclability, and the potential for light-weight structures, that enable CFRTPCs as a substitute material for steel and conventional thermoset polymers in automotive, transportation, aerospace, and marine applications [1, 2]. Continuous glass fiber (GF) and low glass transition temperature matrix systems such as polypropylene (PP) combine ease of processing, lower associated manufacturing costs, high volume processing potential, and performance suited for high end uses. Additionally, these composites exhibit enhanced toughness, chemical-environmental resistance, damage tolerance, and an unlimited shelf life at relatively low cost. A large range of GF/PP composites is commercially available possessing these features [1, 3]. High performance levels can be achieved with high fiber concentration and continuous fiber reinforcement; however, these attributes increase the processing complexity [4]. To date, numerous manufacturing methods for CFRTPCs have been developed, such as compression molding, stamping, vacuum forming, filament winding, pultrusion, and bladder-assisted molding. These manufacturing methods are often associated with expensive molds, and inability to produce complex construction with customized fibers alignment [5]. As a result, alternative manufacturing techniques for CFRTPCs are under great demand in order to bypass the long, expensive processing procedures, and add more complexity to manufactured structures.

Additive manufacturing (AM) or three-dimensional (3D) printing attracted popularity due to high customization and development of application-oriented parts [6]. AM is a promising

technology that has not reached its full potential, particularly in the field of composites. Various researchers worked on applying AM to fiber reinforced thermoplastics in order to benefit from the vast flexibility in 3D composite manufacturing [7]. Most of the works done in this field focused on fused deposition modeling (FDM), selective laser sintering (SLS), and stereolithography (SL) with short fiber reinforcement. Zhong, et al. [8] included short GFs in the filament for improved strength; but, extrusion force and potential tool wear were spotted during the process. Inclusion of short iron and copper fibers in acrylonitrile butadiene styrene (ABS) filament resulted in higher stiffness compared to printed pure ABS [9]. Shofner, et al. [10] compounded carbon nanotube and vapor grown carbon fiber with ABS in FDM 3D printing for improved mechanical properties. Tekinalp, et al. [11] developed a method to control the orientation of short carbon fibers in the matrix; reportedly, tensile strength and modulus of 3D printed samples exhibited 115% and 700% increase compared to pure thermoplastic matrix, respectively. However, FDM samples printed with this method showed significant pore formation between deposited filaments during 3D printing. Ning, et al. [12] reported that inclusion of 5 wt% carbon fiber content in ABS filament, also increased flexural strength, flexural modulus, and flexural toughness by 11.82%, 16.82%, and 21.86%, respectively. Short carbon fiber/ABS was also used FDM 3D printing of 3D orthogonal preforms and poor carbon fiber-ABS interfacial bonding and the high content of fibers under 100 μm in length (~ 50 wt%) were spotted indicating low reinforcing efficiency of short carbon fibers. The authors named continuous fiber reinforcement A highly desirable solution [13]. Carneiro, et al. [14] reinforced polypropylene with short GF for FDM and achieved 30% and 40% improvement for the modulus and strength, respectively. Compton and Lewis [15] employed an a new epoxy-based ink for 3D inkjet printing of cellular composites with controlled alignment of multi-scale and high aspect ratio fiber reinforcement. These structures exhibited Young's modulus an order of

magnitude higher than thermoplastics and photocurable resins utilized in commercial 3D printers. SLS process has been also modified for fiber composites and carbon fiber filled polyamide composite powder is commercially available for SLS, however, mechanical mixing is not able to provide a uniform distribution of carbon fiber in the composite powder which can result in carbon fiber aggregates. Although efforts has been made to coat the fibers with nylon-12 through the dissolution–precipitation process to form suitable CF/PA composite powders, SLS is not capable of continuous or long fiber reinforcement [16-18]. Similarly, SL process is able to fabricate 3D parts with short fiber reinforcement. Carbon fiber and glass fiber has been successfully applied to SL, but, carbon fiber can block the UV light and interferes the curing process which can be resolved by thermal treatment [19]. Various fiber orientation and uniform fiber distribution were achieved by ultrasonic manipulation of the composite resin used in SL process [20].

The aforementioned methods for AM of short fiber composites reported improved strength relative to the thermoplastic matrix; however, continuous fiber (CF) reinforcement has extra potential to be used in functional parts with more substantial effect on the mechanical properties. Maximum achievable stiffness and strength can only be obtained using CF, since most of the load in these composites is carried by the fibers oriented along the load direction [21]. Laminated object manufacturing (LOM) was one of the first developed AM methods capable of CF reinforcement. 3D parts in LOM are manufactured by cutting 2D cross-sections with laser or blade and sequentially laminating the sheets. Prepreg CF/epoxy composite sheets have been utilized in LOM successfully, however, additional heat treatment was required to fully cure the resin and consolidate the prepreg layers [22, 23]. Furthermore, LOM is often associated with large amount of waste material and postproduction time is necessary to eliminate waste and in some cases secondary processes are required to produce accurately functional parts [24]. Lately, efforts have

been made to modify FDM for CF polymers composites. Mori, et al. [25] proposed a FDM method in which continuous carbon fibers were sandwiched between lower and upper plastic plates, and then the plates were heated for better bonding between layers. Although relatively higher strength was achieved, the usage of carbon fiber was limited in this method and porosity of composite structures had negative effects on the strength of the components. Lately, a new FDM method was developed for continuous carbon fiber/polyactic acid (PLA). PLA and carbon fiber were supplied separately before heating and mixing inside the printing head [26-28]. However, this method, similar to other FDM techniques, suffers from bonding issues and void formation between printing beads.

On the other hand, there are other composite manufacturing methods with high potential to be customized for AM. Laser assisted tape placement (LATP) is one of the most promising techniques due to its flexibility and capability to achieve continuous fiber reinforcement. A significant advantage of this method is the ability to manufacture parts of essentially unlimited size in a rapid, potentially saving large capital and running costs associated with large autoclaves. In LATP the high temperature induced by the laser at the nip point combined with high compaction forces of the consolidation roller decrease the viscosity of the polymeric matrix, and the applied roller pressure promotes inter-ply bonding [29]. Recently, laser gained interest over alternative heat sources such as hot gas due to energy efficiency and precise control [30]. 94% of autoclave properties could be achieved for carbon fiber–polyether ether ketone (PEEK) using a diode laser processing head [31]. LATP is associated with high cooling rates, and high toughness was observed in LATP parts with Polyphenylene sulfide (PPS) and PEEK matrix due to largely amorphous morphology [32-35]. Rosselli, et al. [36] studied the effect of process parameters on strength of thermoplastic composite rings manufactured by laser assisted on line consolidation.

Comer, et al. [29] investigated LATP in comparison with traditional autoclave methods for carbon fiber/PEEK manufacturing. It performed better in terms of interlaminar toughness, but flexural strength, interlaminar shear strength, flexural stiffness, and open-hole-compression strength were not on par with autoclave.

As discussed in aforementioned literature review, there are various issues with existing methods used for additive manufacturing of fiber, especially for continuous fiber, reinforced thermoplastics. LATP process is able to manufacture 3D composite structures with minimal void concentration and continuous fiber reinforcement. Our proposed method implements similar method for adding prepreg composite tapes in successive layers and cut the layer according to the CAD file. Prepreg tapes are placed in parallel using LATP to cover each layer prior to laser cut the 2D shape associated with each layer and no post processing is required after the AM process. This method demonstrates the potential to solve the issue with interfacial bonding associated with FDM while offering continuous fiber as reinforcement. In addition, the proposed method is preferred to LOM since it significantly reduces waste material due to use of prepreg narrow tapes instead of prepreg sheet and postprocessing is not necessary due to full consolidation of prepreg tapes. In the present work, interfacial microstructure and mechanical performance of the parts prepared with glass fiber/polypropylene (PP) prepreg by this newly proposed method were studied in assessment with other AM and traditional methods for fiber reinforced polymer.

Experimental

Materials

The thermoplastic composite prepreps used in this study were unidirectional (UD) GF/PP (IE 6832, 66.5% GF) and bidirectional (BD) GF/PP (IE 6010, 60.0% GF) supplied by Polystrand

(Englewood, CO) with 0.30 mm and 0.6 mm thickness, respectively. The matrix of the prepreg composite is PP copolymer reinforced and the diameter of GF is 15 μm . The prepreg sheets were cut into 5 mm wide tapes for laser assisted AM process.

Laser assisted additive manufacturing

The proposed AM method was to add prepreg GF/PP composites in successive layers. A desired 3D shape defined by the CAD file is “sliced” into multiple 2D layers, and each layer is laser cut accordingly to a corresponding 2D slice. This process is iterated layer by layer until an ultimate laminate structure, in the 3D shape defined by the CAD file, achieved. The first layer of the part uses the sheet prepreg instead of the narrow cut tapes for simplicity and higher quality bond. This layer is used as the base layer for the laminated object. Using narrow tapes reduces the waste associated with similar LOM method, where the 2D shape is cut prior to bonding with hot roller. The tape strips are placed layer by layer using a laser and compaction roller. Figure 3-1 illustrates the laser assisted AM to obtain a 3D shape, as well as some 3D parts produced by this method. The v_b denotes to binding velocity for the tape placement process and v_c is the cutting speed of a focused laser used to cut the desired shape of each layer. The laser was emitted at the interface of two layers with the angle of 18° from the base before applying pressure by compaction roller to consolidate the prepreg tapes. The laser used in this work is CO₂ laser (Beijing Reci Laser Technology, China) with maximum power of 100W. In our setup, the roller, laser beam, and mirrors were fixed during the tape placement process and prepreg tapes were supplied under the compaction roller using a motorized stage. The laser power was 22-28 W and the stage was moving at the speed of 1-4 mm/s (v_b) to feed the tape under the roller. After achieving a rough shape of the 2D shape, the fine shape is cut using Full Spectrum (Las Vegas, NV) P-Series 24x16+ CO₂ laser with maximum power of 90 W. In the present setup, the part being printed moves back and

forth between two stations and the parameters of laser cutting process are 31.5 W power, 70 mm/s cutting speed (v_c), and spot diameter of 1 mm. The camera pictures of the described setup is presented in Figure 3-2.

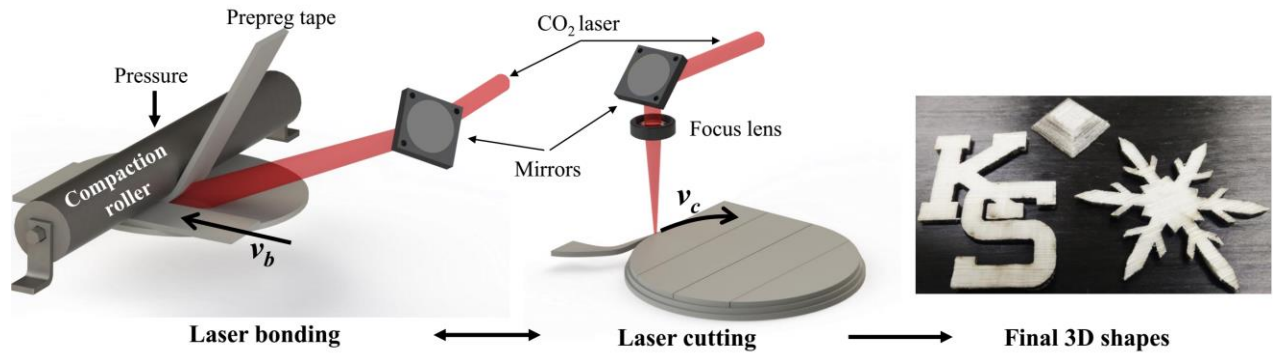


Figure 3-1 3D schematic of the proposed additive manufacturing method

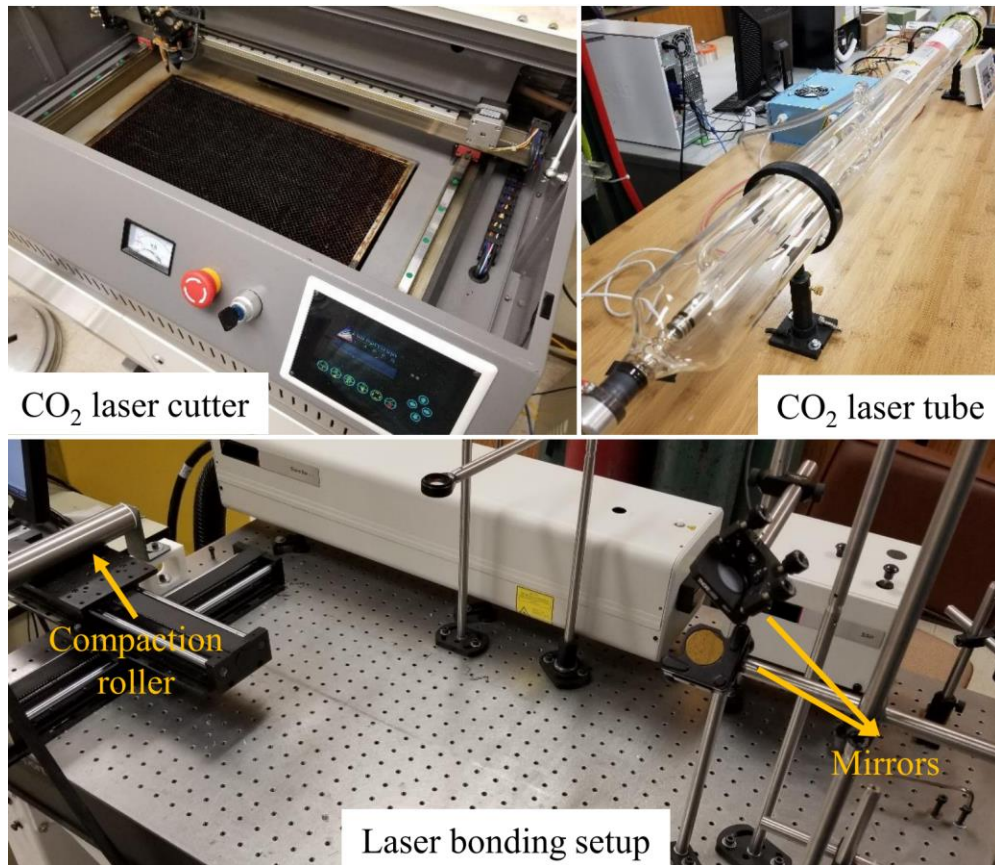


Figure 3-2 Camera pictures of the laser assisted AM setup

Characterization

Scanning electron microscopy (SEM) (FEI Versa 3D Dual Beam, OR) was used for microstructure characterization. The cross-sectional images were used to demonstrate the orientation of the continuous fibers, any possible void content, and bonding details. The surface of the SEM samples was first sputter coated with gold with the thickness of 15 nm. Then, SEM micrographs were observed at an acceleration voltage of 10 kV and an emission current of 20 μ A.

The mechanical properties of the 3D printed parts were characterized with T-peel test, single lap shear test, tensile test, and 3-point bending test. All mechanical tests were performed using Shimadzu EZ-LX universal testing machine, Kyoto, Japan. The T-peel test was run at 5 mm/min, and lap shear test was conducted at the speed of 1.3 mm/s, both using 3 mm wide tapes. At least 4 dog-bone samples were used to determine the tensile related properties of tensile strength and modulus at the strain rates of 1 mm/min. The 3-point bend test was conducted to measure the flexural strength and modulus at the speed 1 mm/s.

Results and discussion

A new AM methodology of CFRTPCs by customizing the laser cutting and laser bonding process was proposed and evaluated. As we demonstrated in this paper, additive manufactured samples with continuous reinforcement prepared by the proposed method presenting high strength, which is in the range of traditional manufacturing methods such as compression molding. Our results also demonstrated that no void was formed during this process which is essential for load bearing components. Detailed results are given in this section.

Cross-sectional microstructure

Bonding mechanism at micro level was studied through cross-sectional SEM images of printed samples. Aforementioned two types of prepregs, unidirectional and bidirectional PP reinforced continuous glass fiber (CGF), were used in the experiments. Figure 3-3 shows the bidirectional and unidirectional prepreg tapes before the laser assisted AM process. The bidirectional prepreg has 0/90 degree fiber orientation while the unidirectional prepreg only has fiber reinforcement oriented in one direction. The bidirectional tape is also thicker at 0.6 mm thickness compare to thickness of 0.3 mm for unidirectional tape. The PP matrix in the prepreg has a semi-crystalline structure and bonded by diffusion when heat and pressure is applied. This process involves heating the polymeric matrix at the interface to a viscous state, physically causing polymer chains to inter-diffuse by the compaction roller, and cooling it for consolidation [37], as described in Figure 3-4.

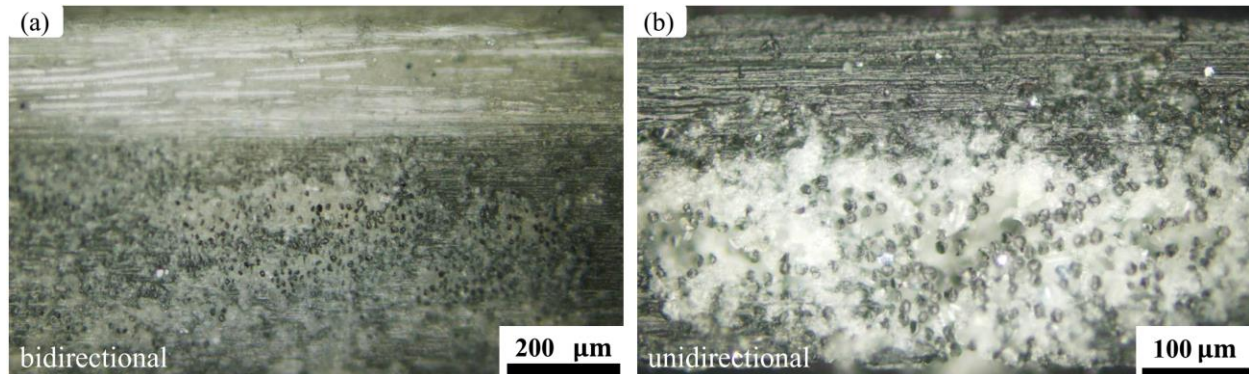


Figure 3-3 Optical microscope pictures of (a) bidirectional and (b) unidirectional GF/PP prepreg tapes before laser assisted AM, demonstrating the thickness and fiber orientation difference in them.

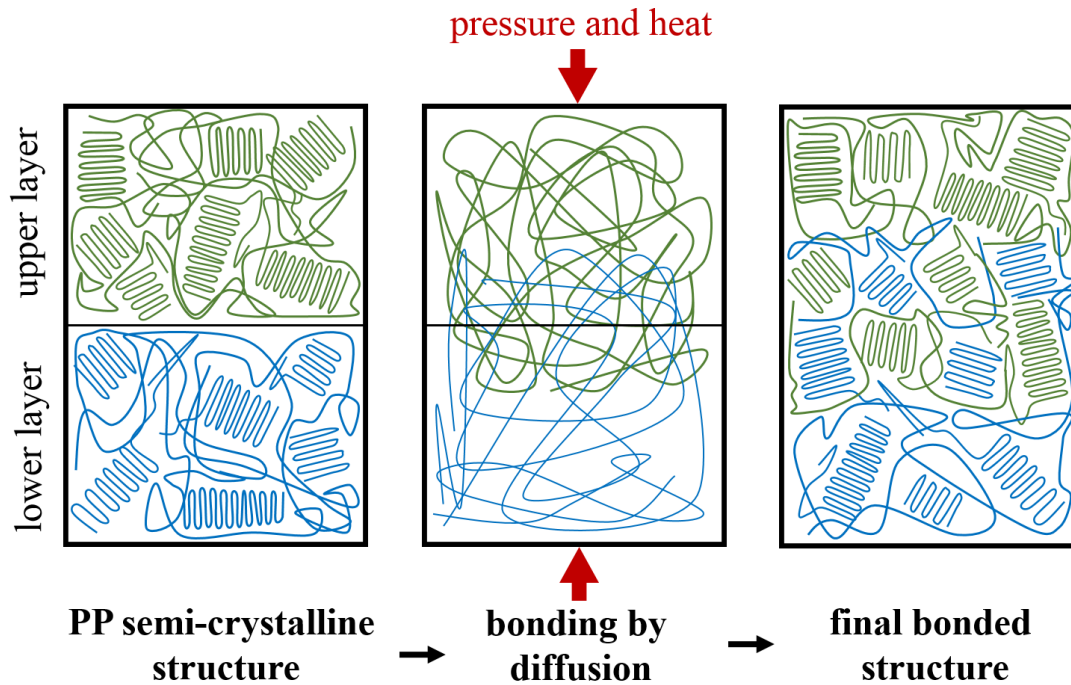


Figure 3-4 Bonding mechanism in laser assisted bonding of PP matrix

Figure 3-5 illustrates the cross sectional microstructure of the parts printed with unidirectional prepreg with 0/90 fiber orientation. The unidirectional tapes were laid on top of each other with 90° angle orientation in two principal fiber directions to achieve high strength in both directions. Microstructures of these specimen showed good interfacial diffusion between layers without any visible void and gap. Figure 3-5 a, and b also demonstrate the continuity of fibers in prepreg material and 3D printed parts. Thickness of the unidirectional prepreg tape is reduced to ~285 μm exhibiting only ~5% shrinkage in thickness. Cross-sectional microstructure of samples prepared with bidirectional prepreg is presented in Figure 3-6. It can be observed in Figure 3-6 (c), that the bonded prepregs form a solid structure without any void between the tapes with good interfacial fusion between layers. The bidirectional prepregs have fiber orientated in two principal direction noticeable in Figure 3-6 (a). The shrinkage in bidirectional samples was more noticeable at ~13% with the thickness of ~520 μm after laser bonding process. The proposed method delivers

excellent interfacial bonding between fibers and matrix as well as laminated layers with minimal void content. This method eliminates the necessity of post-processing for consolidation as reported in aforementioned LOM method [22, 38]. Excessive thermal energy had negative effects on the structural accuracy of the process due to dimensional change of molten material under compaction roller. Therefore, adequate bonding while maintaining dimensional accuracy is highly sensitive to process parameters.

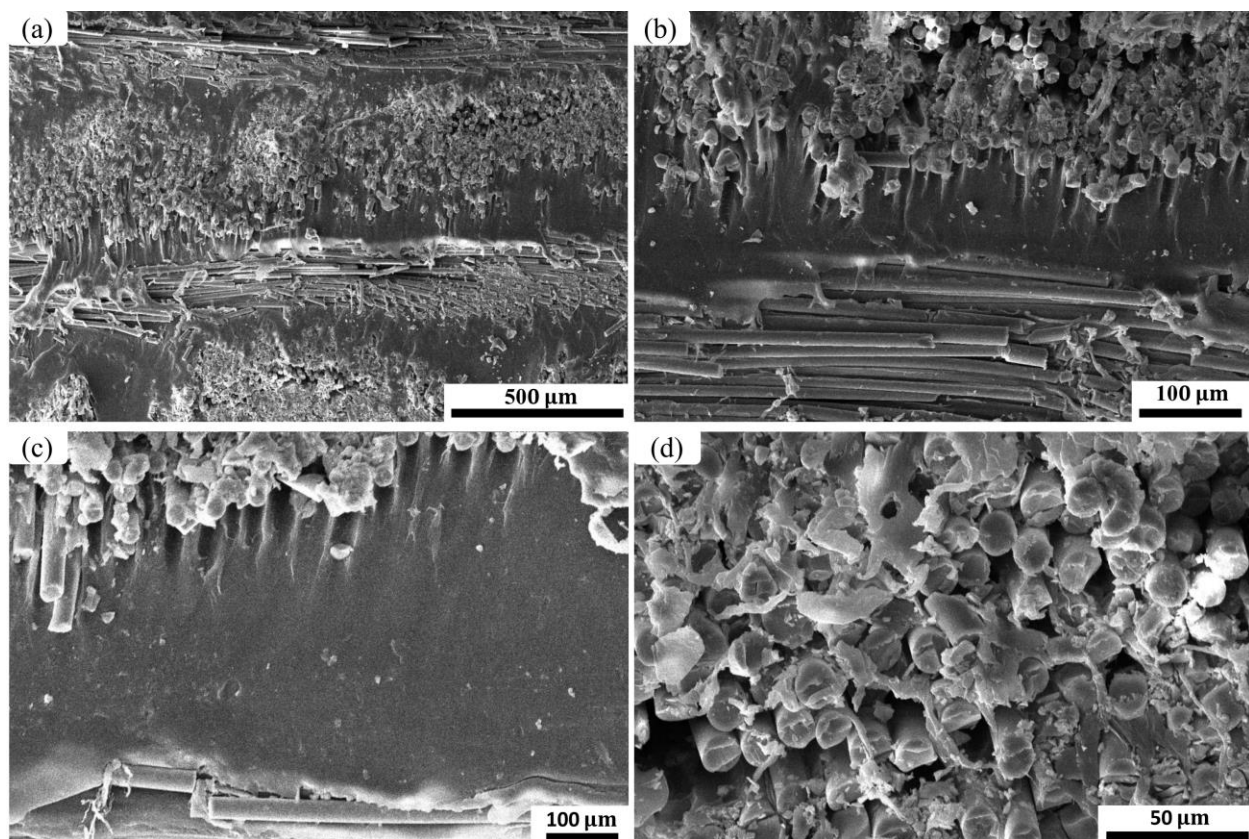


Figure 3-5 Cross-sectional SEM images of unidirectional samples demonstrating interfacial bonding after laser assisted additive manufacturing. (a) cross-ply fiber orientation (0/90) evident from cross-sectional micrograph, (b, c) interfacial area between two layers with 90° angle of fiber orientation, and (d) fibers in unidirectional tape.

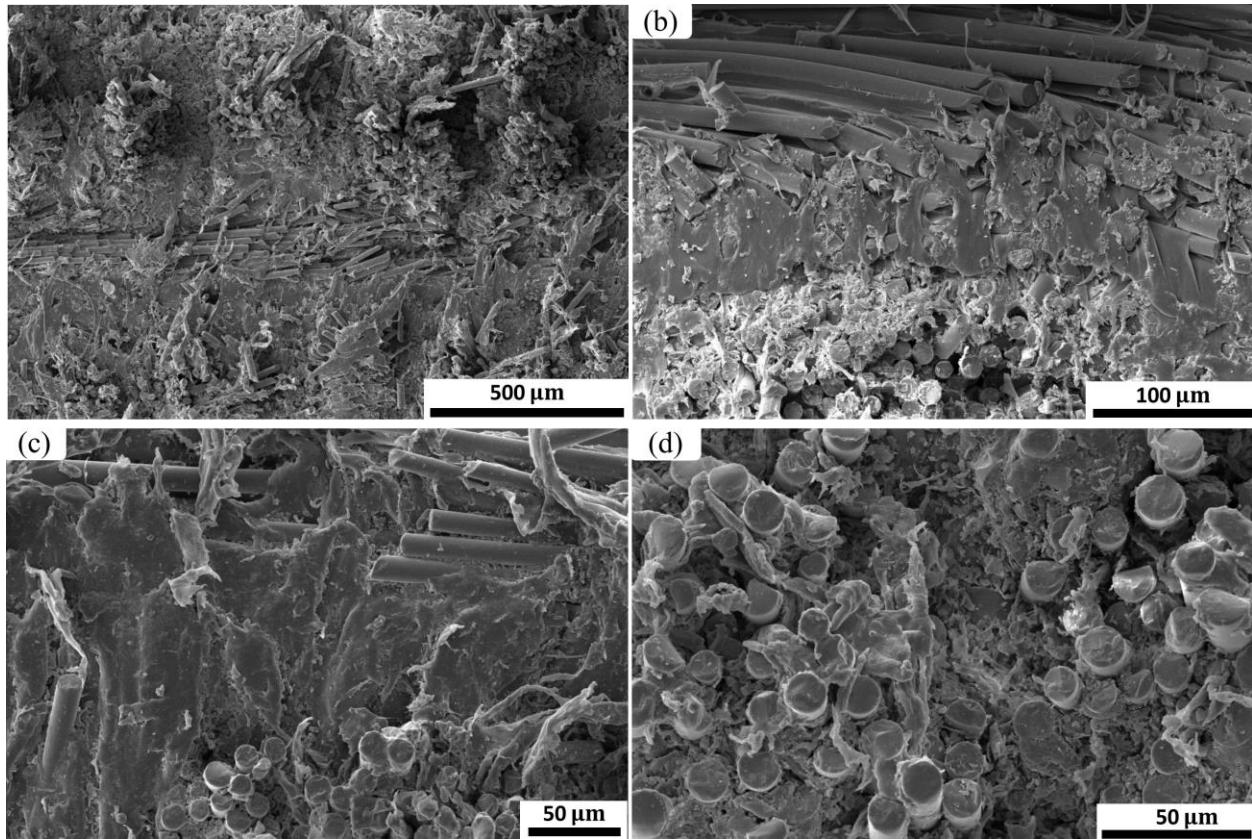


Figure 3-6 Cross-sectional SEM images of bidirectional samples demonstrating interfacial bonding after laser assisted additive manufacturing. (a) Cross section of the sample showing bonding structure of two tapes, (b, c) interfacial area between two tapes, and (d) fiber orientation and distribution in the bidirectional tape.

Bonding Strength

Bonding strength of laser bonded prepreg layers plays an important role for obtaining high strength required in functional components. The supplied prepreg composites are reinforced with continuous GF and exceptional mechanical properties can be achieved by ensuring strong interfacial bonding between prepreg layers. This section presents the results of two popular adhesion test, the T-peel test and single lap shear test, to evaluate the strength of laser bonding method implemented.

T-peel testing

The performance of 3D printed GF/PP composites are highly dependent on its interfacial properties, which were investigated by T-peel test (90°). Four laser power settings of 22, 24, 26, and 28 W and roller speed of 1, 2, 3, and 4 mm/s was selected for this test. The T-peel test was run at 5 mm/s. Figure 3-7 presents the test results of peel strength (N/mm). It can be observed that T-peel strength increases with higher range of laser power (26-28 W). Lower temperatures can be achieved with low laser power, leading to incomplete consolidation of polymer chains, and ultimately, inferior peel strength. It was noticed that substantial increase in laser power can melt the prepreg tape to a point that cause dimensional inaccuracy and considerable shrinkage in thickness. The average peel strength of over 3 and 2 N/mm was achieved for laser bonded prepreg GF/PP material in bidirectional and unidirectional form, respectively. Bidirectional prepregs showed higher peel strength relative to unidirectional counterpart, due to higher thermoplastic concentration which facilitates bond formation. Figure 3-7 (a) and (b) show the effect of laser power and confirm that increasing power to higher than 26 W does not offer any significant improvement in the peel strength. Figure 3-7 (c) and (d) illustrate the influence of roller speed with a fix laser power (26 W) on peel strength. It shows that decreasing the speed has positive effect on the peel strength with highest strength achieved in the range of 1-2 mm/s speed. With higher feed rate, there is not adequate time for consolidation of the prepreg layers. It can be interpreted that, for the given laser bonding setup full consolidation occurs at 26 W laser power and 2 mm/s roller speed and these parameters yielded the best peel strength for both laser bonded unidirectional and bidirectional GF/PP prepregs. T-peel test results in this work were evaluated against peel strength of the well-established hot compaction method for fiber reinforced PP reported by Swolfs, et al. [39]. Superior peel strength for bidirectional prepreg and comparable results for unidirectional

prepreg was achieved. Specifically, our method exhibited 50% higher peel strength than hot compaction for bidirectional prepregs and similar peel strength for unidirectional prepreg layers bonded by laser.

A typical adhesive failure mode after peel test is shown in Figure 3-8. It confirms the excellent bonding and adhesion of fiber-matrix and prepreg layers. The glass fiber in prepreg was damaged and fibers were pulled out of the matrix demonstrating the exceptional interfacial bonding. The SEM images presented in Figure 3-8 indicates the remarkable peel strength comparable to traditional manufacturing methods.

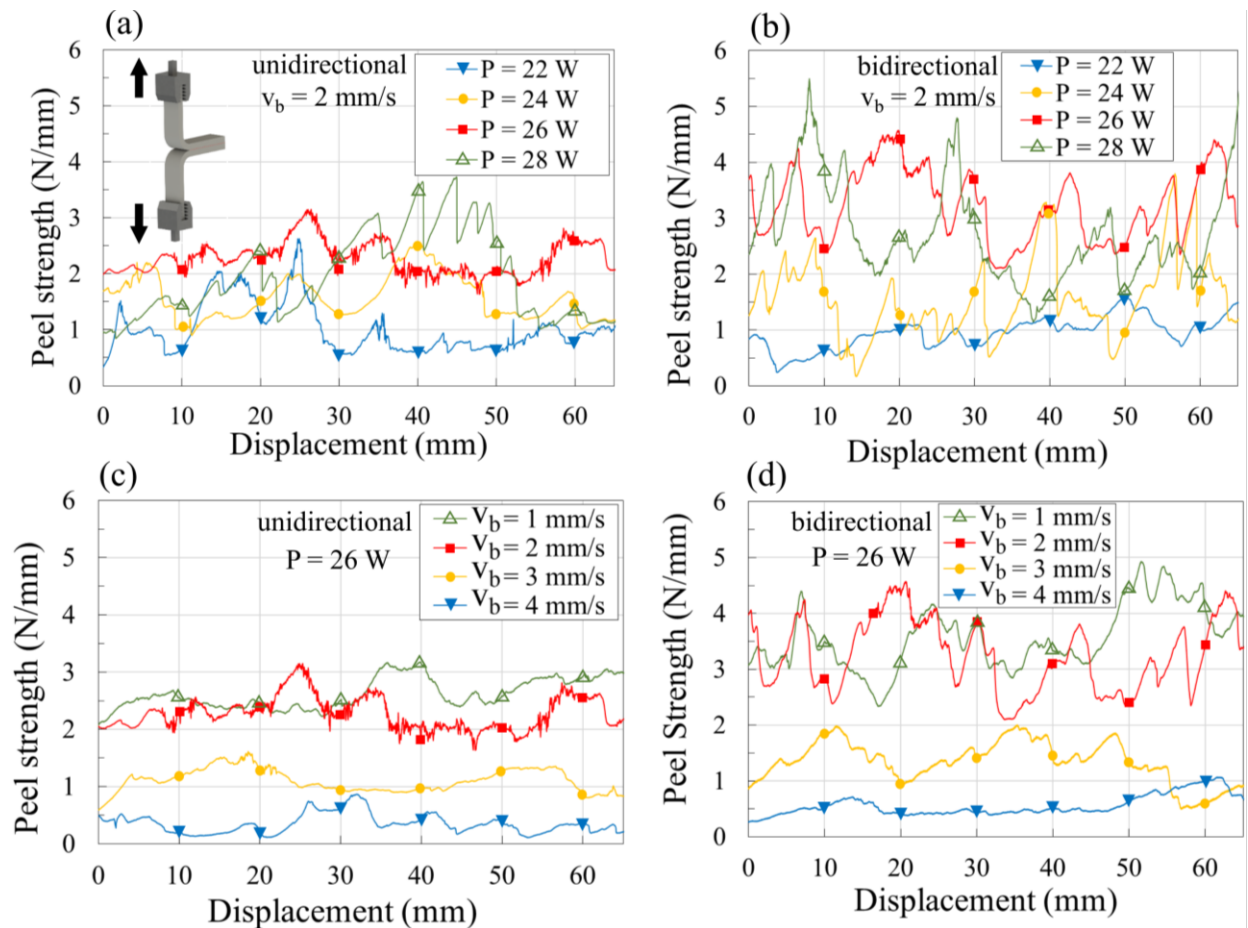


Figure 3-7 T-Peel test results and configuration using various laser powers and roller speeds for laser assisted AM parts; (a, b) the effect of laser power on peel strength of (a) unidirectional and (b) bidirectional samples; (c, d) the effect of roller speed on peel strength of (c) unidirectional and (d) bidirectional samples.

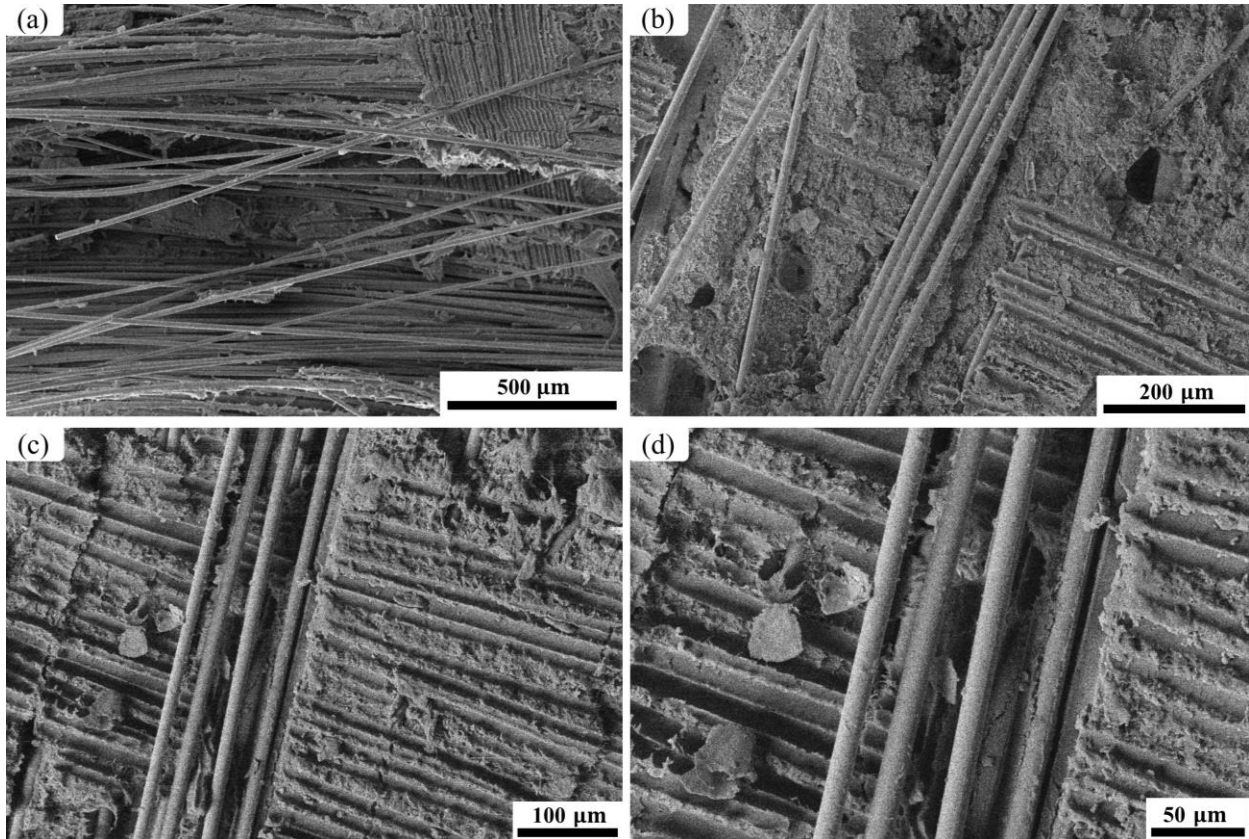


Figure 3-8 SEM images of T-peel test surface after adhesive failure. (a, b) The pulled out fibers from the surface resulted from T-peel test and (c, d) the thermoplastic matrix adhesive failure.

Lap shear strength (LSS)

Lap shear strength (LSS) testing, which involves axial pulling of the bonded specimen, is one of the most commonly test methods for investigating bond strength. LSS can be calculated by the following equation [40]:

$$\tau = \frac{F_{\max}}{L \times b} \left[\frac{N}{mm^2} \right] \quad (3-1)$$

where τ is lap shear strength, L is length of the overlap, b is width of the overlap, and F_{\max} is maximum tensile force. In order to access a better understanding of the laser bonding shear

strength in the AM method, benchmark LSS values of compression molded GF/PP studied by Hou and Friedrich [40] were compared with our work. LSS of the 3D printed specimen with laser bonding is presented in Figure 3-9 with respect to laser powers of 22, 24, 26, and 28 W and feed rate of 1, 2, 3, and 4 mm/s. When speed is fixed to 2 mm/s, Laser power below 22 W was found to be insufficient to initiate bonding, and increasing it to value over 28 W resulted in excessive thermal damage with a large heat affected zone (HAZ) and dimensional inaccuracy.

It can be interpreted that increasing laser power gradually increased the LSS with improved interfacial bonding between thermoplastic matrixes of two respective prepreg layers. However, it was noticed that increasing laser power over 26 W does not offer a substantial improvement in LSS for both unidirectional and bidirectional prepreps in agreement with T-peel test results. Unsurprisingly, LSS decreased at elevated speed resulted from partial consolidation and speed range of 1-2 mm/s generated the best results for LSS. Unidirectional prepreps exhibited lower LSS compared to bidirectional counterpart, which may be due to more volume ratio of PP matrix responsible for better bonding. Nevertheless, LSS obtained from laser bonding in present method approached the value of 9.87 MPa in compression molding stated by Hou and Friedrich [40] for CGF/PP composites. Precisely, using the optimum settings of 26 W power and 2 mm/s speed, 96 % and 93 % of compression molded LSS benchmark were obtained with bidirectional and unidirectional prepreg, respectively.

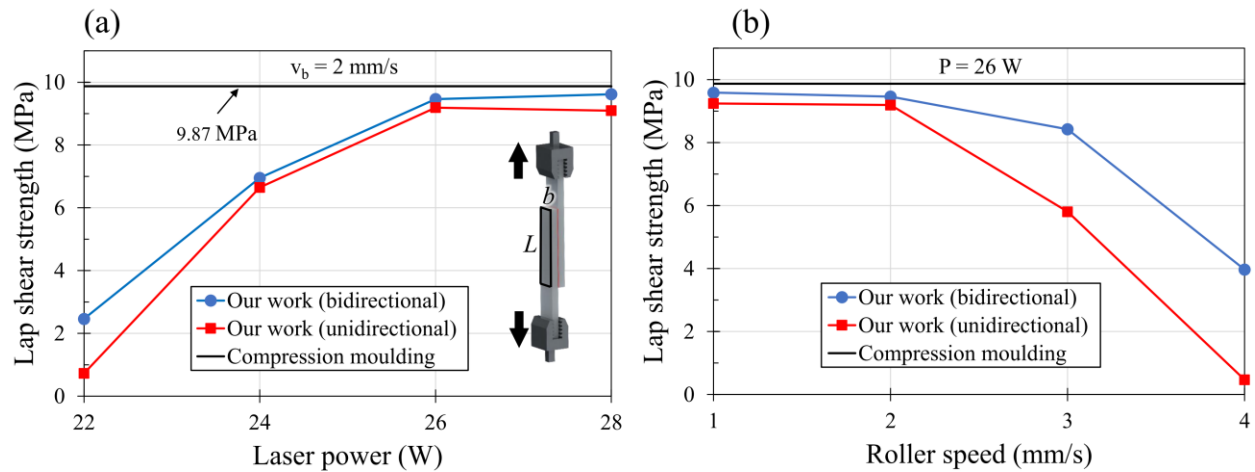


Figure 3-9 Lap shear strength of the laser bonded prepreg as a function of (a) laser power and (b) roller speed as compared with compression moulding [40].

Mechanical properties

Tensile and flexural properties of the 3D printed components by newly proposed method were characterized. The detailed results and comparison with other works are presented in this section.

Tensile properties

The tensile strength was tested by the universal testing machine using 4 samples for each bidirectional and unidirectional prepreg samples to ensure the reliability of test results. Figure 3-10 shows the printed tensile bars and their dimensions for both unidirectional and bidirectional prepreps. Fiber orientation in the tensile bars was in two principle directions, in the load direction and vertical to the load, regardless of the prepreg type. Thus, only about 50% of the fibers carried the load in the tensile test for more realistic results similar to real applications where components are under tension. The fiber orientation in the tensile test samples can be observed in Figure 3-12, which shows the tensile fracture surface obtained by SEM after tensile testing for tensile bars

prepared with unidirectional and bidirectional prepreg. For both prepreg types, fiber pullout and breakage were observed microscopically in the SEM images. It indicates that only one principal fiber orientation carry the tensile load during testing. Long fiber length can be observed in the fracture surface, indicating poor interfacial adhesion between GF and PP matrix. This behavior agreed with the previous report for extruded CGF/PP and 3D printed continuous carbon fiber/PLA using FDM [26, 41].

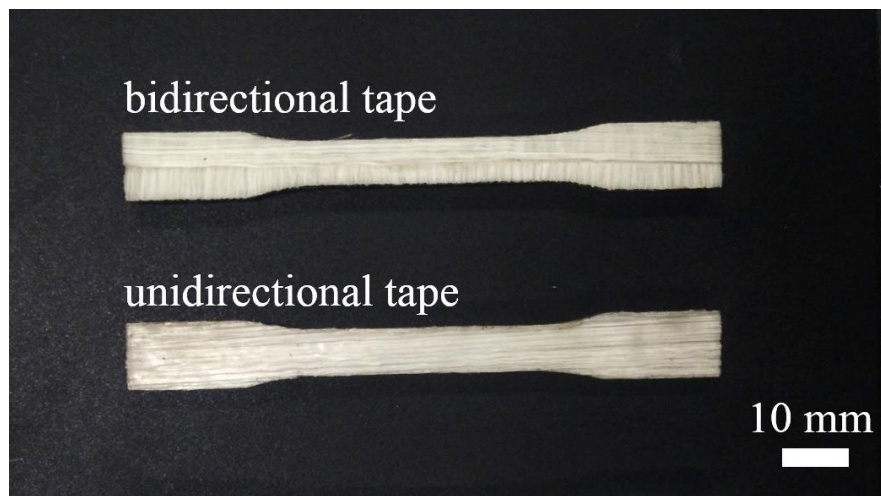


Figure 3-10 Tensile bars used for tensile strength measurement prepared with bidirectional and unidirectional prepreg tapes.

The stress-strain curve of the material, as presented in Figure 3-11 (a), indicated higher strength in the parts 3D printed by unidirectional tapes owing to the higher glass fiber ratio. There were two regions marked in the curves associated with PP and GF similar to previous works on FDM 3D printing of CFRTPCs reported in Li, et al. [27]. The most probable reason can be debonding fiber-matrix interface at the limit value of interface strength causing a slight decrease in the curve slope [27], supported by SEM micrographs of the fracture surface in Figure 3-12, in which fibers are completely snapped out of the matrix. During the test the stress in the samples may rise to the higher than fiber-matrix interface strength causing interfacial failing, but, fibers

and matrix have not failed yet, and most of the load is still supported by fibers. Finally, both GF and PP reach the yield point and break. The GF reinforced samples are entirely snapped by the external tensile load and most of the fiber-matrix interface are damaged (Figure 3-12). It is worth noting that, considerably higher tensile strength and modulus can be reached if all the fibers were oriented in load direction. The proposed AM method for CGF reinforcement of PP was compared with FDM printing of short GF/PP [14] and other traditional methods of composite manufacturing [2, 3, 14] in Figure 3-11 (b). The proposed method offers substantially superior strength and higher Young's modulus relative to FDM of short GF/PP owing to continuous fibers (CF) in the prepreg material. Tensile strength of our 3D printed parts were close to part produced by injection molding with short fiber (SF) and long fiber (LF), compression molding and stamping with CF; however, our method exhibits a lower tensile modulus. Specifically, the tensile modulus is 45 % lower than injection molding and 57% lower than stamping and compression molding, in average. Our method also was compared with continuous carbon fiber reinforced FDM parts with ABS and PLA resin. Tensile strength of FDM of continuous carbon fiber/PLA was in the range of our work with substantially higher tensile modulus (233 %) due to use of carbon fiber. However, in the case of FDM parts with ABS resin, tensile strength and tensile modulus is the same range as our work with bidirectional prepreg. Overall, the proposed method offers higher tensile strength than injection molding with short or long glass fiber and reaches the level of compaction molding and stamping with continuous fiber.

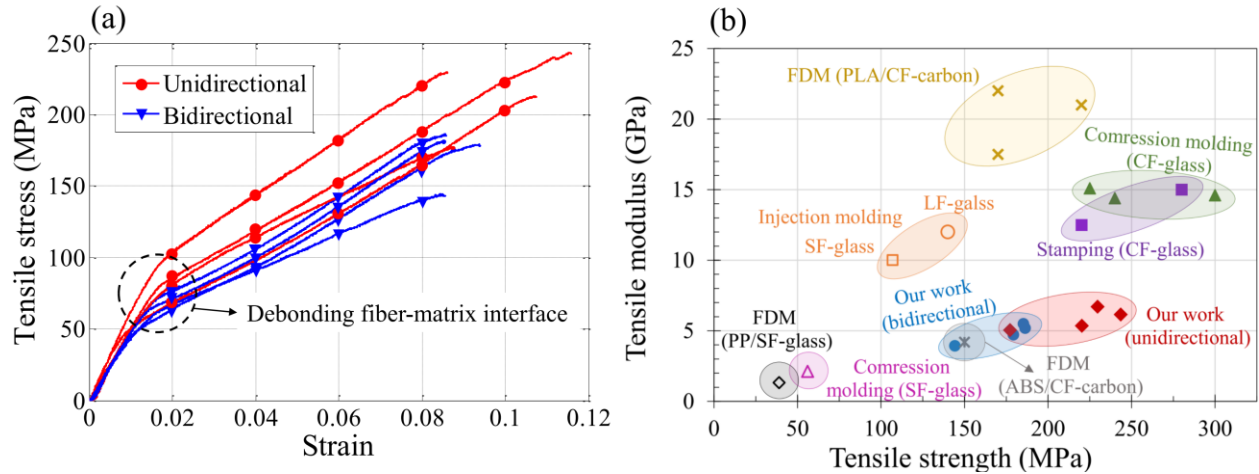


Figure 3-11 Tensile properties of 3D printed samples fabricated by our proposed method. (a) Stress-strain curve showing the ultimate tensile strength of 3D printed samples, and (b) tensile modulus versus strength in comparison with FDM (SF) [14], compression molding (SF) [14], continuous GF compression molding and stamped [2], injection molding with SF and LF [3], FDM (ABS/CF-carbon) [42], and FDM (PLA/CF-carbon) [26].

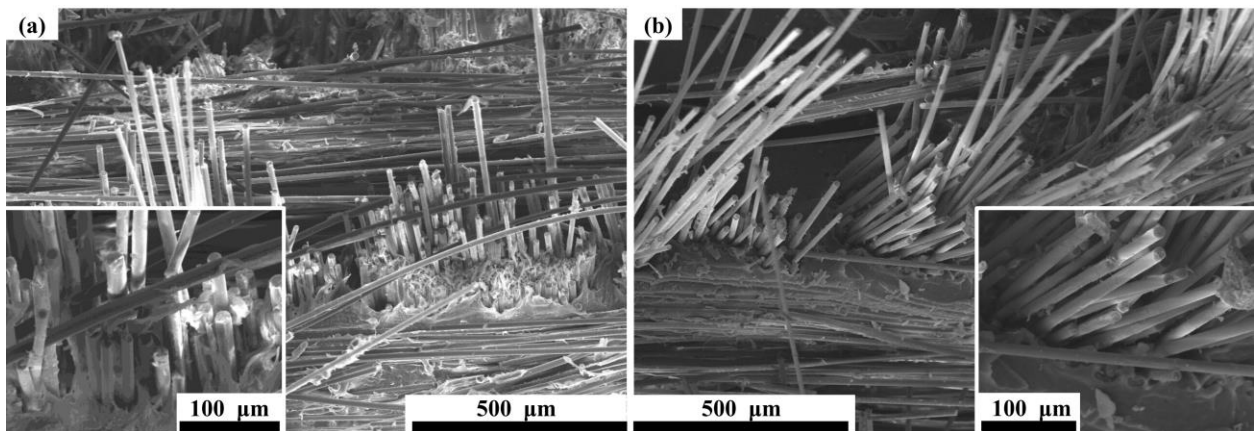


Figure 3-12 Cross-sectional microstructure of the tensile fracture surface: (a) bidirectional prepreg and (b) unidirectional prepreg.

Flexural properties

The flexural properties of our method are reported and compared with benchmark data for compression molding, stamping [2], and injection molding [43], and FDM of continuous carbon

fiber reinforced thermoplastics [28, 42]. Flexural behavior of the continuous GF/PP is highly dependent on the bonding mechanism and its strength. Figure 3-13 (a) presents the stress-curve obtained during 3-point bending test. Unidirectional and bidirectional samples showed different behavior during the test. Predictably, specimen with unidirectional prepreg exhibited higher strength due to higher GF volume ratio. The results obtained from 3-point bending test indicated comparable strength to injection molding with LF and stamping with CF. However, compression molding with CF was able to achieve higher strength range may be due to stronger bonding between layers resulted from longer compression time and higher pressure during processing. Surprisingly, this method exhibited higher stiffness with relatively high flexural modulus compared to compression molding and stamping. As data suggests, using both unidirectional and bidirectional prepreg, similar flexural strength was achieved, but, unidirectional higher GF volume ratio contributed to a higher flexural modulus. Interestingly, higher GF concentration in unidirectional prepreg did not achieve higher strength unlike modulus. We believe that higher bonding strength using bidirectional prepreg due to more thermoplastic matrix concentration was responsible for these results which is in agreement with T-peel test results. This result could also be observed in the benchmark data found in the literature. Although the injection molding using LF instead of CF in compression molding and stamping has lower GF concentration, it exhibited ~50% higher flexural modulus; but, flexural strength was in the same range due to much better bonding in injection molding compared to laminar structure of other mentioned methods. When compared to continuous carbon fiber reinforced FDM parts with both ABS and PLA resin, flexural modulus is substantially lower than laser assisted AM, and flexural strength of samples with ABS and PLA resins is ~30% and ~10% lower than our work, respectively. This superior flexural properties is due to the better interfacial bonding relative to FDM. In brief, our proposed method

was capable of 3D printing parts, and comparable in flexural properties with traditional manufacturing methods of CFRTPCs.

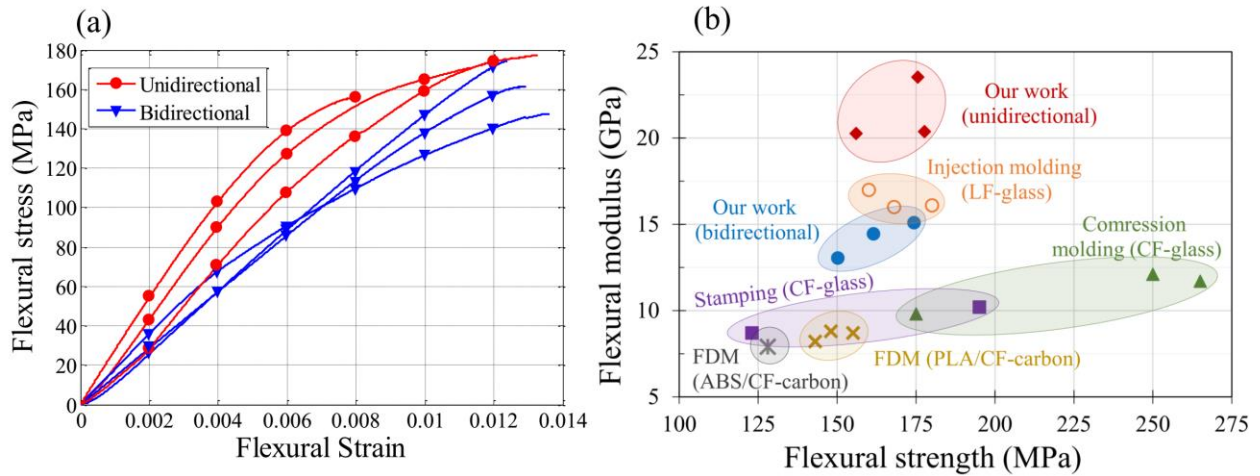


Figure 3-13 Flexural properties obtained from 3-point bending test. (a) Flexural stress-strain curve indicating flexural strength, and (b) comparison of flexural strength and modulus of our method (using unidirectional and bidirectional prepregs) with compression molding (CF-glass) [2], stamping (CF-glass) [2], injection molding (LF-glass) [3], FDM (ABS/CF-carbon) [42], and FDM (PLA/CF-carbon) [28].

Overall picture

The results of all of the tests on mechanical properties are presented and compared with pure PP produced by compression molding in Table 3-1. In general, unidirectional samples exhibited better properties in our tests, and it can be seen that CGF reinforcement has a substantial effect on the mechanical behavior of the pure PP thermoplastic. It can increase tensile strength, tensile modulus, flexural strength, and flexural modulus, by 547%, 247%, 253%, and 750%, respectively.

Table 3-1 Mechanical properties of continuous GF/PP by laser assisted AM compared with pure PP manufactured by compression molding.

	Our work (bidirectional GF)	Our work (unidirectional GF)	Compression molding (pure PP)
Tensile strength	173.7 ± 19.9 MPa	217.6 ± 28.6 MPa	32.3 ± 1.0 Mpa [44]
Tensile modulus	4.9 ± 0.7 GPa	5.9 ± 0.8 GPa	1.7 ± 0.1 GPa [45]
Flexural strength	150.7 ± 30.5 MPa	169.7 ± 48.6 MPa	48.0 ± 0.7 MPa [44]
Flexural modulus	15.3 ± 1.0 GPa	21.4 ± 5.1 GPa	1.8 ± 0.1 GPa [45]

Conclusions

An innovative method for additive manufacturing of CFRTPCs with the intention of solving the fundamental issue in 3D printing of fiber composites was proposed by using prepreg composite. Successive layers of narrow prepreg tapes were heated using a CO₂ laser and bonded by compaction roller to form a laminated 3D object. Designed shape of each layer was obtained by laser cutting prior to adding the next layer. In this work, two types of GF/PP prepreps (unidirectional and bidirectional) were chosen to demonstrate this method. The microstructure characterized by scanning electron microscopy showed superior bonding of prepreg lays with no visible void or gap, which is a substantial improvement compared to other 3D printing techniques, such as FDM and etc.

A series of tests, namely, T-peel, Lap shear strength, tensile, and 3-point bending tests were performed on the parts prepared using this method. The following is a brief summary of the test results:

- Adhesion of laser bonded prepreg layers was tested through a series of T-peel tests, and then compared to compaction molding. Peel strength was 50 % higher for bidirectional prepreg and

nearly equal for the unidirectional type. Increasing laser bonding power to 26 W with fixed roller speed of 2 mm/s resulted in stronger adhesion. Exceeding 26 W showed no adhesion improvement and resulted in dimensional inaccuracy.

- Single lap shear tests indicated comparable LSS to compaction molding for both unidirectional and bidirectional prepregs.
- Our proposed method was capable of achieving superior tensile strength and modulus compared to FDM parts reinforced with SF and similar tensile strength and lower modulus relative to traditional composite manufacturing methods with continuous fiber reinforcement.
- Flexural strength of our method fell below compaction molding by 30% on average; however, flexural modulus can be up to 100% higher, indicating high flexural stiffness.

In conclusion, this proposed method has a high potential in establishing AM as a robust technique for manufacturing of CFRTPC functional components. It can find applications in automotive, aerospace, marine, and construction industries providing excellent rigidity, light weight, versatility of design and material choice. This paper provides a novel path in the field of composite 3D printing.

References

- [1] F. Perrin, M. N. Bureau, J. Denault, and J. I. Dickson, "Mode I interlaminar crack propagation in continuous glass fiber/polypropylene composites: temperature and molding condition dependence," *Composites Sci. Technol.*, vol. 63, no. 5, pp. 597-607, 4// 2003, doi: [http://dx.doi.org/10.1016/S0266-3538\(02\)00255-5](http://dx.doi.org/10.1016/S0266-3538(02)00255-5).
- [2] M. N. Bureau and J. Denault, "Fatigue resistance of continuous glass fiber/polypropylene composites: consolidation dependence," *Composites Sci. Technol.*, vol. 64, no. 12, pp. 1785-1794, 9// 2004, doi: <http://dx.doi.org/10.1016/j.compscitech.2004.01.016>.
- [3] J. L. Thomason, "The influence of fibre length and concentration on the properties of glass fibre reinforced polypropylene: 5. Injection moulded long and short fibre PP," *Composites Part A: Applied Science and Manufacturing*, vol. 33, no. 12, pp. 1641-1652, 12// 2002, doi: [http://dx.doi.org/10.1016/S1359-835X\(02\)00179-3](http://dx.doi.org/10.1016/S1359-835X(02)00179-3).

- [4] R. A. Schweizer, "Glass Fiber Length Degradation in Thermoplastics Recessing," *Polymer-Plastics Technology and Engineering*, vol. 18, no. 1, pp. 81-91, 1982/01/01 1982, doi: 10.1080/03602558208067712.
- [5] C. Yang, X. Tian, T. Liu, Y. Cao, and D. Li, "3D printing for continuous fiber reinforced thermoplastic composites: mechanism and performance," *Rapid Prototyping Journal*, vol. 23, no. 1, 2017.
- [6] D. Lin *et al.*, "Three-Dimensional Printing of Complex Structures: Man Made or toward Nature?," *ACS Nano*, vol. 8, no. 10, pp. 9710-9715, 2014/10/28 2014, doi: 10.1021/nn504894j.
- [7] J. Cerneels, A. Voet, J. Ivens, and J.-P. Kruth, "Additive manufacturing of thermoplastic composites," in *Composites Week@ Leuven*, 2013: KU Leuven, pp. 1-7.
- [8] W. Zhong, F. Li, Z. Zhang, L. Song, and Z. Li, "Short fiber reinforced composites for fused deposition modeling," *Materials Science and Engineering: A*, vol. 301, no. 2, pp. 125-130, 2001.
- [9] M. Nikzad, S. Masood, and I. Sbarski, "Thermo-mechanical properties of a highly filled polymeric composites for fused deposition modeling," *Materials & Design*, vol. 32, no. 6, pp. 3448-3456, 2011.
- [10] M. Shofner, F. Rodriguez-Macias, R. Vaidyanathan, and E. Barrera, "Single wall nanotube and vapor grown carbon fiber reinforced polymers processed by extrusion freeform fabrication," *Composites Part A: Applied Science and Manufacturing*, vol. 34, no. 12, pp. 1207-1217, 2003.
- [11] H. L. Tekinalp *et al.*, "Highly oriented carbon fiber-polymer composites via additive manufacturing," *Composites Sci. Technol.*, vol. 105, pp. 144-150, 2014.
- [12] F. Ning, W. Cong, J. Qiu, J. Wei, and S. Wang, "Additive manufacturing of carbon fiber reinforced thermoplastic composites using fused deposition modeling," *Composites Part B: Engineering*, vol. 80, pp. 369-378, 10// 2015, doi: <https://doi.org/10.1016/j.compositesb.2015.06.013>.
- [13] Z. Quan *et al.*, "Microstructural design and additive manufacturing and characterization of 3D orthogonal short carbon fiber/acrylonitrile-butadiene-styrene preform and composite," *Composites Sci. Technol.*, vol. 126, pp. 139-148, 4/1/ 2016, doi: <https://doi.org/10.1016/j.compscitech.2016.02.021>.
- [14] O. S. Carneiro, A. F. Silva, and R. Gomes, "Fused deposition modeling with polypropylene," *Materials & Design*, vol. 83, pp. 768-776, 10/15/ 2015, doi: <http://dx.doi.org/10.1016/j.matdes.2015.06.053>.

- [15] B. G. Compton and J. A. Lewis, "3D-Printing of Lightweight Cellular Composites," *Adv. Mater.*, vol. 26, no. 34, pp. 5930-5935, 2014, doi: 10.1002/adma.201401804.
- [16] C. Yan, L. Hao, L. Xu, and Y. Shi, "Preparation, characterisation and processing of carbon fibre/polyamide-12 composites for selective laser sintering," *Composites Sci. Technol.*, vol. 71, no. 16, pp. 1834-1841, 11/14/ 2011, doi: <https://doi.org/10.1016/j.compscitech.2011.08.013>.
- [17] S. R. Athreya, K. Kalaitzidou, and S. Das, "Processing and characterization of a carbon black-filled electrically conductive Nylon-12 nanocomposite produced by selective laser sintering," *Materials Science and Engineering: A*, vol. 527, no. 10–11, pp. 2637-2642, 4/25/ 2010, doi: <https://doi.org/10.1016/j.msea.2009.12.028>.
- [18] S. Yuan, J. Bai, C. Chua, J. Wei, and K. Zhou, "Material Evaluation and Process Optimization of CNT-Coated Polymer Powders for Selective Laser Sintering," *Polymers*, vol. 8, no. 10, p. 370, 2016. [Online]. Available: <http://www.mdpi.com/2073-4360/8/10/370>.
- [19] L. Lü, J. Y. H. Fuh, and Y. S. Wong, "Improvements of Mechanical Properties by Reinforcements," in *Laser-Induced Materials and Processes for Rapid Prototyping*. Boston, MA: Springer US, 2001, pp. 67-88.
- [20] M. L.-J. Thomas, W. D. Bruce, and S. T. Richard, "3D printed components with ultrasonically arranged microscale structure," *Smart Mater. Struct.*, vol. 25, no. 2, p. 02LT01, 2016. [Online]. Available: <http://stacks.iop.org/0964-1726/25/i=2/a=02LT01>.
- [21] E. J. Barbero, *Introduction to composite materials design*. CRC press, 2010.
- [22] D. Klosterman, R. Chartoff, G. Graves, N. Osborne, and B. Priore, "Interfacial characteristics of composites fabricated by laminated object manufacturing," *Composites Part A: Applied Science and Manufacturing*, vol. 29, no. 9, pp. 1165-1174, 1998.
- [23] F. O. Sonmez and H. T. Hahn, "Thermomechanical analysis of the laminated object manufacturing (LOM) process," *Rapid Prototyping Journal*, vol. 4, no. 1, pp. 26-36, 1998, doi: doi:10.1108/13552549810197541.
- [24] S. H. Huang, P. Liu, A. Mokeddar, and L. Hou, "Additive manufacturing and its societal impact: a literature review," *The International Journal of Advanced Manufacturing Technology*, journal article vol. 67, no. 5, pp. 1191-1203, 2013, doi: 10.1007/s00170-012-4558-5.
- [25] K.-i. Mori, T. Maeno, and Y. Nakagawa, "Dieless forming of carbon fibre reinforced plastic parts using 3D printer," *Procedia Engineering*, vol. 81, pp. 1595-1600, 2014.

- [26] R. Matsuzaki *et al.*, "Three-dimensional printing of continuous-fiber composites by in-nozzle impregnation," *Scientific Reports*, vol. 6, p. 23058, 03/11 2016, doi: 10.1038/srep23058.
- [27] N. Li, Y. Li, and S. Liu, "Rapid prototyping of continuous carbon fiber reinforced polylactic acid composites by 3D printing," *J. Mater. Process. Technol.*, vol. 238, pp. 218-225, 12// 2016, doi: <http://dx.doi.org/10.1016/j.jmatprotec.2016.07.025>.
- [28] X. Tian, T. Liu, C. Yang, Q. Wang, and D. Li, "Interface and performance of 3D printed continuous carbon fiber reinforced PLA composites," *Composites Part A: Applied Science and Manufacturing*, vol. 88, pp. 198-205, 9// 2016, doi: <http://dx.doi.org/10.1016/j.compositesa.2016.05.032>.
- [29] A. Comer *et al.*, "Mechanical characterisation of carbon fibre-PEEK manufactured by laser-assisted automated-tape-placement and autoclave," *Composites Part A: Applied Science and Manufacturing*, vol. 69, pp. 10-20, 2015.
- [30] M. STEYER, M. DUBRATZ, A. SCHÜTTE, C. WENZEL, and C. BRECHER, "Laser-assisted thermoplastic tape-laying systems," *JEC composites*, no. 47, pp. 39-41, 2009.
- [31] M. A. Schledjewski R, "Thermoplastic tape placement by means of diode laser heating," in *Proceedings SAMPE conference*, Baltimore, Maryland, USA, 18-21 May 2009 18-21 May 2009.
- [32] S.-L. Gao and J.-K. Kim, "Cooling rate influences in carbon fibre/PEEK composites. Part 1. Crystallinity and interface adhesion," *Composites Part A: Applied Science and Manufacturing*, vol. 31, no. 6, pp. 517-530, 6// 2000, doi: [https://doi.org/10.1016/S1359-835X\(00\)00009-9](https://doi.org/10.1016/S1359-835X(00)00009-9).
- [33] W. Groupe, G. Vanden Poel, L. Warnet, and R. Akkerman, "On crystallisation and fracture toughness of poly (phenylene sulphide) under tape placement conditions," *Plastics, Rubber and Composites*, vol. 42, no. 7, pp. 282-288, 2013.
- [34] W. J. B. Groupe, L. Warnet, R. Akkerman, S. Wijskamp, and J. S. M. Kok, "Weld Strength Assessment for Tape Placement," *International Journal of Material Forming*, journal article vol. 3, no. 1, pp. 707-710, 2010, doi: 10.1007/s12289-010-0868-z.
- [35] W. J. B. Groupe, L. L. Warnet, B. Rietman, H. A. Visser, and R. Akkerman, "Optimization of the tape placement process parameters for carbon-PPS composites," *Composites Part A: Applied Science and Manufacturing*, vol. 50, pp. 44-53, 7// 2013, doi: <https://doi.org/10.1016/j.compositesa.2013.03.003>.
- [36] F. Rosselli, M. H. Santare, and S. I. Güçeri, "Effects of processing on laser assisted thermoplastic tape consolidation," *Composites Part A: Applied Science and Manufacturing*, vol. 28, no. 12, pp. 1023-1033, 1997.

- [37] A. Yousefpour, M. Hojjati, and J.-P. Immarigeon, "Fusion Bonding/Welding of Thermoplastic Composites," *J. Thermoplast. Compos. Mater.*, vol. 17, no. 4, pp. 303-341, 2004, doi: doi:10.1177/0892705704045187.
- [38] D. Klosterman *et al.*, "Direct Fabrication of Polymer Composite Structures with Cuwed LOM," 1999.
- [39] Y. Swolfs *et al.*, "The importance of bonding in intralayer carbon fibre/self-reinforced polypropylene hybrid composites," *Composites Part A: Applied Science and Manufacturing*, vol. 76, pp. 299-308, 9// 2015, doi: <http://dx.doi.org/10.1016/j.compositesa.2015.06.017>.
- [40] M. Hou and K. Friedrich, "Resistance welding of continuous glass fibre-reinforced polypropylene composites," *Composites Manufacturing*, vol. 3, no. 3, pp. 153-163, // 1992, doi: [http://dx.doi.org/10.1016/0956-7143\(92\)90078-9](http://dx.doi.org/10.1016/0956-7143(92)90078-9).
- [41] A. Arbelaiz, B. Fernández, G. Cantero, R. Llano-Ponte, A. Valea, and I. Mondragon, "Mechanical properties of flax fibre/polypropylene composites. Influence of fibre/matrix modification and glass fibre hybridization," *Composites Part A: Applied Science and Manufacturing*, vol. 36, no. 12, pp. 1637-1644, 12// 2005, doi: <http://dx.doi.org/10.1016/j.compositesa.2005.03.021>.
- [42] C. Yang, X. Tian, T. Liu, Y. Cao, and D. Li, "3D printing for continuous fiber reinforced thermoplastic composites: mechanism and performance," *Rapid Prototyping Journal*, vol. 23, no. 1, pp. 209-215, 2017, doi: doi:10.1108/RPJ-08-2015-0098.
- [43] J. L. Thomason, "The influence of fibre length and concentration on the properties of glass fibre reinforced polypropylene. 6. The properties of injection moulded long fibre PP at high fibre content," *Composites Part A: Applied Science and Manufacturing*, vol. 36, no. 7, pp. 995-1003, 7// 2005, doi: <http://dx.doi.org/10.1016/j.compositesa.2004.11.004>.
- [44] J. L. Thomason, M. A. Vlug, G. Schipper, and H. G. L. T. Krikor, "Influence of fibre length and concentration on the properties of glass fibre-reinforced polypropylene: Part 3. Strength and strain at failure," *Composites Part A: Applied Science and Manufacturing*, vol. 27, no. 11, pp. 1075-1084, 1996/01/01 1996, doi: [http://dx.doi.org/10.1016/1359-835X\(96\)00066-8](http://dx.doi.org/10.1016/1359-835X(96)00066-8).
- [45] J. L. Thomason and M. A. Vlug, "Influence of fibre length and concentration on the properties of glass fibre-reinforced polypropylene: 1. Tensile and flexural modulus," *Composites Part A: Applied Science and Manufacturing*, vol. 27, no. 6, pp. 477-484, 1996/01/01 1996, doi: [http://dx.doi.org/10.1016/1359-835X\(95\)00065-A](http://dx.doi.org/10.1016/1359-835X(95)00065-A).

Chapter 4 - Additive manufacturing of High Strength Carbon Fiber Composites

The emerging field of 3D printing (also known as additive manufacturing) carbon fiber reinforced polymers (CFRPs) offers unparalleled flexibility in achieving complex geometries and high mechanical performance suitable for aerospace [1], automotive [2], marine [3], and civil engineering [4] industries, unattainable by traditional manufacturing methods [5]. The vision of inexpensive and high performance structural composites without the need of expensive custom molds and post machining processes associated with conventional methods [6] is enabled by various 3D printing techniques [5]. A vast majority of 3D printed CFRP composites comprises pre-blended polymer filament, resin, or powders with short carbon fibers (SCFs) for commercial 3D printers, including fused deposition modeling (FDM) [7-9], stereolithography (SLA) [10, 11], extrusion [12], and selective laser sintering (SLS) [13, 14] demonstrating relative improvements in mechanical performance over pure resin [13, 14]. However, pre-blended resins imposes several issues and complications when using commercial 3D printers. Presence of fibers in the filament for FDM reduces tape swelling at the printing head during the material deposition and increases the filament stiffness which further complicates the process and reduces the printing quality [15]. These composite filaments also cause micro voids inside the beads in addition to regular voids between beads and layers, which are potential spots for stress concentration and failure. Furthermore, SCF reinforcement itself is not adequate for ultrahigh strength structures and only aligned continuous carbon fiber (CCF) reinforced components can enable structural load bearing applications. The majority of the research efforts for integrating CCF reinforcement was focused on FDM, where either prepreg filaments with CCF were used [16], or CCF was supplied separately

and mixed with the molten polymeric resins inside the printing head [17, 18]. However, FDM is also known to have weak interfacial bonding and is associated with void formation amongst the deposited layers [7]. These limitations call for an alternative 3D printing of CFRP composites technique, which can manufacture lightweight and ultrahigh strength structural materials with high weight ratio of CCF, decent interfacial bonding, low void content, and controlled alignment of carbon fibers in each layer. Therefore, we proposed a laser assisted additive manufacturing method to concurrently achieve these key features.

Herein, we reported a novel approach for 3D printing of CFRP using prepreg composite sheets to fabricate free standing laminated structures. This process was inspired by laminated object manufacturing (LOM), however, the bonding process was modified for a more efficient consolidation of prepreg sheets. It began with the laser cutting of prepreg sheets based on the sliced CAD geometry (Figure 4-1 (a)), similar to LOM. Each prepreg layer was then stacked on top the previous layer and bonded by a collimated laser beam and a consolidation roller (Figure 4-1 (b) and (c)), unlike the LOM that bonds the layers with a hot roller and bonders. There was no post processing required after the 3D printing process, as appose to LOM which requires post heat treatment in order to cure the bonders for full consolidation. Fiber reinforced epoxy composites have been already produced by LOM successfully, however, additional heat treatment was required to fully cure the epoxy resin and consolidate the prepreg layers [19, 20]. We demonstrated a comparable method by utilizing continuous glass fiber reinforced thermoplastic in our previous work [21]. In that work, we used prepreg tape and successively laser bonded the tape strips. After covering the entire surface of each layer with prepreg tape, the precise 2D shape was cut using a laser cutting system. However, in the current work, prepreg sheets were used instead of tape and laser cutting took place before the laser bonding process. This method improved the flexibility of

the process in producing over-hanging features and simplified the overall additive manufacturing process. In addition, the new method sped up the fabrication process and could improve the mechanical properties, owing to more uniform layers. The temperature at the interface exceeded the melting point of the polymeric matrix and was adequate to interfuse the polymer chains for full consolidation. We used polyamide 6 (PA6) as a high performance thermoplastic matrix for an alternative to conventional and single-use thermoset polymers with complex curing cycles. Thermoplastics have shown a great potential to improve the printing flexibility of CFRPs [22] and allow an improved control over reproducible physical properties [23]. Continuous carbon fiber reinforced thermoplastic (CFRTP) composites are a class of structural materials offering superior strength, impact resistance, lightweight, extensive shelf life, recyclability, and exceptional damage tolerance.[1, 24] A CO₂ laser source with 29 W power was used for bonding the CFRTP layers due to high absorptivity of both polymeric matrix and carbon fibers for 10.6 μm wavelength of laser radiation.[25] The high temperature, induced by laser beam, significantly improved the interfacial bonding over extrusion based techniques, such as FDM. In addition, the pressure delivered by the consolidation roller eliminated the voids between layers. These advantages coupled with aligned CCF reinforcement enabled us to produce ultra-strong 3D printed constructs. In this work, we demonstrated the highest tensile and flexural strength of 668.3 and 591.6 MPa, respectively. Our technique was also capable of achieving high lap shear strength (17.01 ± 0.54 MPa) in the range of high performance CFRPs with epoxy resins produced by autoclave [26-28], as shown in Figure 4-2. The fracture surface of the lap shear test samples (Figure 4-3) showed adhesive failure and fiber pullout. This indicates an enormous improvement in interfacial bonding quality over other additive manufacturing techniques. The PA6/CCF prepreg sheets were used to demonstrate this 3D printing technique. Our 3D printing was also capable of producing 3D multi-

material structures by using various prepreg composites materials. Herein, we demonstrated this ability by printing subsequent layers of glass and carbon fiber reinforced prepreg. Optical image of some 3D printed carbon fiber composite structures is shown in Figure 4-1 (d). The thickness of the prepreg sheets, which determined the vertical resolution of the process, was 130 μm . The CCF orientation in the 3D printed laminated structures can be controlled and designed according to the application and loading direction. Differential scanning calorimetry (DSC) of these materials is presented in Figure 4-1 (e), showing the crystallization behavior and melting point of PA6/CF and polypropylene (PP)/GF. Our 3D printing process also has the potential to be developed as an automated process for manufacturing high performance laminates [29, 30] with comparable mechanical properties to the conventional autoclave method [31].

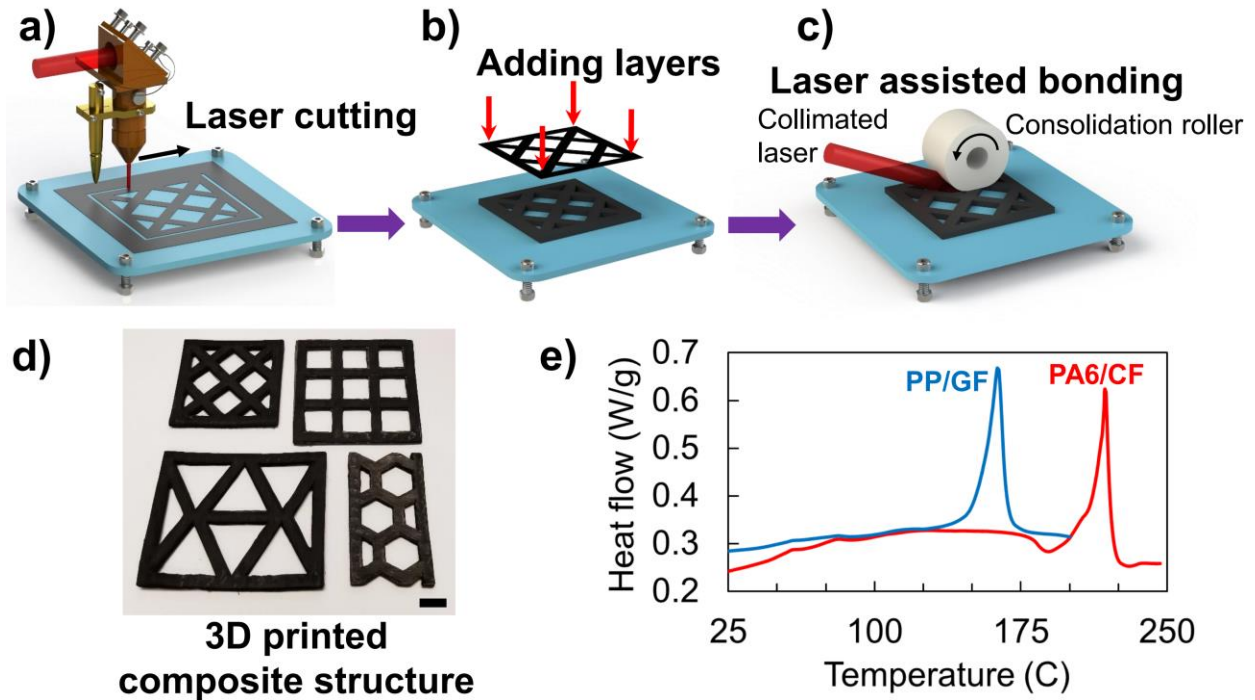


Figure 4-1 Schematic illustration of the laser assisted 3D printing for carbon fiber reinforced thermoplastic composites. a) Laser cutting of prepreg composite sheet using a focused CO₂ laser beam based on the sliced shape. b) Adding the pre-cut layer on top of the previous printed layers. c) Laser assisted bonding of composite prepreg sheets using a tilted CO₂ laser beam and a consolidation roller. High temperature above the resin melting point from the laser irradiation and pressure from the consolidation roller causes full consolidation of the prepreg layers. d) Optical picture of final 3D laminated structures produced by 3D printing (scale bar: 10 mm). e) DSC curves of polyamide 6 PA6/CF and polypropylene /GF prepreg composite sheets used in our 3D printing method.

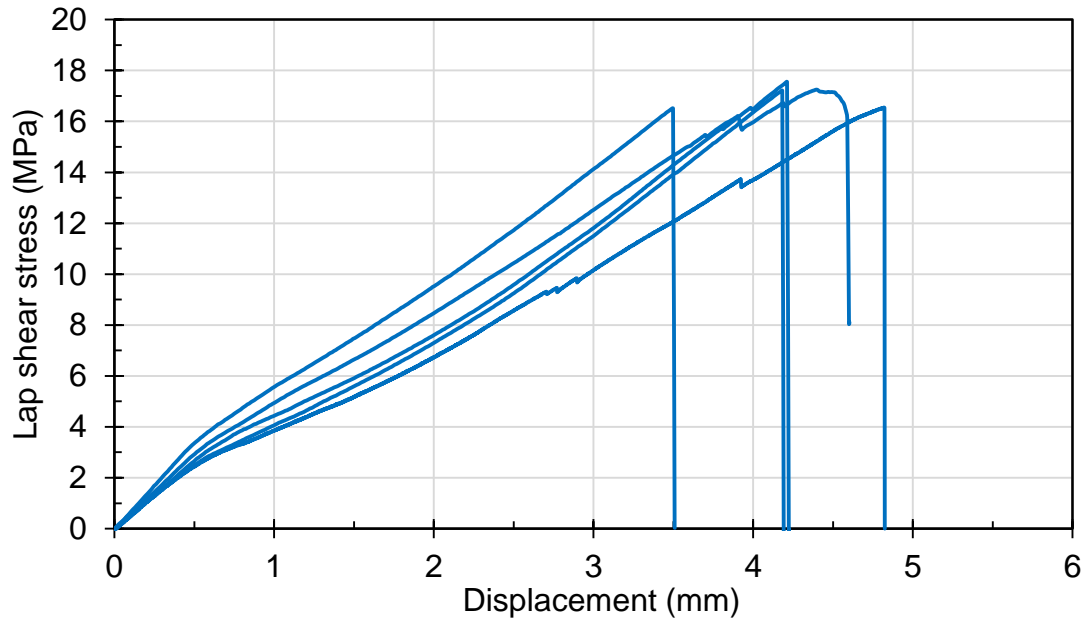


Figure 4-2 Lap shear strength for the test laser bonded unidirectional carbon fiber laminates. 5 samples with similar condition were tested.

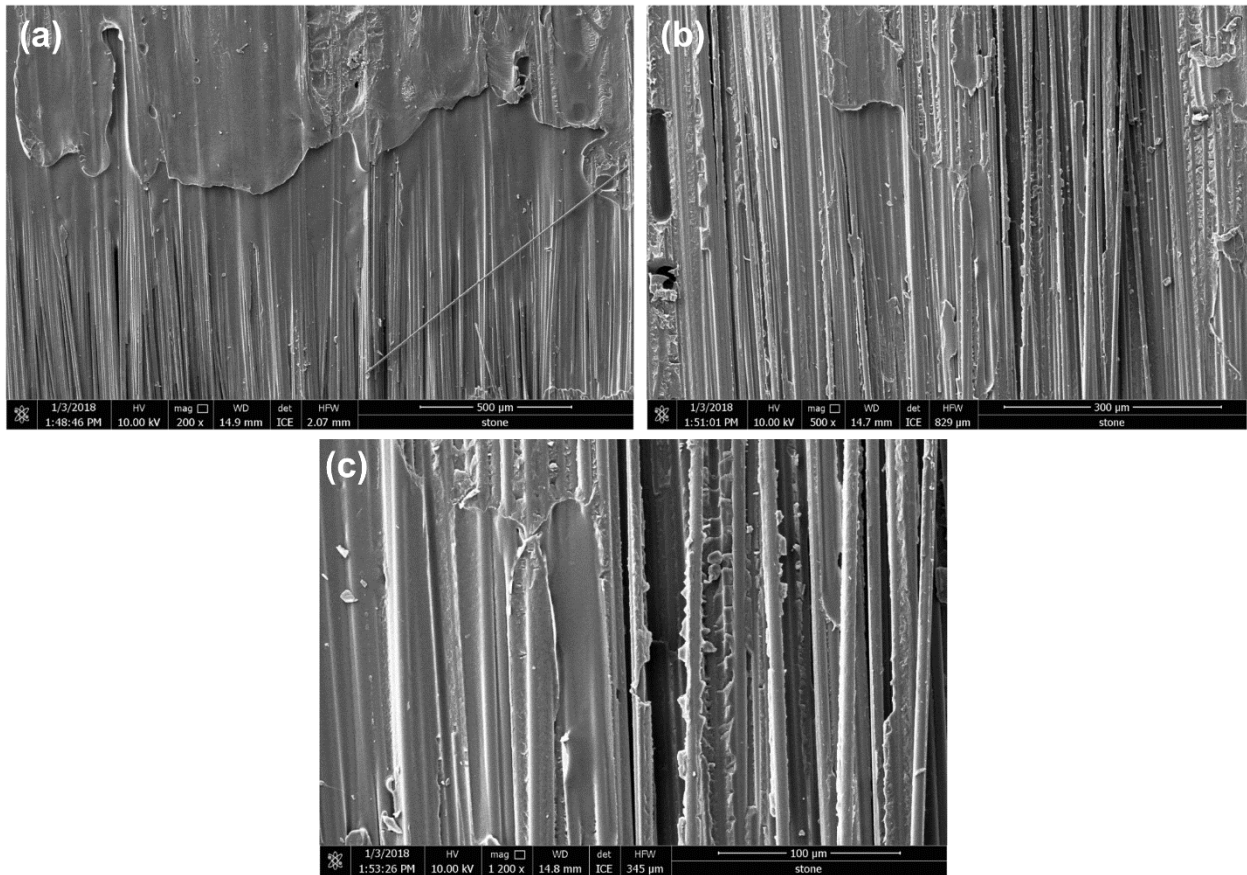


Figure 4-3 Fracture surface of the lap shear test samples

Experimental

Materials

The CFRTP prepreg used in this work was Celstran CFR-TP PA6 CF60-03 with 60 wt. % (48.5 vol. %) carbon fiber and 130 μm layer thickness (Celanese Corp, Dallas, TX). The glass fiber prepreg composite was IE 6832 with 66.5 wt. % glass fiber and 300 μm thickness supplied by Polystrand (Englewood, CO).

Laser Assisted 3D printing

The 3D CAD geometry was sliced into 2D profiles and then cut by a CO₂ laser cutter (Full Spectrum P-Series, Las Vegas, NV) with maximum power of 90 W. The laser beam was focused to 1 mm in diameter. The 37% and 60% of laser power were used to cut CF and GF prepreg sheets, respectively, with the cutting speed of 50 mm/s. The prepregs composite sheets were then bonded in a layer by layer fashion using a consolidation roller and a top-scanning CO₂ laser beam at 20° angle from the build plate. The laser beam heated the prepreg sheets to above its melting point and with the pressure provided by the stainless steel roller (41.25 mm diameter) the composite sheets were bonded and fully consolidated. The laser beam was Gaussian beam and 6 mm in diameter. The 100 W CO₂ laser used for bonding was purchased from Beijing Reci Laser Technology, China. The laser beam was directed to the nip point under the consolidation roller heating the printing layer from the top. The built plate moved at 6 mm/s in a serpentine pattern to cover the entire surface area with 3 mm spacing between scanning lines.

Characterization

Differential scanning calorimetry (DSC) of PA6/CF and PP/GF was performed using TA instrument DSC Q200 and in the temperature range of -10°C to 250°C. 5.7 mg of each material was sampled for DSC and data was sampled at the time intervals of 0.2 s. Scanning electron

microscopy (SEM) (FEI Versa 3D Dual Beam, OR) micrographs were observed at an acceleration voltage of 10 kV and an emission current of 20 μ A. Micro CT scans were performed with Xradia microXCT 400 Scanner with the resolution of 1 μ m at the University of Texas at Austin CT Laboratory (UTCT). The tensile testing was conducted based on ASTM D3039 standard with Shimadzu AG-IC universal testing machine (Kyoto, Japan) at a constant 1 mm/min strain rate (Figure 4-4). The 3-point bending test was based on ASTM D7264 standard and performed with Shimadzu EZ-LX universal testing machine (Kyoto, Japan) at 1 mm/min strain rate (Figure 4-5). For both tensile and 3-point bending tests, at least 5 samples were tested and averaged for each condition to determine the properties. The lap shear test was conducted based on ASTM D5868 standard with Shimadzu AG-IC universal testing machine (Kyoto, Japan) at the rate of 13 mm/min and repeated 5 times. We performed lap shear adhesion tests for fiber reinforced plastic bonding based on ASTM D5868 standard. At least 5 samples were tested to determine the lap shear strength of the laser bonded PA6/CF laminates. The dimensions of these specimens are explained in Figure 4-6. The tests were only performed for unidirectional laminates. Optical images of the lap shear test samples are shown in Figure 4-7.



Figure 4-4 Some of the tensile bars used for tensile testing (scale bar: 14 mm).



Figure 4-5 Some of the flex bars used for 3-point bending testing (scale bar: 10 mm)

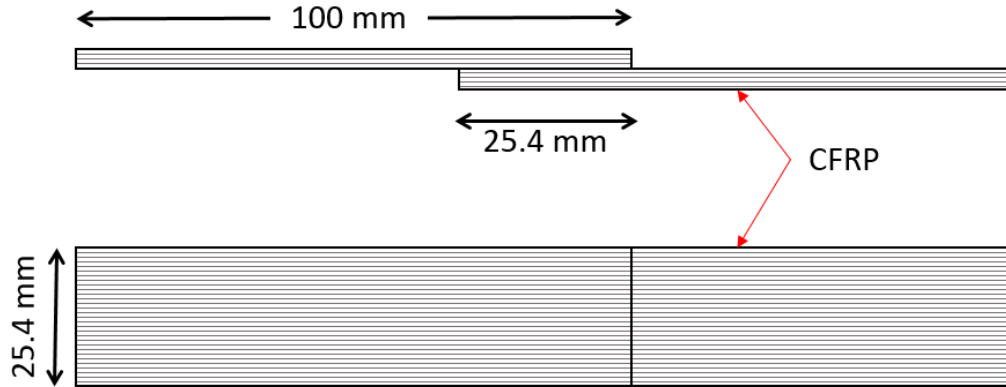


Figure 4-6 Overall layout and dimensions of the ASTM D5868 lap shear test specimens



Figure 4-7 Optical image of lap shear test samples (Scale bar: 25 mm)

Microstructure

We studied the microstructure of the 3D printed CFRTPs through micro computed tomography (micro-CT) scans (Figure 4-8) with ultrahigh resolution of 1 μm . For this communication, we printed structures with various fiber orientations in each layer, specifically, unidirectional $[0^\circ]_s$ (Figure 4-8 (a)), cross-ply $[0/90^\circ]_s$ (Figure 4-8 (b)), and $[0/-45/0/45^\circ]_s$ (Figure 4-8 (c)), as well as unidirectional glass-carbon fiber (G-CF) reinforced composites (Figure 4-8 (d)). The 3D illustrations of continuous fiber reinforcement in these structures were created using the micro-CT scan slices and presented in Figure 4-8. The continuous glass and carbon fibers are

easily distinguishable with 0° , $\pm 45^\circ$, and 90° angle orientations in these 3D images. The inset in Figure 4-8 (a) shows the cross section of the 3D printed unidirectional laminate, containing fibers in 0° orientation. All fibers in these samples aligned in one direction and provided the highest longitudinal reinforcement. The cross sectional scans of the cross-ply samples are presented in Figure 4-8 (b) inset. CCFs had two principal orientations of 0° and 90° , and potentially, these laminates should exhibit similar strength in these two directions. Figure 4-8 (c) inset shows the scan from the cross section of $[0/-45/0/45]_s$ sample with CFs oriented in 0° and $\pm 45^\circ$ angles. The CT scans of our 3D oriented CFRTPs showed decent interfacial bonds and no indistinctive boundary between printed layers except for some minor voids. Lastly, the scan of G-CF reinforced samples is shown in Figure 4-8 (d) inset, demonstrating the GF and CF both are in 0° orientation. More void content was noticed in the multi-material sample and the boundaries between layers are more distinct. This was, most probably, due to the poor interfacial bonding between dissimilar thermoplastic resins used in the multi-material specimens. Additional 3D illustrations and CT scans of the 3D printed carbon fiber composite microstructure can be found in Appendix A. The demonstrated continuous reinforcement significantly improved the strength and stiffness over pure polymers and short fiber reinforcement with the potential of being implemented for end-use products across various industries.

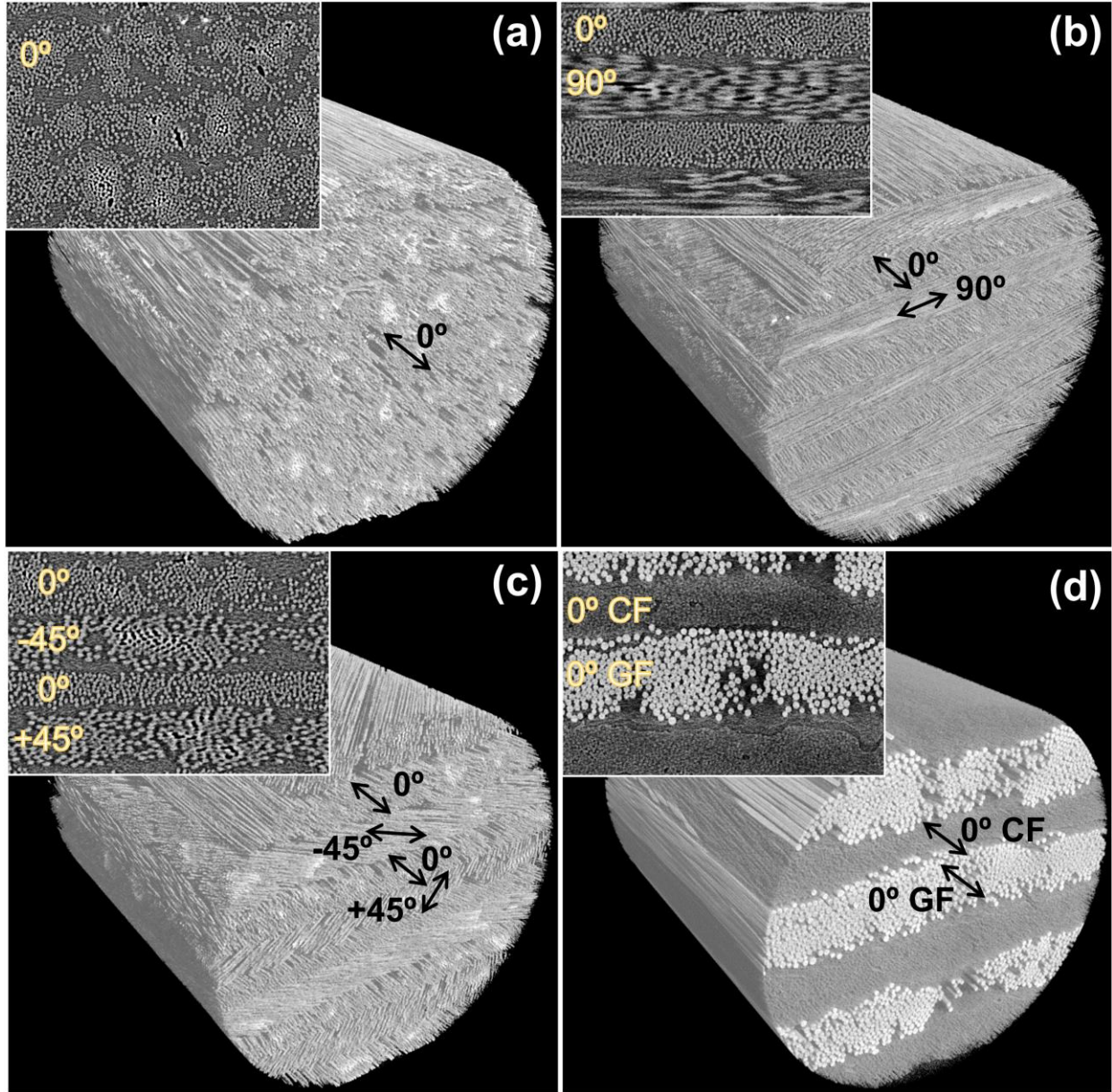


Figure 4-8 Micro CT scans of the 3D printed CFRTPs with various fiber orientations, namely, a) unidirectional [0]_s, b) cross-ply [0/90]_s, c) [0/-45/0/45]_s, and d) unidirectional with both GF and CF. The continuous carbon fiber reinforcement can be achieved in any desired angle at any given layer. The insets show the cross sectional slices of the CT scans and demonstrate the fiber orientation in 3D printed composite structure.

Mechanical Properties

We have conducted the mechanical properties tests to evaluate the strength and Young's modulus of our 3D printed CFRP structures. Tensile bars were fabricated with various fiber

alignments and materials to investigate the tensile properties relative to fiber reinforcement. Unlike other 3D printing techniques which can only print fiber composites with unidirectional or limited fiber alignments, our proposed 3D printing methodology could control the fiber alignment in each layer. Here, we printed unidirectional $[0^\circ]_s$, cross-ply $[0/90^\circ]_s$, and $[0/-45/0/45^\circ]_s$ CFRTPs, as well as unidirectional glass-carbon fiber (G-CF) reinforced composites. In general, the CFRP laminates exhibit intense anisotropic strength dependent on the state of carbon fiber orientation [32]. Typically, they have superior longitudinal strength and stiffness along fiber orientation over transverse direction and most of the CFRPs use multi-direction fiber reinforcement to achieve high strength in several directions. Figure 4-9 (a) shows the typical stress-strain curve of tensile testing. Our 3D printed unidirectional tensile bars exhibited high tensile strength and modulus of 668.3 ± 80.6 MPa and 18.2 ± 4.1 GPa, respectively, owing to the alignment and high weight ratio of CFs in the loading direction. Our 3D printed unidirectional CFRPs substantially overwhelmed FDM with CCF reinforcement and extrusion in terms of ultimate strength (Figure 4-9 (d)). There were two distinct regions observed in the tensile stress-strain curves and the slope of the curves slightly decreased after fiber-matrix debonding. This phenomenon was previously observed in continuous CFRTP FDM printing and our previous work [21, 33]. After the printing process, a portion of the carbon fiber bundles were not entirely straight and they could further be stretched under tensile loads, thus causing a slight drop in the curve's slope.

The tensile fracture surface of the unidirectional tensile bars (Figure 4-9 (b)) shows microscopic fiber pullout and breakage resulting from tensile test. The fracture surface appeared to be free of delamination with fiber breakage and fiber-matrix debonding being the primary fracture mechanism. The $[0/-45/0/45^\circ]_s$ and cross ply samples exhibited an impressive tensile strength of over 600 and 400 MPa, respectively. The fiber pullout could be observed in the fracture

surface of these samples (Figure 4-9 (c) and (e)) for the fibers aligned in 0° and $\pm 45^\circ$, in which fibers are completely snapped out of the matrix. These results demonstrated a higher tensile strength than aerospace grade Aluminum alloy 7075-T652 [34] with 470 MPa ultimate tensile strength. Our 3D printing methodology for CFRTP composites could be an excellent lightweight replacement for high strength Aluminum alloys. On the other hand, the tensile bars with G-CF reinforcement exhibited the lowest strength and modulus amongst the printed samples (239.4 ± 9.4 MPa and 9.6 ± 1 GPa, respectively) mainly due to the lower strength of GF reinforcement. The fracture surface of these samples (Figure 4-9 (f)) showed concurrent delamination and fiber breakage. This delamination was primarily due to the low interlaminar bonding strength between PP and PA6 resins. As a benchmark, the tensile strength and modulus of our printed CRFTP composites were compared with other previously reported additive manufacturing techniques capable of processing CFRTP (Figure 4-9 (d)). The tensile strength of our 3D printed unidirectional CFRPs significantly exceeded other available 3D printing methods with comparable tensile Young's modulus to extrusion and FDM. The tensile performance of our composite tensile bars was vastly superior to SLS, inkjet, and SLA both in terms of strength and modulus with the tensile strength of up to 3 times higher than majority of FDM and 10 times higher than SLS, inkjet, and SLA. The capability to process composites with high fractions of CCF (48.5 vol. %) and exceptional interfacial bonding were the distinct characteristics of our methods over other 3D printing techniques which was responsible for the ultrastrong 3D printed laminates. Moreover, these structures could offer reinforcement in several directions and be designed to support multi-directional loads.

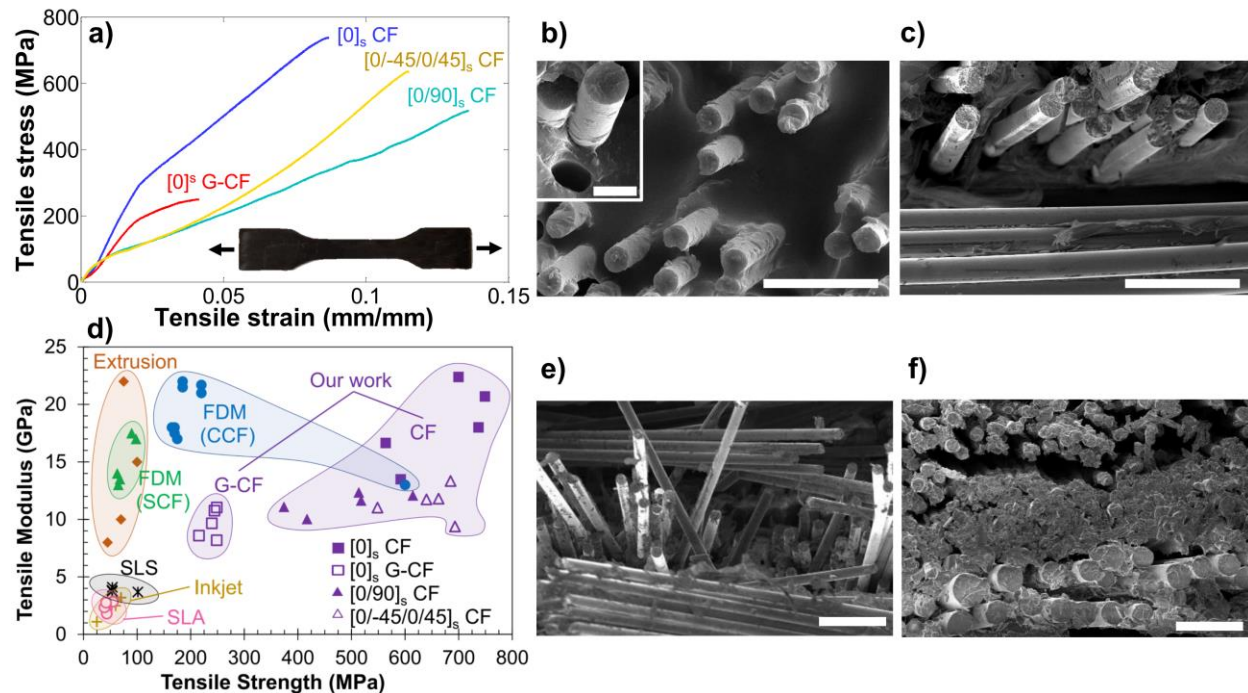


Figure 4-9 Tensile properties of the 3D printed carbon fiber composites. a) Representative tensile stress versus strain curves for 3D printed tensile bars of varying fiber materials and alignments. d) Property space map of tensile modulus versus tensile strength that compare our 3D printed CFRTP with other CF reinforced polymer 3D printing methods, namely, FDM [6-8, 16, 18], extrusion [12], SLS [12, 35], inkjet [12], and SLA [12, 36, 37]. Tensile fracture surface of the tensile bars with b) unidirectional $[0]_s$, c) cross-ply $[0/90]_s$, and e) $[0/-45/0/45]_s$ with CF reinforcement. f) Tensile fracture surface of a multi material tensile bar with unidirectional $[0]_s$ glass and carbon fiber reinforcement. The inset in (b) shows the fiber pullout resulted from the tensile test. Scale bars are 30 μm for (b), (c), (e), and (f). The scale bar for the inset in (b) is 5 μm .

We also investigated the flexural properties of our 3D printed composites to better understand the interlaminar bonding. Flex bars with four previously mentioned fiber alignments were 3D printed for the 3-point bending test and results are displayed in Figure 4-10 (a). Unsurprisingly, our unidirectional CFRTPs displayed the highest flexural strength and modulus of 591.16 ± 88.6 MPa and 79.0 ± 10.0 GPa, respectively. The $[0/-45/0/45]_s$ and cross-ply samples exhibited slightly lower flexural strength 460.6 ± 33.2 MPa and 352.5 ± 31.3 MPa, respectively, due to less CF in the bending direction. Flexural modulus of our $[0/45/0/45]_s$ and cross-ply printed CFRTPs was 49.2 ± 5.9 GPa and 46.3 ± 3.4 GPa, respectively. The unidirectional G-CF reinforced

structures exhibited lower flexural strength and modulus of 163.6 ± 47.1 MPa and 36.1 ± 9.9 GPa, respectively, due to the usage of less strong GF. The SEM images (Figure 4-11) shows the fracture mechanisms in the flex bars. In the 3D printed single material CF composites the failure was mainly due to fiber and matrix failure, however, delamination in dual-material samples (G-CF reinforced) was more prominent due to the lower quality of interfacial bonding. As a reference, we plotted the flexural property map of our printed composite structures in comparison with other 3D printed carbon fiber composites (Figure 4-10 (b)). Our 3D printed composites showed impressive flexural properties, which are significantly higher than the best 3D printed CFRTP materials, with around 100% improvement in both flexural strength and modulus. Our unidirectional CFRTPs were 50% stronger and 100% stiffer than the strongest FDM with CCF reinforcement and up to 6 times stronger than SLS and FDM with SCF. The exceptional flexural strength and modulus make our printed architectures a prime candidates for structural material in various industries where rigidity and stiffness are essential.

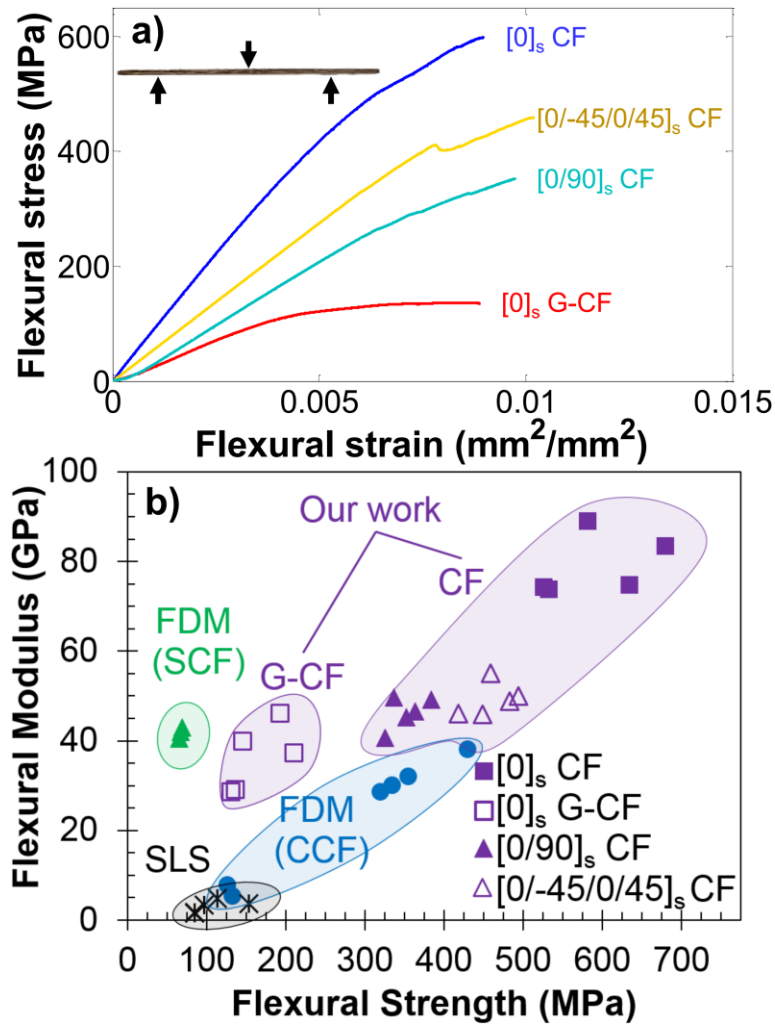


Figure 4-10 Flexural properties of the 3D printed CFRTP flex bars. a) Typical flexural stress versus strain curves from 3-point bending test of flex bars with varying fiber alignments. b) Property space map of flexural modulus versus flexural strength in comparison with CFRTPs fabricated by FDM [16, 17] and SLS [14, 35].

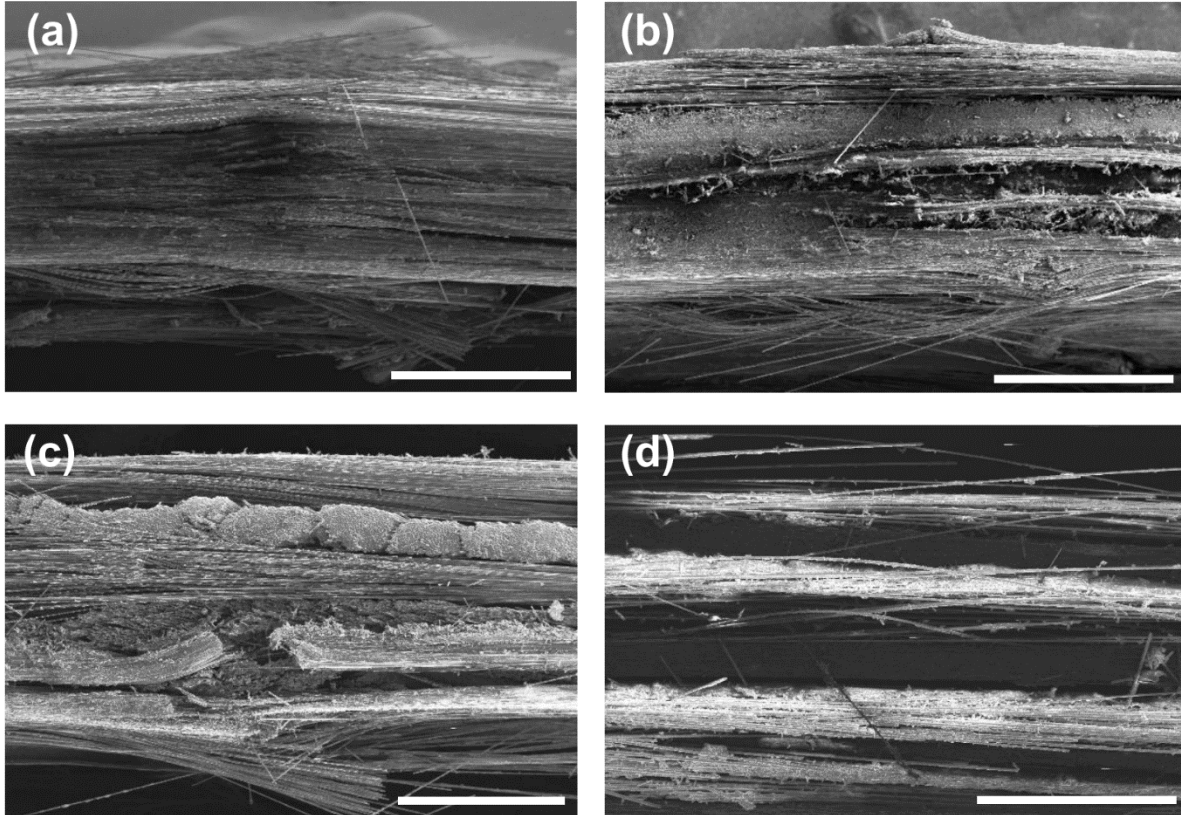


Figure 4-11 SEM images from sides of the flex bars after 3-point bending test for (a) unidirectional, (b) cross-ply, (c) [0/-45/0/45]_s, and (d) unidirectional G-CF laminates (Scale bar: 1 mm).

Finite Element Simulation

In order to evaluate the bonding process, we conducted a heat transfer finite-element (FE) simulation of the laser bonding process using COMSOL Multiphysics (Figure 4-15 (a)). The geometry of the simulated domain was same as the geometry used in temperature measurement with thermocouples. The built-in heat transfer modulus of COMSOL was used for the heat transfer simulation. The geometry of the domain (Figure 4-12) was consist of 8 layers of prepreg sheets with the dimensions of 25x120 mm. The roller was also included in the simulation. Heat transfer conduction in solid with a translational motion (equation 4-1) was used to perform the heat transfer in the laminate.

$$\rho C_p u \cdot \nabla T + \nabla \cdot q = 0 \quad \ni \quad q = -k \nabla T \quad (4-1)$$

where ρ is the volumetric mass, C_p is the heat capacity, k is the anisotropic conductivity tensor, v is the bonding velocity, and T is the temperature. Our boundary conditions consisted of convective heat flux (equation 4-2) on all outer surfaces, thermal contact at the 3 upper interfaces (equations 4-3 – 4-6), and the boundary heat source on top of the laminates and on the roller.

$$q_0 = h \cdot (T_{ext} - T) \quad (4-2)$$

$$-n_d \cdot q_d = -h(T_u - T_d) + rQ_b \quad (4-3)$$

$$-n_u \cdot q_u = -h(T_d - T_u) + (1 - r)Q_b \quad (4-4)$$

$$r = \frac{1}{1 + \xi}, \quad \xi = \sqrt{\frac{\rho_u C_{p,u} (k_u n_u) \cdot n_u}{\rho_u C_{p,d} (k_d n_d) \cdot n_d}} \quad (4-5)$$

$$h = h_c + h_g \quad (4-6)$$

where h_c is the constriction conductance and is obtained by cooper-mikic-yovanovich correlation [38] and h_g is parallel plate gap gas conductance [39]. The cooper-mikic-yovanovich correlation is built in COMSOL. The boundary heat source represent the laser source on top of the laminate. In our simulation, we modeled the laser source as an elliptical beam to accommodate the tilting angle of the laser beam. An elliptical Gaussian model was used as a boundary heat source to simulate the 20° angle of the laser beam (equation 4-7) [40]. This elliptical Gaussian heat source is presented in Figure 4-13.

$$P(x, y) = P_0 \exp \left\{ - \left[\frac{((x - x_c) + (y - y_c))^2}{2\sigma_a^2} + \frac{(-(x - x_c) + (y - y_c))^2}{2\sigma_b^2} \right] \right\} \quad (4-7)$$

where σ_a and σ_b are the standard deviations of the Gaussian profiles along the elliptical major axis and minor axis, (x_c, y_c) is coordinate pair of the peak value location, and P_0 is the laser peak power per area. The prepreg composite sheets exhibit orthotropic properties. The thermal properties of

PA6/CF at room temperature was supplied by Celanese Corporation. We used the general rule of mixture for thermal conductivity to estimate the axial and transverse temperature dependent thermal conductivity (Figure 4-14) [41]. The temperature dependent thermal conductivity of PA6 and carbon fibers were obtained from elsewhere [42, 43]. The roller material is stainless steel. The rest of the material properties and COMSOL parameters are shown in Table 4-1.

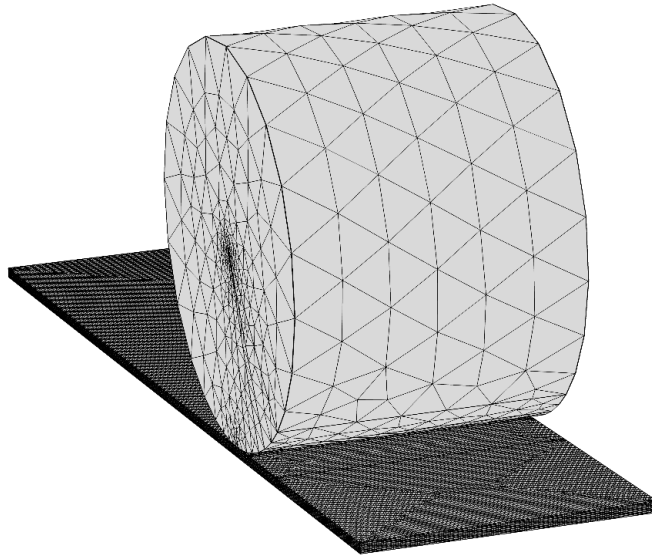


Figure 4-12 Meshed geometry used in COMSOL simulation

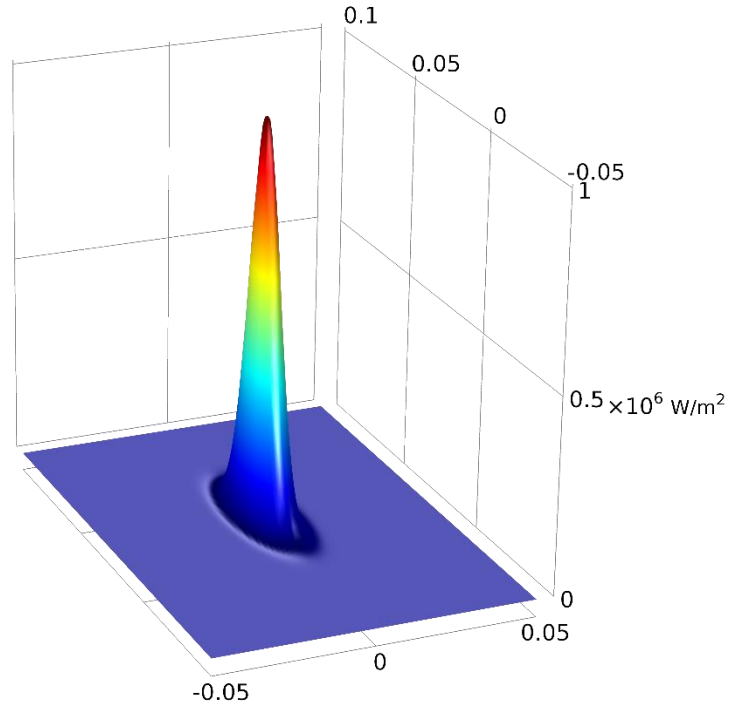


Figure 4-13 Elliptical Gaussian boundary heat source

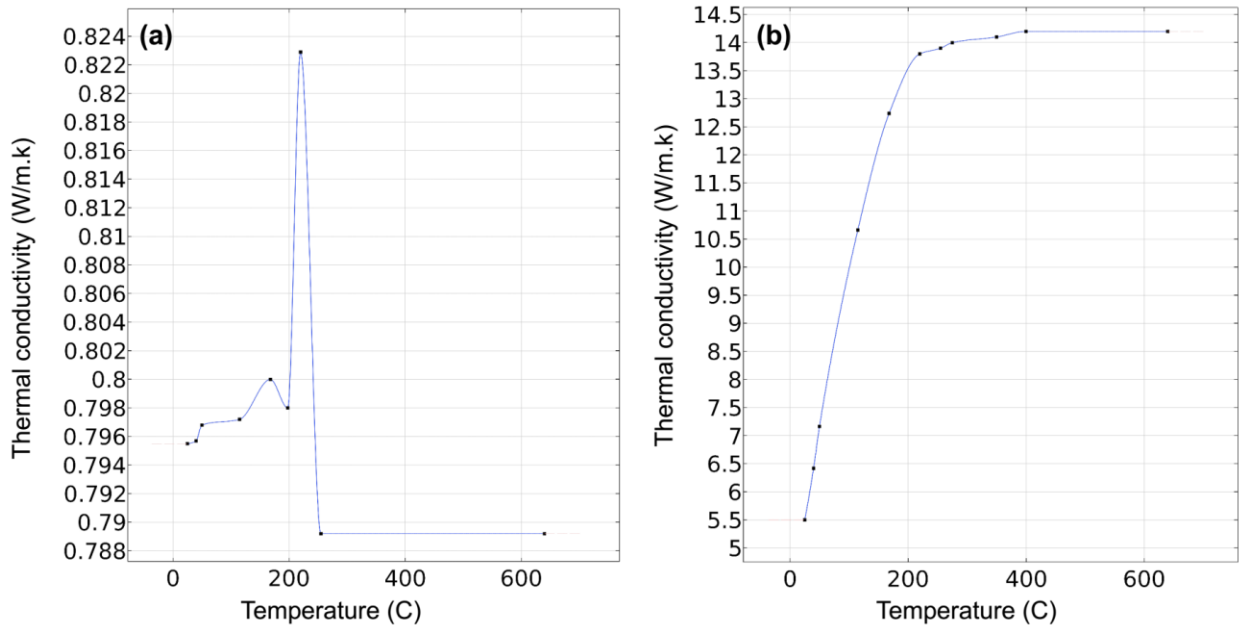


Figure 4-14 (a) Transverse and (b) longitudinal temperature dependent thermal conductivity of PA6/CF

Table 4-1 Material properties and COMSOL parameters used in the heat transfer simulations

Material properties and COMSOL parameters	Value
Heat capacity of PA6/CF	1700 J/kg.K
Density of PA6/CF	1450 kg/m ³
Thermal conductivity of the roller	15 W//m.K
Heat capacity of roller	460.55 J/kg.K
Density of Roller	8000 kg/m ³
Convective coefficient	23 W//m ² .K
Laser Power (P ₀)	29 W
Translational speed	6 mm/s
σ_a	2.5 mm
σ_b	7.3 mm
PA6/CF absorption	0.125
Roller absorption	0.1
Ambient and initial temperature	298.15 K
Surface roughness of PA6/CF	2 μ m
Thermal conductivity of air	0.025 W//m.K

The simulated temperature distribution was validated by thermal sensors embedded in the interface (Figure 4-15 (a) inset). The temperature distribution in the interface played a crucial role in the consolidation of two prepreg layers with polymer diffusion. These executed FE simulations and experimental studies on the heat transfer during the bonding process can directly inform the laser bonding parameters. The temperature distribution at the bonding interface is of high importance for consolidation to occur. From the FE simulations, the maximum temperature at the first interface, which is the most important, was well above the PA6 melting point (220 °C) at 360 °C. The maximum temperature at the second and third interface was simulated to be 257 °C and 158 °C, respectively. In order to accurately validate our heat transfer simulations, we embedded three micro thermal sensors (d=70 μ m) at the three upper interfaces for internal temperature measurement, as illustrated in Figure 5c. The thermocouples reading and simulation data for the temperature history agree with each other (Figure 4-15 (b)). The 3D printed structure with CCF

reinforcement possessed orthotropic properties in each lamina and overall were anisotropic. 8 layers of prepreg sheets were used in both experimental temperature measurements and FE simulation. For the temperature measurement experiments, we embedded the thermal sensors at the three upper interfaces and bonded the last three layers at the same time while recording the temperature at 40 ms intervals. We also considered one reflection of laser beam from both roller and composite sheet. With the validated FE model, we could improve our fundamental understanding about this process and it guided us to alter process parameters for further optimization.

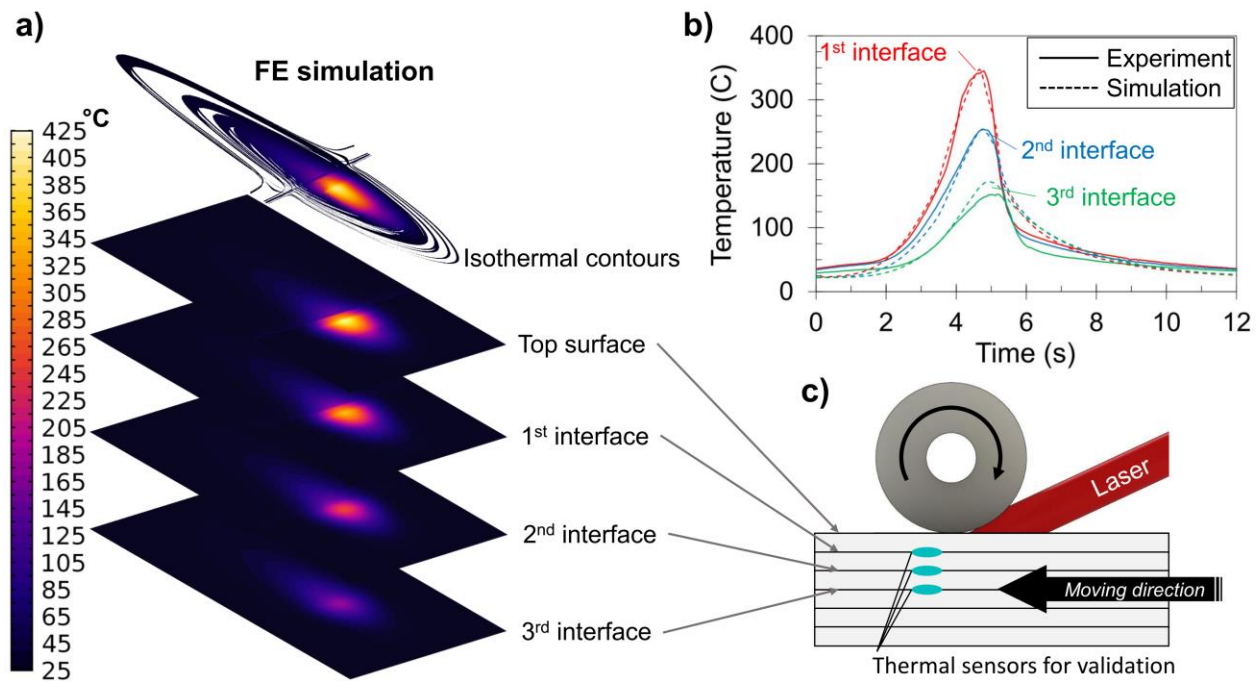


Figure 4-15 Heat transfer analysis of the CFRP laser assisted bonding process using FE simulations. a) Temperature distribution in the CFRP laminate during the laser bonding process computed from the FE simulation. Isothermal contours show the temperature profile in the entire geometry; the temperature distribution on the top surface, 1st, 2nd, and 3rd interface are presented due to their importance in the consolidation process. The temperature at the 1st interface is well above the PA6's melting point (220 °C). The image from thermal IR camera shows the experimental temperature distribution on the top surface. b) Comparison of the temperature history obtained by thermocouples during the experiment with FE simulation at 1st, 2nd, and 3rd interface. c) Schematics of the thermal sensor locations for the experimental temperature measurements.

In order to further understand the effects of processing parameters on the temperature distribution, we performed additional simulation and experiments for laser powers (P) of 25 and 29 W with the scanning speeds (v) of 6, 12, and 18 mm/s. The temperature distribution at the cross section for all 6 printing conditions are presented in Figure 4-16. It can be observed that with increasing the laser power and decreasing the scanning speed, higher temperatures could be obtained at the cross section. The melting point of Nylon6 resin is 220 °C and temperatures above melting point were easily accessible with the current setup. Temperatures above melting point at the interface facilitate material diffusion and result in a stronger interlayer bonding. The assumption of thermal contact boundary condition at the upper interface (interface 1) caused the temperature at the top layer to be relatively high due to the increased thermal resistance at interface 1. In order to validate our simulation results, we performed experiments with the same parameters as FE simulations. The temperature history of three upper interfaces (interface 1-3) for some of these parameters is shown in Figure 4-17. The dimensions of the laminate for these experiments were same as the geometry used in FE simulations (120x25 mm).

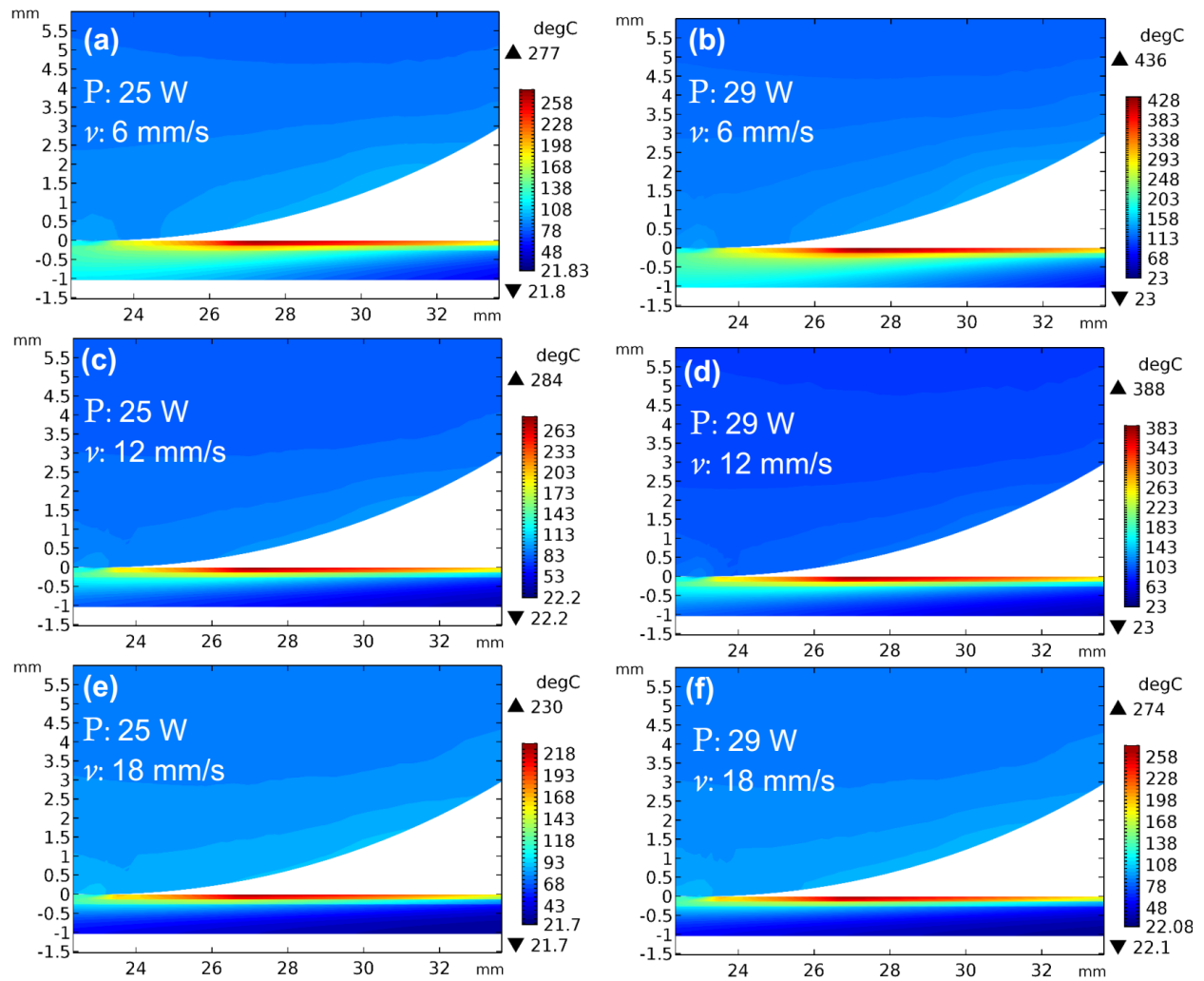


Figure 4-16 The temperature profile obtained from FE simulations at the cross section for various process parameters, namely, (a) P=25 W, v =6 mm/s, (b) P=29 W, v =6 mm/s, (c) P=25 W, v =12 mm/s, (d) P=29 W, v =12 mm/s, (e) P=25 W, v =18 mm/s, and (f) P=29 W, v =18 mm/s.

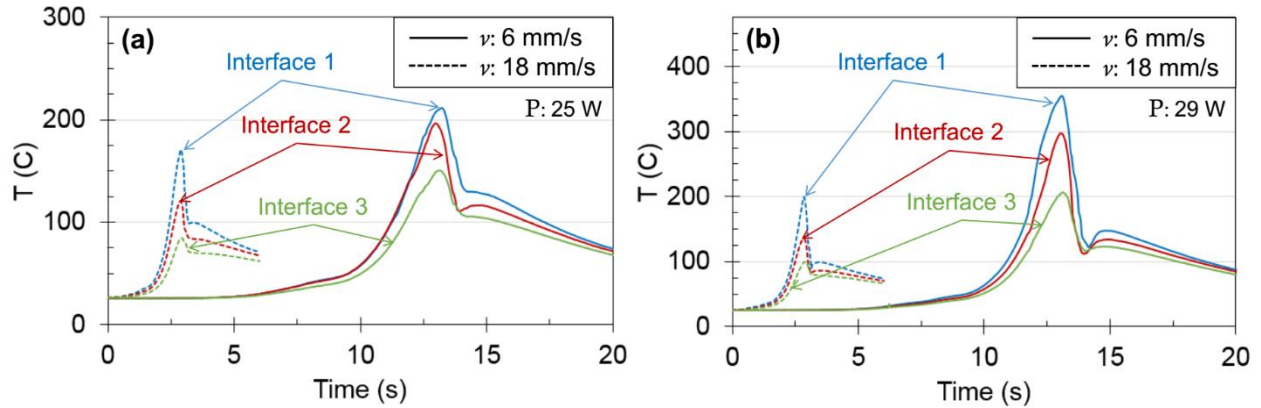


Figure 4-17 The experimental temperature history obtained from thermocouples, at interface 1-3, for the laser powers of (a) 25 W and (b) 29 W.

We compared the simulated maximum temperature at three upper interfaces with the experimentally measured values to validate our FE model. This comparison is illustrated in Figure 4-18 for all 6 parameters. The FE model had a decent agreement with experimental results and could successfully predict the temperature distribution in the laminate during the 3D printing process. Our model can be used to optimize the bonding process during the bonding process to achieve the desired temperature for a required time at the interface. The temperature should be above melting point to enable the diffusion of thermoplastic resin in the prepreg composite sheets. The developed FE model is a versatile method to study the effect of process conditions on the interfacial bonding quality.

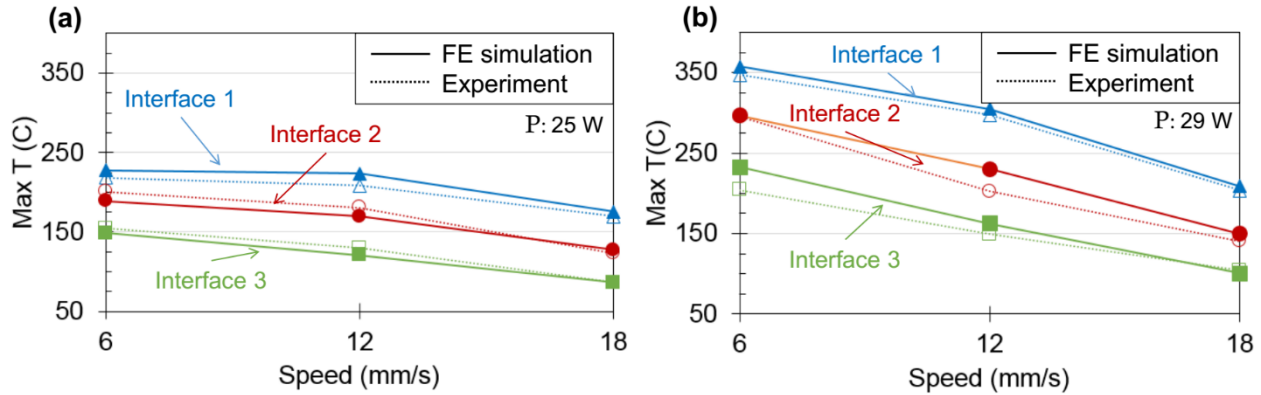


Figure 4-18 The comparison of maximum temperature at interface 1-3 between the FE simulations and experimental results for the laser powers of (a) 25 W and (b) 29 W.

Practical Applications

The feasibility of our 3D printing technique for high-strength CFRTP constructs was further established through 3D printing a laminate structure capable of supporting the axial (Figure 4-19 (a)) and transverse (Figure 4-19 (b)) load of P. Parandoush's weight, as well as, a fully functioning remote control car (Figure 6c and 6d). All of these structures were 3D printed with $[0/-45/0/45]_s$ CF orientation for a high multi-directional strength. Figure 4-19 (a) shows the incredible axial strength of the 3D printed support structure. The dimensions of this 3D printed structure were 150x100x12 mm and its detailed drawing is illustrated in Figure 4-19 (b). Nevertheless, one of the main benefits of our method was the strong interlayer bonding and it was verified in Figure 4-19 (b) by supporting a transverse load of P. Parandoush weight. These results are not surprising as we previously confirmed the ultrahigh tensile and flexural strength of these additively manufactured CFRTPs. Furthermore, our 3D printed frame for a remote control car proven to be as stiff and strong as the original Aluminum frame that it replaced. The supreme flexibility of our additive manufacturing technique, paired with its high strength-to-weight ratio

can be a defining moment for 3D printing to become a chief candidate in the production of high performance structural materials.

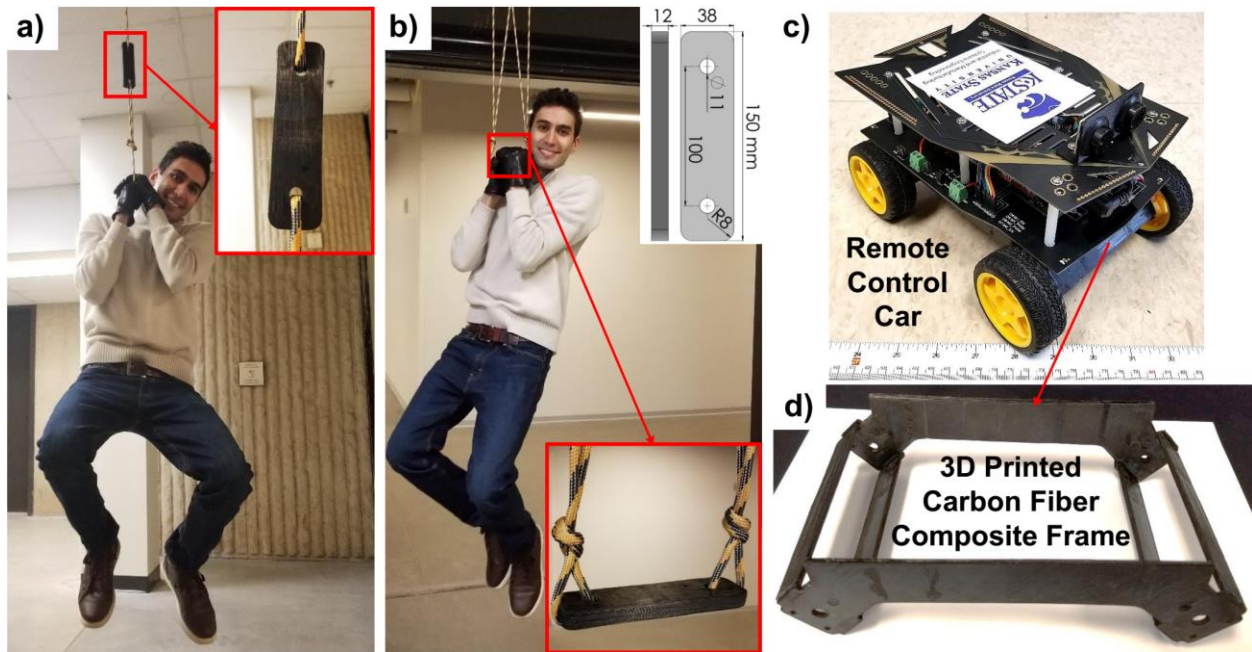


Figure 4-19 Some practical implications of the developed additive manufacturing technique. The 3D printed CFRTTP structure with $[0/-45/0/45]_s$ fiber orientation can support the weight of P. Parandoush in both a) axial and b) transverse direction. This strength is enabled by having a variety of continuous fiber reinforcement directions and exceptional interfacial bonding. c) This 3D printing methods method was also used to print the chassis of a remote control car. d) The printed under body of the car was replaced the original Aluminum parts without sacrificing the rigidity of the structure.

The 3D printing technique described in the current work, in addition to exceptional mechanical properties, is easily scalable for high volume productions. This system is based on LOM and can be designed for components with the size scales from few centimeters to few meters. The LOM is capable of automation in handling materials, as well as automation of the entire additive manufacturing process. The modified bonding process does not add a significant complication to the design and conveniently remove the need of post processing for most of the engineering thermoplastics. The only challenge in designing this system would be determining the prepreg thickness after the laser consolidation process and adjusting the vertical travel based on

the prepreg material and process parameters. Currently, autoclave molding and laser assisted tape placement (LATP) are the prominent manufacturing techniques used in CFRP production. Autoclave is a manual process that require expensive molds and post machining process is required to get the final geometry. LATP does not require molds, however, post processing is often required and complex geometries are not attainable [44, 45]. These factors enormously increase the production costs and hinder the wide spread utilization of CFRP in consumer products. The 3D printing technology suggested in this work could streamline the CFRP production and replace existing manufacturing methods for various mass produced components. Additionally, the proposed technology is an improvement from production time standpoint over existing methods. With the help of automation and eliminating the need of molds and post-processing, the production time could be significantly reduced for potential commercial applications in aerospace, transportation, marine, etc. Finally, the additive manufacturing nature of the proposed approach means complex geometries, both internal and external, could be produced that conventional approaches are incapable of producing and yields new degrees of freedom in CFRP production.

Conclusions

In conclusion, we have demonstrated a high-strength 3D printed by utilizing prepreg composite sheets with CCF reinforcement as the feedstock. In this method, the CAD geometry was sliced to 2D cross section similar to other 3D printing techniques. In printing each layer, the prepreg sheets were laser cut based on the specified CAD model cross section. The prepreg layer was then bonded to the previous layer using a laser beam and a consolidation roller. This layer upon layer process was repeated until the final 3D geometry was achieved. Our 3D printed architectures incorporated high weight ratio CCFs and a strong interlayer adhesion responsible for

superior strength and stiffness over commercial composite 3D printing techniques. The tensile and flexural properties of our 3D printed CF/PA6 composites were superior to FDM, SLA, SLS, inkjet, and extrusion with both continuous and short carbon fiber reinforcement with tensile and flexural strength of 668.3 and 591.6 MPa, respectively. The controllable fiber alignment in any respective layer could further increase the flexibility of the 3D printed CFRTPs and add an entirely new dimension to the engineering design of 3D printed assemblies. By automation of this process, highly customized CFRTP geometries with complex internal and external features could be digitally designed, optimized, and manufactured, offering a substantial improvement in cost and flexibility relative to the manual and expensive conventional molding in the autoclave. This technique can be used for a wide variety of prepreg composites with thermoplastic resins and we demonstrated the capability of widening the range of materials available for additive manufacturing in this work. It also has a potential to be used with thermosetting resins which is one of our future scopes for this project. In addition, we developed a validated FE model capable of predicting temperature distribution in the CFRTP structure during the laser bonding process. Temperature disturbing at the laminate interface is the primary factor in the bonding quality and the FE model could help modifying and optimizing this technique for various structural composites. Moreover, this system can be designed for components with the size scale from few millimeters to few meters for potential commercial productions. With no required post-processing and the benefit of automation, this process is also scalable for high volume productions and could improve current CFRP productions both volumetrically and from a production time standpoint. The flexibility of the demonstrated 3D printing process and the ability to produce lightweight and strong structures made it favorable in various industries such as aerospace, automotive, marine,

and civil engineering where automation of the process could significantly bring down the cost and waste.

References

- [1] C. Soutis, "Carbon fiber reinforced plastics in aircraft construction," *Materials Science and Engineering: A*, vol. 412, no. 1, pp. 171-176, 2005/12/05/ 2005, doi: <http://dx.doi.org/10.1016/j.msea.2005.08.064>.
- [2] A. Maier, R. Schmidt, B. Oswald-Tranta, and R. Schledjewski, "Non-destructive thermography analysis of impact damage on large-scale CFRP automotive parts," *Materials*, vol. 7, no. 1, pp. 413-429, 2014.
- [3] Y. Miyano, M. Nakada, J. Ichimura, and E. Hayakawa, "Accelerated testing for long-term strength of innovative CFRP laminates for marine use," *Composites Part B: Engineering*, vol. 39, no. 1, pp. 5-12, 2008.
- [4] N. F. Grace, F. C. Navarre, R. B. Nacey, W. Bonus, and L. Collavino, "Design-construction of bridge street bridge-first CFRP bridge in the United States," *PCI J.*, vol. 47, no. 5, 2002.
- [5] P. Parandoush and D. Lin, "A review on additive manufacturing of polymer-fiber composites," *Compos. Struct.*, vol. 182, no. Supplement C, pp. 36-53, 2017/12/15/ 2017, doi: <https://doi.org/10.1016/j.compstruct.2017.08.088>.
- [6] C. Yang, X. Tian, T. Liu, Y. Cao, and D. Li, "3D printing for continuous fiber reinforced thermoplastic composites: mechanism and performance," *Rapid Prototyping Journal*, vol. 23, no. 1, pp. 209-215, 2017, doi: doi:10.1108/RPJ-08-2015-0098.
- [7] H. L. Tekinalp *et al.*, "Highly oriented carbon fiber-polymer composites via additive manufacturing," *Composites Sci. Technol.*, vol. 105, pp. 144-150, 2014.
- [8] F. Ning, W. Cong, J. Qiu, J. Wei, and S. Wang, "Additive manufacturing of carbon fiber reinforced thermoplastic composites using fused deposition modeling," *Composites Part B: Engineering*, vol. 80, pp. 369-378, 2015/10/01/ 2015, doi: <http://dx.doi.org/10.1016/j.compositesb.2015.06.013>.
- [9] M. L. Shofner, K. Lozano, F. J. Rodríguez-Macías, and E. V. Barrera, "Nanofiber-reinforced polymers prepared by fused deposition modeling," *J. Appl. Polym. Sci.*, vol. 89, no. 11, pp. 3081-3090, 2003, doi: 10.1002/app.12496.
- [10] H. S. J. and W. R. B., "Functionalizing stereolithography resins: effects of dispersed multi-walled carbon nanotubes on physical properties," *Rapid Prototyping Journal*, vol. 12, no. 5, pp. 292-303, 2006, doi: doi:10.1108/13552540610707059.

- [11] A. Gupta and A. A. Ogale, "Dual curing of carbon fiber reinforced photoresins for rapid prototyping," *Polym. Compos.*, vol. 23, no. 6, pp. 1162-1170, 2002, doi: 10.1002/pc.10509.
- [12] B. G. Compton and J. A. Lewis, "3D-Printing of Lightweight Cellular Composites," *Advanced Materials*, vol. 26, no. 34, pp. 5930-5935, 2014, doi: 10.1002/adma.201401804.
- [13] R. D. Goodridge *et al.*, "Processing of a Polyamide-12/carbon nanofibre composite by laser sintering," *Polym. Test.*, vol. 30, no. 1, pp. 94-100, 2011/02/01/ 2011, doi: <https://doi.org/10.1016/j.polymertesting.2010.10.011>.
- [14] C. Yan, L. Hao, L. Xu, and Y. Shi, "Preparation, characterisation and processing of carbon fibre/polyamide-12 composites for selective laser sintering," *Composites Sci. Technol.*, vol. 71, no. 16, pp. 1834-1841, 2011/11/14/ 2011, doi: <https://doi.org/10.1016/j.compscitech.2011.08.013>.
- [15] W. Zhong, F. Li, Z. Zhang, L. Song, and Z. Li, "Short fiber reinforced composites for fused deposition modeling," *Materials Science and Engineering: A*, vol. 301, no. 2, pp. 125-130, 2001.
- [16] G. D. Goh *et al.*, "Characterization of mechanical properties and fracture mode of additively manufactured carbon fiber and glass fiber reinforced thermoplastics," *Materials & Design*, vol. 137, no. Supplement C, pp. 79-89, 2018/01/05/ 2018, doi: <https://doi.org/10.1016/j.matdes.2017.10.021>.
- [17] X. Tian, T. Liu, C. Yang, Q. Wang, and D. Li, "Interface and performance of 3D printed continuous carbon fiber reinforced PLA composites," *Composites Part A: Applied Science and Manufacturing*, vol. 88, pp. 198-205, 9// 2016, doi: <http://dx.doi.org/10.1016/j.compositesa.2016.05.032>.
- [18] R. Matsuzaki *et al.*, "Three-dimensional printing of continuous-fiber composites by in-nozzle impregnation," *Scientific Reports*, vol. 6, p. 23058, 03/11 2016, doi: 10.1038/srep23058.
- [19] D. Klosterman, R. Chartoff, G. Graves, N. Osborne, and B. Priore, "Interfacial characteristics of composites fabricated by laminated object manufacturing," *Composites Part A: Applied Science and Manufacturing*, vol. 29, no. 9, pp. 1165-1174, 1998.
- [20] F. O. Sonmez and H. T. Hahn, "Thermomechanical analysis of the laminated object manufacturing (LOM) process," *Rapid Prototyping Journal*, vol. 4, no. 1, pp. 26-36, 1998, doi: doi:10.1108/13552549810197541.
- [21] P. Parandoush, L. Tucker, C. Zhou, and D. Lin, "Laser assisted additive manufacturing of continuous fiber reinforced thermoplastic composites," *Materials & Design*, 2017/06/06/ 2017, doi: <http://dx.doi.org/10.1016/j.matdes.2017.06.013>.

- [22] S. Melendi-Espina, C. Morris, T. Turner, and S. Pickering, "Recycling of carbon fibre composites," *Carbon* 2016, 2016.
- [23] F. N. Cogswell, "1 - An introduction to thermoplastic composite materials," in *Thermoplastic Aromatic Polymer Composites*: Butterworth-Heinemann, 1992, pp. 1-10.
- [24] P. K. Mallick, *Fiber-reinforced composites: materials, manufacturing, and design*. CRC press, 2007.
- [25] A. Riveiro *et al.*, "Experimental study on the CO2 laser cutting of carbon fiber reinforced plastic composite," *Composites Part A: Applied Science and Manufacturing*, vol. 43, no. 8, pp. 1400-1409, 2012/08/01/ 2012, doi: <https://doi.org/10.1016/j.compositesa.2012.02.012>.
- [26] E. M. Soliman, U. F. Kandil, and M. M. Reda Taha, "Investigation of FRP lap splice using epoxy containing carbon nanotubes," *J. Composite Constr.*, vol. 19, no. 2, p. 04014045, 2014.
- [27] D. Cree, T. Gamaniouk, M. L. Loong, and M. F. Green, "Tensile and lap-splice shear strength properties of CFRP composites at high temperatures," *J. Composite Constr.*, vol. 19, no. 2, p. 04014043, 2014.
- [28] S. Liu, X. Cheng, Q. Zhang, J. Zhang, J. Bao, and X. Guo, "An investigation of hygrothermal effects on adhesive materials and double lap shear joints of CFRP composite laminates," *Composites Part B: Engineering*, vol. 91, pp. 431-440, 2016/04/15/ 2016, doi: <https://doi.org/10.1016/j.compositesb.2016.01.051>.
- [29] C. Stokes-Griffin and P. Compston, "Laser-assisted tape placement of thermoplastic composites: the effect of process parameters on bond strength," in *Sustainable Automotive Technologies 2013*: Springer, 2014, pp. 133-141.
- [30] W. J. B. Grouve, L. Warnet, B. Rietman, H. Visser, and R. Akkerman, "Optimization of the tape placement process parameters for carbon-PPS composites," *Composites Part A: Applied science and manufacturing*, vol. 50, pp. 44-53, 2013.
- [31] A. Comer *et al.*, "Mechanical characterisation of carbon fibre-PEEK manufactured by laser-assisted automated-tape-placement and autoclave," *Composites Part A: Applied Science and Manufacturing*, vol. 69, pp. 10-20, 2015.
- [32] M. Hagino and T. Inoue, "Effect of carbon fiber orientation and helix angle on CFRP cutting characteristics by end-milling," *International Journal of Automation Technology*, vol. 7, no. 3, pp. 292-299, 2013.

- [33] N. Li, Y. Li, and S. Liu, "Rapid prototyping of continuous carbon fiber reinforced polylactic acid composites by 3D printing," *J. Mater. Process. Technol.*, vol. 238, pp. 218-225, 12// 2016, doi: <http://dx.doi.org/10.1016/j.jmatprotec.2016.07.025>.
- [34] "7075-T652 Aluminum." <https://www.makeitfrom.com/material-properties/7075-T652-Aluminum>. <https://www.makeitfrom.com/material-properties/7075-T652-Aluminum> (accessed 02/01/2018, 2018).
- [35] W. Jing, C. Hui, W. Qiong, L. Hongbo, and L. Zhanjun, "Surface modification of carbon fibers and the selective laser sintering of modified carbon fiber/nylon 12 composite powder," *Materials & Design*, vol. 116, no. Supplement C, pp. 253-260, 2017/02/15/ 2017, doi: <https://doi.org/10.1016/j.matdes.2016.12.037>.
- [36] J. Hector Sandoval and R. B. Wicker, "Functionalizing stereolithography resins: effects of dispersed multi-walled carbon nanotubes on physical properties," *Rapid Prototyping Journal*, vol. 12, no. 5, pp. 292-303, 2006.
- [37] C. C.M., F. J.Y.H., N. A.Y.C., and L. L., "Mechanical characteristics of fiber-filled photo-polymer used in stereolithography," *Rapid Prototyping Journal*, vol. 5, no. 3, pp. 112-119, 1999, doi: doi:10.1108/13552549910278937.
- [38] T. L. Bergman, A. S. Lavine, F. P. Incropera, and D. P. Dewitt, "Fundamentals of heat and mass transfer," ed: John Wiley & Sons New York, 2011.
- [39] S. Song, M. Yovanovich, and F. Goodman, "Thermal gap conductance of conforming surfaces in contact," *J. Heat Transfer*, vol. 115, no. 3, pp. 533-540, 1993.
- [40] M. Guo and Z. Wang, "On the analysis of an elliptical Gaussian flux image and its equivalent circular Gaussian flux images," *Solar Energy*, vol. 85, no. 5, pp. 1144-1163, 2011/05/01/ 2011, doi: <https://doi.org/10.1016/j.solener.2011.03.010>.
- [41] G. S. Springer and S. W. Tsai, "Thermal conductivities of unidirectional materials," *J. Compos. Mater.*, vol. 1, no. 2, pp. 166-173, 1967.
- [42] J.-l. Wang, M. Gu, W.-g. Ma, X. Zhang, and Y. Song, "Temperature dependence of the thermal conductivity of individual pitch-derived carbon fibers," *New Carbon Materials*, vol. 23, no. 3, pp. 259-263, 2008/03/01/ 2008, doi: [https://doi.org/10.1016/S1872-5805\(08\)60029-3](https://doi.org/10.1016/S1872-5805(08)60029-3).
- [43] W. N. dos Santos, J. A. de Sousa, and R. Gregorio, "Thermal conductivity behaviour of polymers around glass transition and crystalline melting temperatures," *Polym. Test.*, vol. 32, no. 5, pp. 987-994, 2013/08/01/ 2013, doi: <https://doi.org/10.1016/j.polymertesting.2013.05.007>.

- [44] T. Suzuki and J. Takahashi, "Prediction of energy intensity of carbon fiber reinforced plastics for mass-produced passenger cars," in *Ninth Japan International SAMPE Symposium JISSE-9, Tokyo, Japan*, 2005, pp. 14-19.
- [45] P. M. Schaefer, D. Gierszewski, A. Kollmannsberger, S. Zaremba, and K. Drechsler, "Analysis and improved process response prediction of laser- assisted automated tape placement with PA-6/carbon tapes using Design of Experiments and numerical simulations," *Composites Part A: Applied Science and Manufacturing*, vol. 96, pp. 137-146, 2017/05/01/ 2017, doi: <https://doi.org/10.1016/j.compositesa.2017.02.008>.

Chapter 5 - Finishing Operation for Additively Manufactured Carbon Fiber Composites

3D printing (also known as additive manufacturing) technology has the potential to revolutionize carbon fiber reinforced polymer composite (CFRP) production by increasing the flexibility of the fabrication process, reducing waste, and a significant cost saving. In this technology, 3D parts are fabricated by joining materials layer upon layer from a computer aided design (CAD) model. The direct transformation of a digital file to the finished product in an automated process is a substantial improvement over existing manual conventional methods of CFRP productions [1]. Recently, there has been enormous amount of research efforts to increase the mechanical properties of 3D printed CFRP composites. 3D printing CFRP composites with short carbon fiber (SCF) reinforcement was the main focus of the majority of recent works by using pre-blended filament, resin, or powders. Various 3D printing techniques could benefit from SCF reinforcement, including fused deposition modeling (FDM) [2-4], stereolithography (SLA) [5, 6], extrusion [7], and selective laser sintering (SLS) [8, 9]. These 3D printed composites could offer relative improvement over pure polymers and even composites with higher specific strength than Aluminum 6061-0 could be 3D printed [2]. However, CFRPs with SCF could not be a true replacement for high performance CFRP laminated composites with continuous carbon fiber (CCF) reinforcement. So far, only FDM [10-12] and laminated object manufacturing (LOM) [13-15] have been used for 3D printing composites with continuous fiber reinforcement. The mechanical properties of these 3D printed composites are approaching conventionally produced CFRPs and could be replacing traditional techniques in various industries.

On the other hand, 3D printing technologies for composites are required to resolve issues regarding surface finish and geometric tolerance before becoming mainstream for industrial

applications. Layered structure of the 3D printed parts deteriorates the surface finish and the free standing fabrication process could result in poor tolerances [16]. Substantial experimental and theoretical works aimed to optimize the 3D printing (mainly FDM) process parameters to improve the surface smoothness of the 3D printed components. The effects of layer thickness, wall thickness, and build orientation was the most significant for surface quality [17-19]. Achievable tolerances in FDM were reported in the range of 0.1-0.7 mm, which is again not suitable for high precise applications [20]. An inexpensive and straightforward solution to the quality issues of 3D printing could be finishing subtractive operations. Finishing processes could be categorized under chemical and mechanical processes. Chemical processes for polymers involve acetone vapor bath and could decrease surface roughness up to 90% and cause slight reduction in tensile strength [21, 22]. However, chemical finishing processes require deep knowledge of the material and, to date, have only been applied to Acrylonitrile Butadiene Styrene (ABS). In addition, they do not offer a consistent control over the dimensional accuracy of the treated parts. Conversely, mechanical finishing processes are less sensitive to the 3D printing material and overall are more attractive amongst industries and 3D printing services [23].

Mechanical processes are ideal for finishing 3D printed polymers and their composites and could offer an improved and consistent geometric tolerances over unfinished parts, as well as, a smoother surface finish. They can also be customized and only applied to certain areas of interest based on the application. Geometric complexity is the primary element in designing a manufacturing process and often a combined additive and subtractive manufacturing process is the optimal approach [24, 25]. Barrel finishing was employed to improve surface quality of the FDM process with higher repeatability compared to chemical processes. Moreover, it did require clamping of the part and the outcome was less sensitive to process parameters [26]. Abrasive flow

machining could also be used for finishing in micro/nano level with no effect on the mechanical properties [27]. Integrating FDM and 5-axis CNC machining for a hybrid additive and subtractive manufacturing process could resolve the aforementioned issues regarding engineering quality of 3D printing. This hybrid system could use benefit of the both systems and use five-axis machining on a completed FDM part or trim the freeform surface fabricated by FDM to achieve more accurate dimensions and better surface finish [28]. Currently, there is a significant research gap in mechanical finishing operations of 3D printed polymers and their composites. To the best of the author's knowledge there has not been any research effort on finishing operations of 3D printed polymer composites and only few works investigated mechanical finishing for a limited number of polymers.

In this chapter, CNC machining and rotary ultrasonic machining (RUM) were chosen as finishing processes for 3D printed continuous CFRP composites. RUM can be a great candidate as a mechanical finishing operation for additive manufacturing of CFRPs. Ultrasonic machining uses mechanical vibrations which is converted from high frequency electrical energy via a combination of transducer and booster. This vibration is then transmitted through an assembly of horn and tool. RUM on the other hand involves a tool which simultaneously vibrated and rotated, reducing out-of-roundness compared to conventional ultrasonic machining [29]. The feasibility of RUM in drilling CFRPs has been already verified in several works with reduced tool wear, higher surface quality, decreased delamination, and improved chip-removal rate relative to conventional drilling. Moreover, RUM could drill holes in CFRP without any fiber pull-out and taper [30-32]. Here, CNC and RUM finishing was applied to two 3D printing technologies of FDM and laser assisted-laminated object manufacturing (LA-LOM). The FDM 3D printer used in this study could produce continuous and short carbon fiber reinforcement. The chopped carbon fiber was pre-

blended in the thermoplastic matrix and continuous carbon fiber was deposited between layers during the 3D printing process using an additional depositing nozzle similar to ref. [33, 34]. On the other hand, the LA-LOM system used prepreg continuous carbon fiber reinforced polymer sheets and therefore offered continuous fiber reinforcement. This technique was inspired by the LOM process with a modified consolidation process. The laser assisted consolidation phase in LA-LOM improves the LOM bonding process by using a laser source instead of a hot roller. LOM, with post curing cycles, has been used to fabricate epoxy composites with continuous fiber reinforcement [13, 14]. In our system, prepreg sheets were cut based on the CAD cross-section and then bonded layer upon layer using a laser beam and a consolidation roller. Potentially, the in-house developed LA-LOM system could achieve stronger interfacial bonding relative to FDM owing to its laser assisted consolidation process. In the present work, we performed face and peripheral milling on top and side surfaces of the 3D printed CFRP composites with varying cutting depths. In addition, we performed RUM drilling on both using varying machining conditions on the additively manufactured CFRP plates to explore the performance of the process and the quality of the drilled holes. The surface morphology of the finished parts was investigated and compared based on the 3D printing technology and the machining conditions.

Experimental

Materials

The prepreg carbon fiber (CF)/Polyamide 6 (PA6) composite, used for the LA-LOM, was supplied by Celanese Corp, Dallas, TX. The Celstran CFR-TP PA6 CF60-03 prepreg composite sheet had 60 wt. % (48.5 vol. %) continuous CF content with sheet thickness of 130 μm . The materials used in the FDM 3D printer was purchased from Markforged. In this study, nylon

composite material was used, which was reinforced with short CF with the commercial name of ONYX. The continuous CF for the FDM machine was also purchased from Markforged.

LA- LOM

This method was inspired by the traditional LOM process; however, the bonding process was modified to develop a more efficient bonding process for prepreg CFRP materials (Figure 5-1). The CAD model of the desired geometry was sliced into 2D cross sections to determine the path for the laser cutter. Each cross section were then laser cut using a CO₂ laser cutter with a maximum power of 100 W (Figure 5-1 (a)). 60% of the laser power used for the cutting process with cutting speed of 50 mm/s and laser spot diameter of 0.8 mm. After laser cutting of each layer, they were stacked on top of the previous layer, prior to the laser consolidation process (Figure 5-1 (b)). The laser beam heated the nit point under the roller from the top, with 20° angle, just before compressed by the stainless steel roller with the diameter of 41.25 mm (Figure 5-1 (c)). The laser beam had a Gaussian power distribution with 6 mm diameter. This 100 W CO₂ laser was purchased from Beijing Reci Laser Technology, China. We used 29% of the laser power for the bonding process with the scanning speed of 6 mm/s. In this setup, the roller and the laser beam were stationary and the stage held the moving part. After bonding the entire surface of each layer with 3 mm spacing between scanning lines, the next layer was cut and bonded layer upon layer until the desired 3D geometry was achieved. The additively manufactured laminates were then compressed with the pressure of 1.2 kPa and cured at 220 °C for 2 hours in an isothermal furnace. The CFRP plates had carbon fiber orientation of [0°/90°]_s (cross-ply). The overall dimensions of the CFRP plates fabricated via LA-LOM were 8.3×27×27 mm.

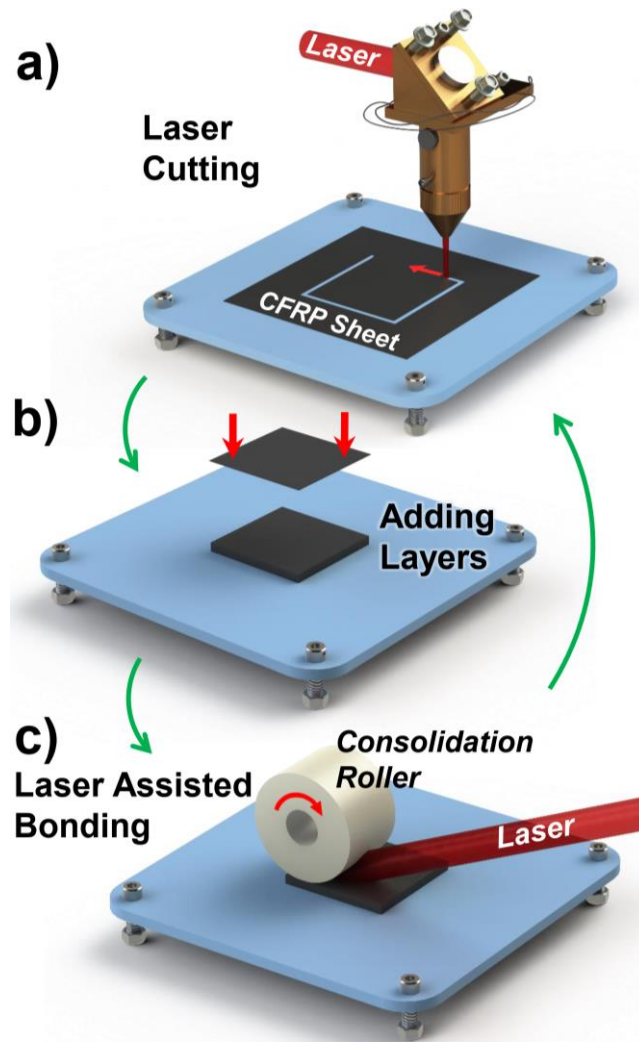


Figure 5-1 Schematic of the LA-LOM process for each layer: a) laser cutting of the prepreg CFRP sheets, b) adding the pre-cut cross section on top of the previous layers, and c) laser assisted bonding of the prepreg CFRP layer using a laser beam and a consolidation roller.

FDM 3D Printing

The FDM printed CFRP plates were printed using Markforged MARK TWO 3D printer (Markforged, Watertown, MA). The FDM printed parts had both short and continuous CF reinforcement. The short CF reinforced matrix is a Nylon composites with the commercial name of ONYX. In addition, the parts were reinforced with continuous carbon fiber to further increase the CF content. The optimal images of the Markforged Mark two 3D printed and the 3D printing

mechanism are shown in Figure 5-2. The FDM 3D printed plates were 8.3×27×27 mm in dimensions. In the 3 mm thickness of the printed CFRP plates, 3 layers of continuous CF were used as reinforcement.

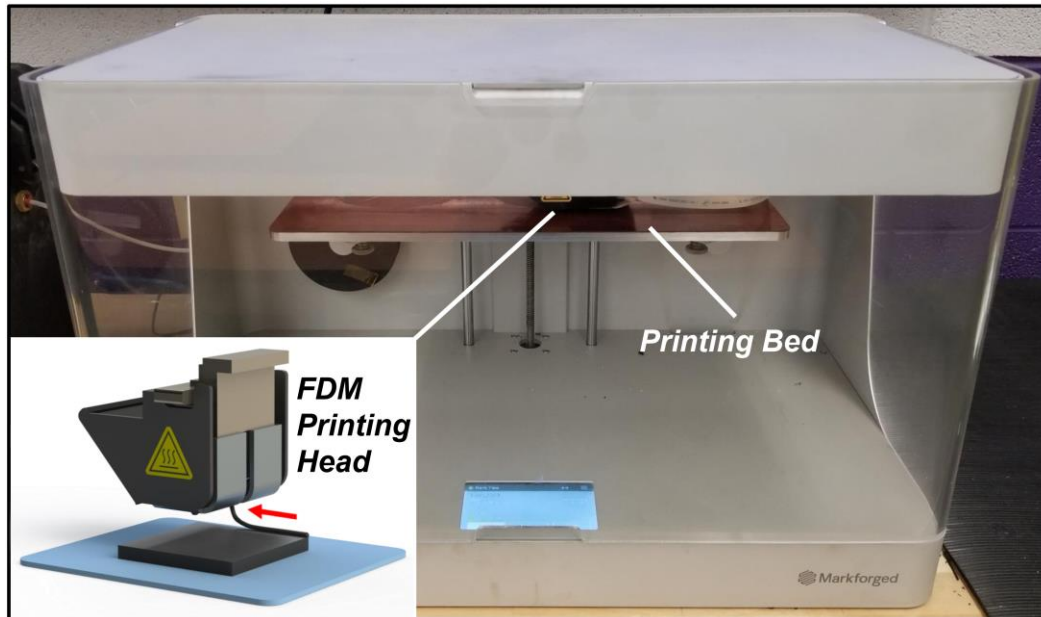


Figure 5-2 The Markforged FDM 3D printer used for CFRP fabrication showing the 3d printing configuration. The printing head consists of two nozzles, one for continuous carbon fiber and one for nylon composite filament.

CNC Machining

A 5-axis CNC milling machine was used to finish the horizontal and vertical surfaces of the 3D printed CFRP structures (Figure 5-3). The HAAS VF-E CNC Vertical Machining Center that was used in this work was purchased from Haas Automation, Inc. (Oxnard, CA). The tool that was used in the milling process was Accupro - 1/4" Diameter 2 flute carbide mill and was purchased from Accupro Technologies, Inc. (Green Bay, WI). All the finishing processes were performed using 4000 rpm rotation speed and 15 inch/min cutting speed with a varying cutting depth.



Figure 5-3 The CNC milling machine used for finishing the 3D printed CFRP composites.

Rotary Ultrasonic Machining

A RUM machine (Series 10, Sonic-Mill, Albuquerque, New Mexico, USA) was used to carry out the RUM process (Figure 5-4). The experimental setup involved an ultrasonic spindle system, a data acquisition system, and a coolant system, as shown in Figure 5-5. The ultrasonic spindle system was included an ultrasonic spindle, a power supply, an electric motor, and a control panel. The power supply generates a high frequency (20 kHz) electrical output from a low frequency (60 Hz) 110v electric input. A piezoelectric transducer in the ultrasonic spindle converts that high frequency electric signal to low amplitude mechanical vibrations. That low amplitude of the mechanical vibrations was amplified by the horn in the spindle and supplied to the cutting tool. The vibration amplitude could be adjusted by controlling the output of the power supply. The electric motor located on top of the spindle provides the rotational power to the spindle. The cold air cooling system consisted of an air compressor, oil and water filters, a vortex tube, a pressure

regulator and gauge, and a valve. Cold air is generated using a vortex tube, which has the capability to separate the compressed air stream into two separate streams, one of hot air and one of cold air. The cold air outlet of the vortex tube is fixed onto the spindle to blow out cold air (with a temperature of 5 °C and a pressure of 50 psi) through the cutting tool (core drill). The tool variables, namely inner and outer tool diameters, abrasive size, and abrasive concentration were fixed at 10 mm, 12 mm, 0.12 mm, and 100, respectively. Abrasive size is defined as the average diameter of the tool abrasives and abrasive concentration is defined as the weight of diamond per cm³ which is 4.4 carat/cm³. The data acquisition system contained a dynamometer (Model 9272, Kiestler Inc., Winterthur, Switzerland), a charge amplifier (Model 5070, Kiestler Inc., Winterthur, Switzerland), an analog to digital converter, a data acquisition card (PCIM-DAS 1602/16, Measurement Computing Corporation, Norton, MA, USA), and a computer with software (Type 2815A, Kiestler Inc., Winterthur, Switzerland).

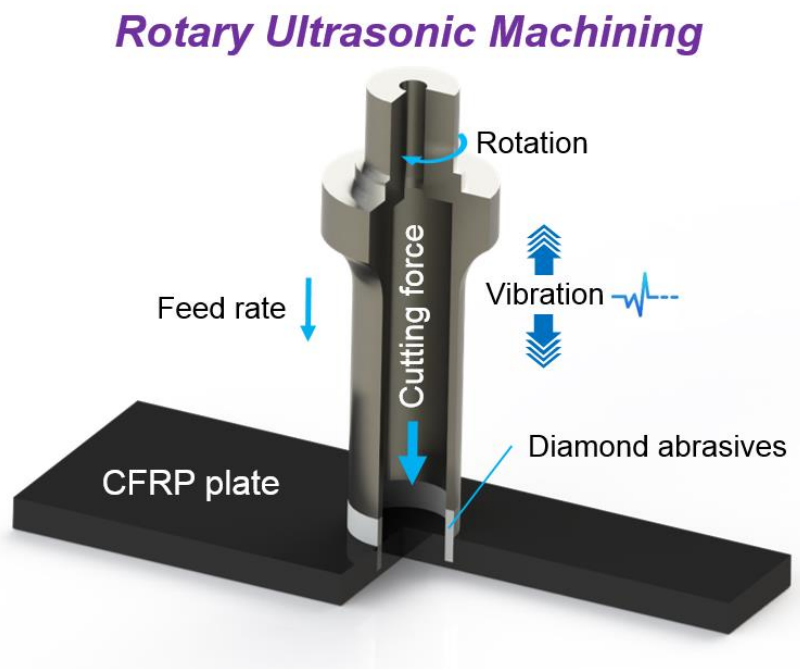


Figure 5-4 Schematic of the RUM of the fabricated CFRP plate with LA-LOM and FDM showing the RUM tool and cutting mechanism.

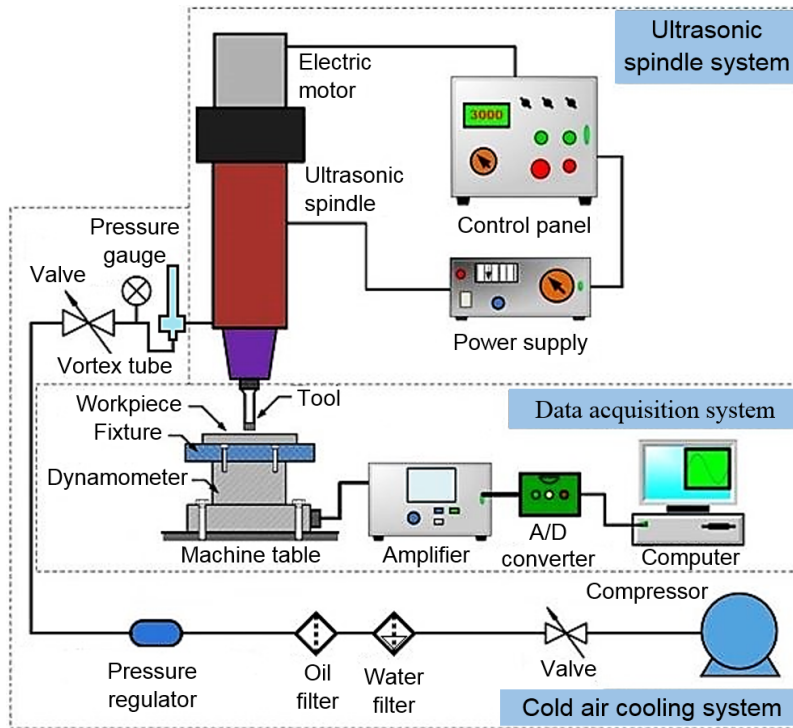


Figure 5-5 RUM experimental setup

Characterization

The 3D surface morphology of samples was measured with a Zygo NewView 7300 surface profiler. The scanning area was $1.40 \text{ mm} \times 1.05 \text{ mm}$ and the magnification was 50x. All the data obtained from the surface profiler was processed with a post-processing software MetroPro. The average of three tests for each condition was reported. The microscopic images of the surface was captured using an Olympus BX51 Fluorescence Microscope (Olympus Corporation, Shinjuku, Tokyo, Japan). $5\times$ and $20\times$ objectives lenses were used to study the surface morphology of the finished 3D printed composites. Scanning electron microscopy (SEM) (FEI Versa 3D Dual Beam, OR) images were acquired at an acceleration voltage of 20 kV and an emission current of $20 \mu\text{A}$. The SEM samples were coated with Gold particles with a coating thickness of 10 nm prior to the observation. A dynamometer measured the cutting force in RUM process. The dynamometer

signal was amplified using an amplifier. The signal was then converted a digital numerical signal. Dynoware software (Version 2.4.1.6 type 2825A-02, Kistler Instrument Corp, Switzerland) was used to observe the cutting force. 2D surface roughness was recorded on the cylindrical surface of the drilled hole after each drilling test by using a surface profilometer (Mitutoyo SJ-400, Mitutoyo Corporation, Kanagawa, Japan). The measurement range was 1.25 mm and the surface roughness was calculated by taking the average surface roughness value (R_a). Five measurements were taken for each experimental condition. The mean and standard deviation of these five R_a values are stated in this paper. The cutting temperature throughout the RUM process was monitored by an E40 FLIR thermal camera (FLIR Systems, Wilsonville, OR). The initial temperature and the highest temperature were then captured from the recorded video and used for analysis.

CNC Machining Results

The feasibility of the CNC finishing process was investigated by finishing the horizontal and vertical surfaces of LA-LOM and FDM components. The surface morphology and particularly surface roughness for various cutting depths were the main focus of this work. The rest of the machining parameters were kept constant, as described in the experimental section. The cutting depth ranged from 0.1 mm to 1.0 mm, as presented in Table 5-1. As the cutting depth increased in the machining process more fibers were protruded and they needed to be removed manually after the process. However, trimming the excess fibers on the surface with cutting depth under 1 mm did not require any additional process. The 3D profile and microscopic images of each surface were studied to reveal the surface roughness and surface features.

Table 5-1 The varying cutting depths used in the experimental study.

Condition	1	2	3	4	5	6
Cutting Depth	0.1 mm	0.2 mm	0.4 mm	0.6 mm	0.8 mm	1.0 mm

Surface Roughness

Improving surface roughness of 3D printed carbon fiber composites was the primary motivation of the present work. Initially, the surface roughness of the 3D printed surfaces were measured before the finishing process. Surfaces parallel and perpendicular to the 3D printing layers were the main focuses of this study. For this purpose, we 3D printed cubic structures and characterized their top and side surfaces before and after the finishing operation. An optical surface profiler was used to investigate the surface morphology of these surfaces and at least three measurements were carried out for each experimental condition. Figure 5-6 presents the resultant surface roughness values for both LA-LOM and FDM method for cutting depths varying from 0.1 to 1 mm. The cutting depth of zero in Figure 5-6 represents the unfinished surfaces prior to the CNC machining process. For unfinished LA-LOM surfaces, there is a huge disparity between the surface roughness values of the horizontal and vertical surfaces. The reason is the smooth surface of the prepreg CFRP sheets that gives the horizontal surfaces a smooth finish compared to surfaces 90° to the prepreg layers. The surface roughness for the horizontal and vertical unfinished LA-LOM samples was 2.0 ± 0.2 and 10.0 ± 0.4 μm , respectively (Figure 5-6 (a)). For all the investigated cutting depths, the horizontal surfaces maintained the smoother surface finish relative to vertical surfaces. Relatively, the average surface roughness of horizontal LA-LOM surfaces was below 3 μm . On the other hand, the vertical surface of LA-LOM structures showed improved surface finish

with higher cutting depths. The reason for this improvement is due to the machining of any potential misalignments and waviness of the 3D printed layers that might have happened during the LA-LOM process. Thus, machining these surfaces that are not parallel to 3D printed layers could drastically improve the surface finish. The average surface roughness of the vertical surfaces in LA-LOM composites could be reduced up to 70% by the proposed finishing process, demonstrating a substantial improvement over the original surface. It could also be observed that the variability of surface roughness was decreased by increasing the cutting depth showing more consistency in the surface finish.

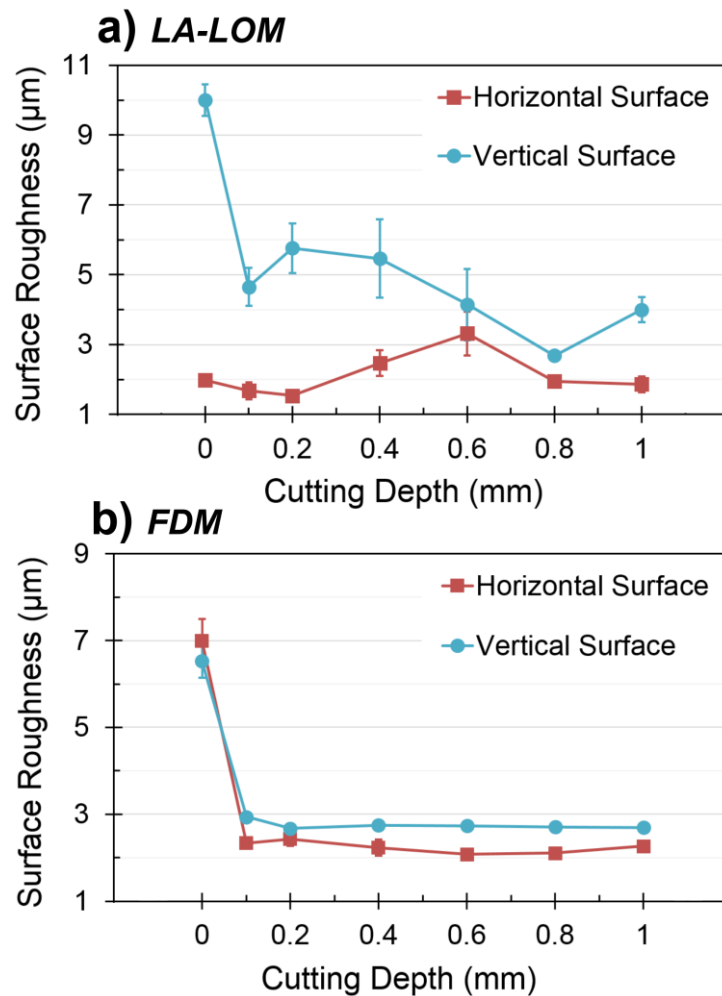


Figure 5-6 Surface roughness of the 3D printed CFRPs before and after finishing with varying cutting depths. Surface roughness of the horizontal and vertical surfaces for a) LA-LOM and b) FDM method is presented.

On the other hand, when we inspected the FDM 3D printed CFRP structures, more consistency could be observed between horizontal and vertical surfaces. As it can be seen in Figure 5-6 (b), the surface roughness of horizontal and vertical surfaces were in the range of 6 – 7 μm . Similar to unfinished surfaces, the roughness of the finished surfaces via CNC machining showed a good consistency for various cutting depths. The surface roughness of surfaces parallel to 3D printed layers was consistently and slightly lower than the vertical surfaces. This is due to the directional continuous and short carbon fiber which are aligned along the 3D printed layers. The surface roughness of the mechanically finished horizontal and vertical surfaces for FDM CFRP structures were around 2.2 and 2.7 μm , respectively. Overall, the proposed CNC finishing process could reduce the surface roughness of FDM parts up to 60% which is a substantial improvement in the surface finish. Additionally, Figure 5-6 (b) demonstrates that the variance of surface roughness was substantially decreased for all FDM surfaces and the surface finish exhibited a higher degree of consistency compared to the original 3D printed surfaces. It is to be noted that LA-LOM samples contained higher volume fraction of CCF reinforcement everywhere in the structure which increased the hardness of the CFRP composites and made it harder to machine. Conversely, The FDM parts only contained CCF in the center of the structure where no machining took place and overall had lower volume fraction of CCF compared to LA-LOM. Furthermore, the outer surfaces of FDM constructs only contained SCF reinforcement making it softer and easier to machine. In general, the surface roughness of the 3D printed carbon fiber composites fabricated via LA-LOM and FDM could be substantially reduced with a higher consistency in the finished surface morphology relative to the unfinished 3D printed surfaces.

LA-LOM Surface Morphology

The 3D profile of the LA-LOM 3D printed surfaces before and after the mechanical finishing process could reveal the surface morphology of these surfaces and helps us understand features associated with each surface. First, we analyzed the horizontal surfaces of LA-LOM CFRP laminates through the 3D surface profiles and optical microscope images (Figure 5-7). Here we only presented the original unfinished surface alongside with the finished surfaces with the cutting depth of 0.4 and 0.8 mm. As we illustrated earlier, the horizontal surface of the unfinished LA-LOM exhibited a smooth surface finish that could be observed in its surface profile (Figure 5-7 (a)). The unidirectional CCF created the directional surface morphology in Figure 5-7 (a). The microscopic images of this surface (Figure 5-7 (d)) also shows the unidirectional CCF on the top surface. Figure 5-7 (b) shows the 3D profile of the finished surface with 0.4 mm cutting depth and displays a slight increase in the surface roughness. The pattern created by the milling tool could be observed in surface profile and microscopic images of the finished surface. We also noticed more exposed CCF on the top surface. The same patterns could be seen in the finished horizontal surface with deeper cutting depth of 0.8 mm (Figure 5-7 (c) and (f)). The surface roughness did not exhibit a substantial change with increasing the cutting depth and similar surface morphology could be achieved. The proposed finishing process could be successfully applied for various cutting depth to attain the desirable geometry with considerably higher tolerances than what 3D printing could offer.

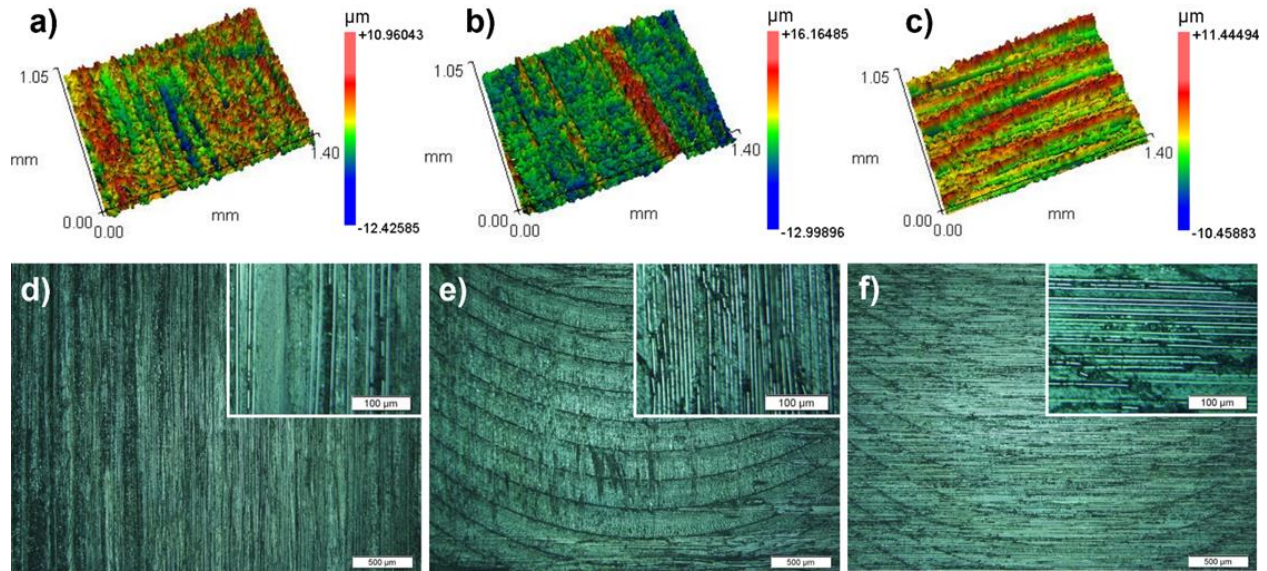


Figure 5-7 The surface morphology of the original and finished horizontal surfaces for LA-LOM structures. 3D surface profiles of the a) original unfinished surface and finished surfaces with b) 0.4 mm and c) 0.8 mm cutting depth. Microscopic images of d) the unfinished surface and finished surfaces with e) 0.4 mm and f) 0.8 mm cutting depth

Figure 5-8 displays the surface profile and surface morphology of the vertical surfaces before and after finishing. The unfinished surface exhibited a relatively rough surface finish due to the potential misalignment of the prepreg layers during the LA-LOM process. The layered microstructure of the CFRP laminated could be easily noticed in the 3D surface profile. Each prepreg layer had a thickness of 130 μm (Figure 5-8 (a)). The layers of the laminated structure and their fiber alignment could be clearly distinguished in Figure 6d. However, the finished surface with 0.4 mm cutting depth showed a relatively smoother surface finish (Figure 5-8 (b)). As explained earlier, the LA-LOM composite structures had a cross-ply $[0/90]_s$ fiber arrangement that is clearly visible in microscopic images of the finished surface (Figure 5-8 (e)). By increasing the cutting depth to 0.8 mm, the surface finish was improved dramatically and the surface features were more uniform with less defects (Figure 5-8 (c) and (f)). The high magnification microscopic

images could also confirm that the interfacial bonding of composites was not damaged, exhibiting a desirable surface morphology for industrial applications.

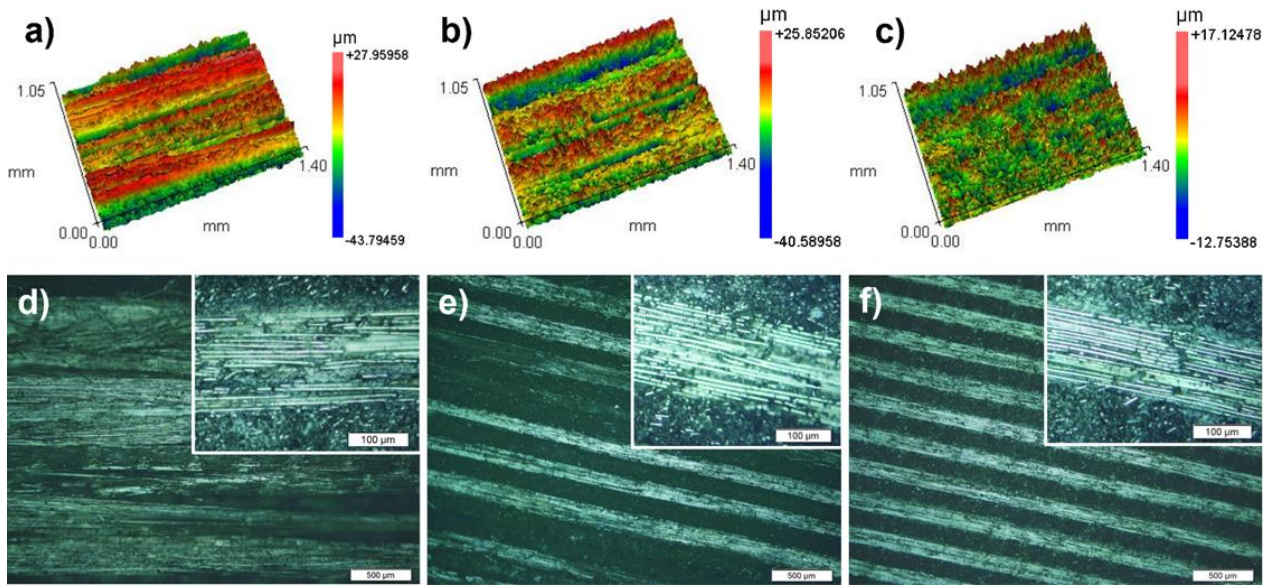


Figure 5-8 The surface morphology of the original and finished vertical surfaces for LA-LOM structures. 3D surface profiles of the a) original unfinished surface and finished surfaces with b) 0.4 mm and c) 0.8 mm cutting depth. Microscopic images of d) the unfinished surface and finished surfaces with e) 0.4 mm and f) 0.8 mm cutting depth.

FDM Surface Morphology

The microstructure of the CFRP composites fabricate via FDM 3D printing was vastly different with the microstructure of LA-LOM composites. Figure 5-9 shows the 3D profiles and microscopic images of the horizontal surfaces of FDM constructs. In the surface profile of the original top surface, the deposited beads are clearly noticeable that creating an undesirable rough surface finish (Figure 5-9 (a)). The microscopic images in Figure 5-9 (d), confirm this surface morphology and also shows the SCF reinforcement used near the surface. There are no CCF reinforcement near the surface of the FDM structures. On the other hand, the finished horizontal surfaces with 0.4 mm cutting depth showed a significant improvement in surface roughness (Figure 5-9 (b)). The optical images of the surface clearly shows the milling marks similar to LA-LOM samples, as well as the exposed SCFs on the top surface (Figure 5-9 (e)). By increasing the

cutting depth to 0.8 mm, comparable surfaces roughness and morphology could be attained. The 3D surface profile (Figure 5-9 (c)) and the optical microscopic images of the surface (Figure 5-9 (f)) display the surface features resulted from the finishing operation and the end milling tool. The direction of the carbon fiber reinforcement depended on the 3D printed layer that ended up being on top after the finishing process. Overall, a smooth surface finish could be achieved for FDM printed composites for any cutting depth.

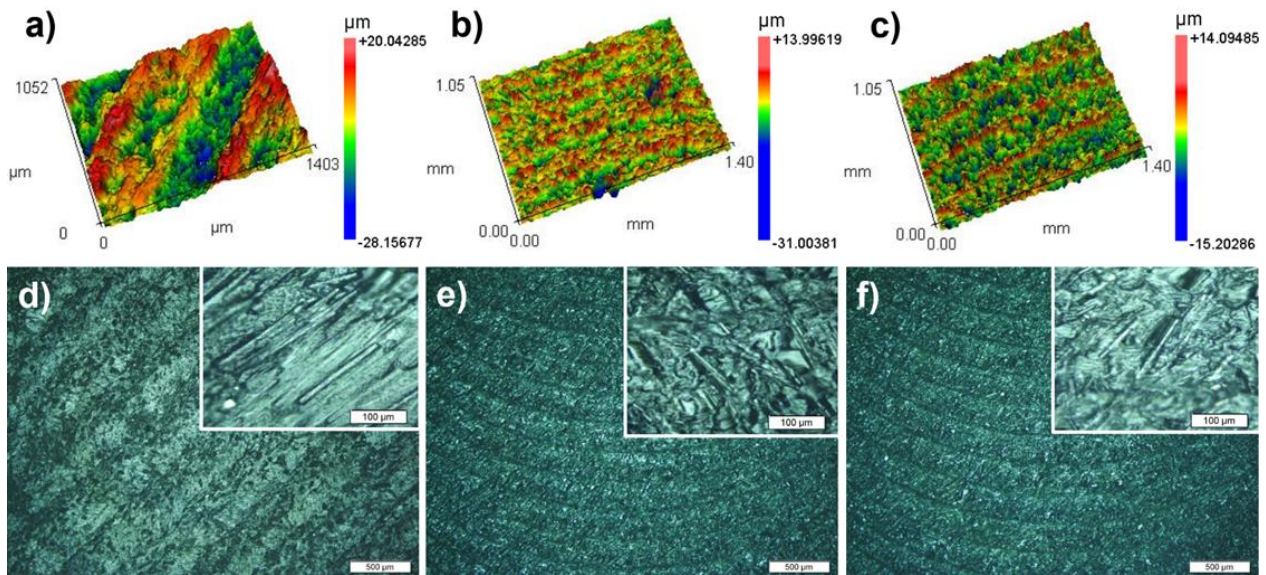


Figure 5-9 The surface morphology of the original and finished horizontal surfaces for FDM structures. 3D surface profiles of the a) original unfinished surface and finished surfaces with b) 0.4 mm and c) 0.8 mm cutting depth. Microscopic images of d) the unfinished surface and finished surfaces with e) 0.4 mm and f) 0.8 mm cutting depth

Figure 5-10 shows the profile and microscopic images of the vertical FDM surfaces before and after CNC finishing with 0.4 and 0.8 mm cutting depth. The layered microstructure of the original unfinished surface could be seen in the 3D profile (Figure 5-10 (a)) and the microscopic images of the unfinished surface (Figure 5-10 (d)). This kind of layered surface morphology causes a rough surface finish and decreases the consistency and reliability of the manufacturing process. As expected, the CNC finished vertical surfaces with 0.4 mm cutting depth exhibited a substantial

improvement in surface roughness (Figure 5-10 (b)). The vertical patterns resulted from the milling process could also be observed in Figure 5-10 (b) and (e). Interestingly, the layered surface morphology of the vertical surfaces were completely eliminated demonstrating a smooth surface. Carbon fibers could also be observed near the finished vertical surfaces and no sign of a layered structure could be noticed. Figure 5-10 (c) and (f) illustrates the 3D profile and features of the finished vertical surfaces with 0.8 mm cutting depth. The surface morphology was identical to the surfaces with lower cutting depth and the average surface roughness was comparable. In general, a consistent and predictable surface morphology could be achieved using the proposed finished method for FDM CFRP composites. The CNC finishing process could improve the surface finish and geometric tolerances of the FDM composites in an inexpensive and reliable manner suitable for a wide range of industries.

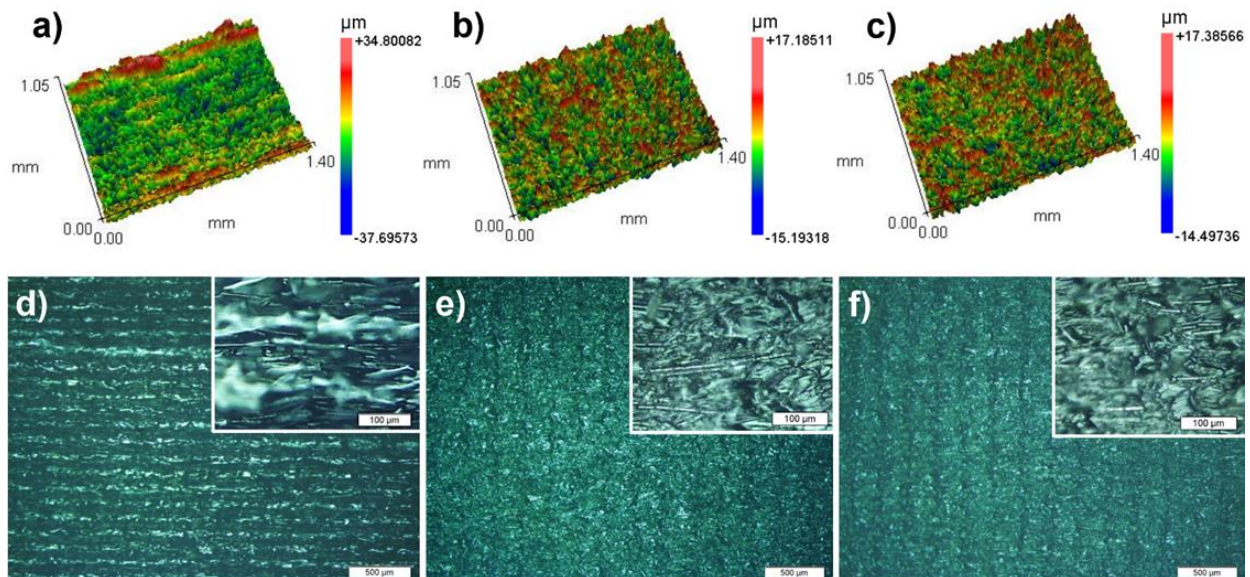


Figure 5-10 The surface morphology of the original and finished vertical surfaces for FDM structures. 3D surface profiles of the a) original unfinished surface and finished surfaces with b) 0.4 mm and c) 0.8 mm cutting depth. Microscopic images of d) the unfinished surface and finished surfaces with e) 0.4 mm and f) 0.8 mm cutting depth

RUM Results

The RUM was carried out on the CFRP plates fabricated by FDM and LA-LOM with a total seven different cutting conditions. In the present study, we investigated the effect of feedrate (FR), tool rotation speed (TRS), and ultrasonic power (UP) on the overall cutting quality. Surface quality, surface roughness, cutting force, and cutting temperature were studied to determine the performance and feasibility of RUM for additively manufactured CFRPs. Table 5-2 shows the seven machining conditions used in the current paper which included 3 levels of FD, TRS, and UP. 100% UP was equivalent to 900 W. Three replicates were carried out for each experimental condition.

Table 5-2 RUM experimental conditions

Condition	Feedrate (mm/s)	Tool rotation speed (rpm)	Ultrasonic power (%)
1	0.04	4000	20
2	0.04	4000	40
3	0.04	4000	60
4	0.04	2000	40
5	0.04	6000	40
6	0.02	4000	40
7	0.06	4000	40

Cutting Force

Cutting force is one of the most crucial variables of RUM and significantly influences the surface quality and machining performance. It could alter the fracture mechanism during the

machining process and directly affect the microstructure and surface quality. The 3D printed CFRP plates by FDM and LA-LOM had a layered micro structure and cutting force beyond their interfacial bonding strength at elevated temperatures could lead to delamination. However, LA-LOM and FDM CFRPs microstructures differs substantially due to the fundamentally different fabrication process. LA-LOM parts had a laminated structure with continuous CF reinforcement in each prepreg layer. On the other hand, the FDM parts used various layers of pure continuous CF between the polymeric layers. In addition to continuous CF, the nylon matrix had pre-blended chopped CF. The FDM parts generally exhibit porous microstructure with pores between the printing beads and potentially have weaker interfacial bonding relative to LA-LOM parts. During the modified LA-LOM process, the interface is heated beyond matrix melting point and further heat treatment ensured the full consolidation of the prepreg layers. Fig 3 shows the effects of machining conditions on the maximum cutting force occurred during the RUM process. The maximum cutting force in RUM of LA-LOM parts were generally higher than FDM printed CFRP plates. Increasing feedrate from 0.02 to 0.06 mm/s, steadily elevated the maximum cutting force from 55.0 ± 3.0 to 67.3 ± 2.6 N for FDM and from 65.5 ± 3.7 to 82.8 ± 11.3 N for LA-LOM (Fig 3a). Higher feedrate directly increase the material removal rate (MRR) and unsurprisingly increase the associated cutting force. In addition, the RUM cutting force predominantly affected by the interaction between active abrasive particles on the tool surface and the workpiece. The force resulted by this interaction increases in deeper penetration depths. At higher feedrates, the depth of penetration depth typically increase, hence increasing the interaction force and ultimately cutting force [32].

Tool rotation speed had an opposite effect on the maximum cutting force and higher tool rotation speed corresponded to lower maximum cutting force. The influence of tool rotation speed

was similar for FDM and LA-LOM parts with LA-LOM exhibited higher maximum cutting force. For LA-LOM, the maximum cutting force of over 100 N was occurred with TRS of 2000 rpm while it decreased to about 60 N for the TRS of 6000 rpm. Similarly, for FDM, cutting force decreased from about 90 N to 50 N when TRS changed from 2000 to 6000 rpm (Figure 5-11). The penetration depth of active abrasive particles into the workpiece decreases as tool rotation speed increases for fixed feedrate and ultrasonic power, resulting in a reduced interaction force, hence decreasing the cutting force.

Ultrasonic power did not have a similar influence on FDM and LA-LOM CFRP composites. It did not significantly alter the maximum cutting force when power was changed from 20 to 60 % in RUM of FDM composites. Conversely in RUM of LA-LOM parts, increasing the power increased the maximum cutting force. When ultrasonic power increases ultrasonic vibration amplitude also increases which results in a higher penetration depth of active abrasive particles into the workpiece material. The cutting force was ultimately increased due to this higher interaction force.

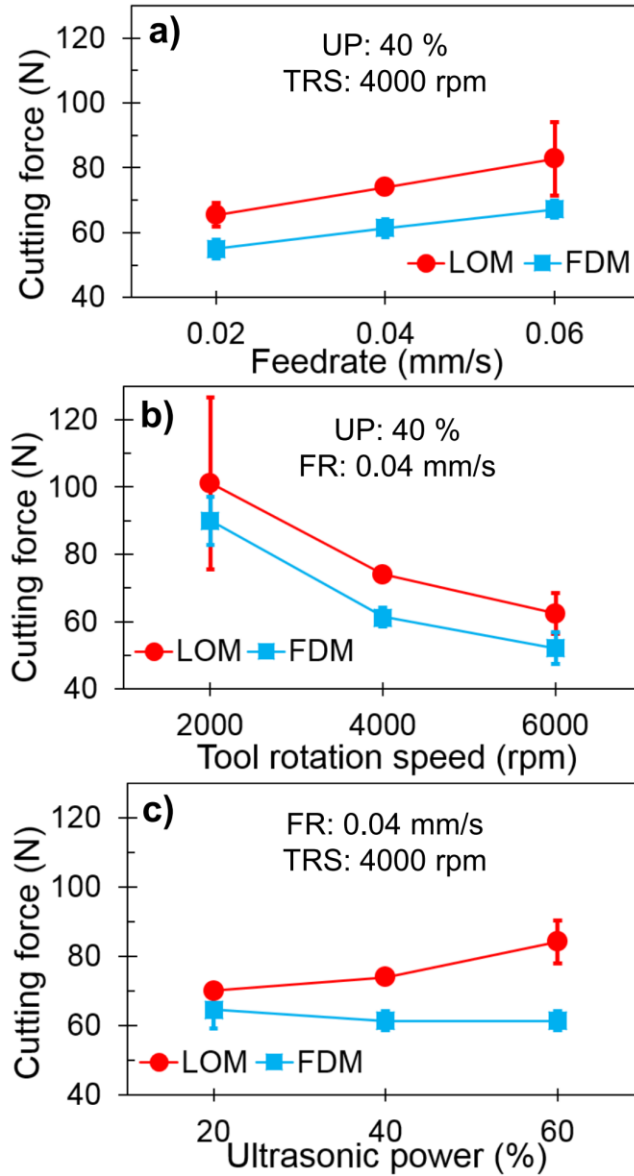


Figure 5-11 The effect of RUM machining conditions, namely, a) feedrate, b) tool rotation speed, and c) ultrasonic power, on the maximum cutting force

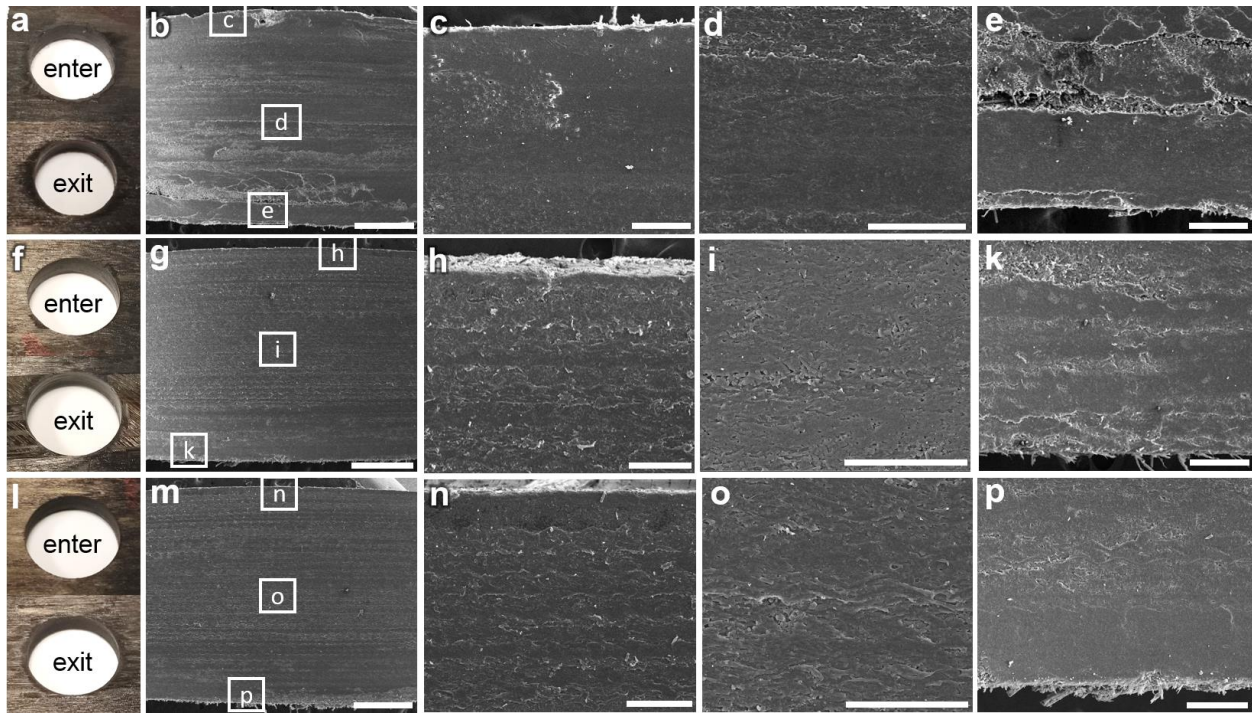


Figure 5-12 The digital photographs and SEM micrographs of the drilled holes in the LA-LOM parts for various feedrates. The optical images of the enter and exit surfaces of drilled holes for FRs of a) 0.02, f) 0.04, and l) 0.06 mm/s. The SEM micrograph of the surface morphology for the FRs of b, c, d, e) 0.02, g, h, i, k) 0.04, m, n, o, p) 0.06 mm/s. The scale bar in b, g, and m are 1 mm and the scale bar in the rest of SEM images are 200 μ m.

Surface Morphology

The investigation of the surface morphology of the drilled hole through SEM micrographs and digital images revealed better surface finishing quality and cleaner holes for LA-LOM part relative to FDM. Figure 5-12 shows the enter and exit surface of the drilled holes and SEM images of the hole surface for various feedrates in LA-LOM parts (experimental conditions 6, 2, and 7). In SEM images the surfaces near the entering surface, middle, and exiting surface were analyzed. When feedrate was set at 0.02 mm/s, decent surface quality was achieved, with some pull out delamination and rough surface finish near the exiting surface. With 0.04 mm/s feedrate, pull out delamination could be eliminated with no significant burr formation. Furthermore, surface finish was improved and the integrity of the microstructure was maintained throughout the RUM process

resulted in much cleaner holes. However, when the feedrate was increased to 0.06 mm/s, the drilled holes were further improved with an exceptional defect-free surface and no trace of delamination or burr formation, demonstrating the capability of RUM in drilling additively manufactured CFRP with our modified LA-LOM technology. The effects of feedrate on the surface morphology of the drilled holes in FDM parts are illustrated in Figure 5-13. The drilled holes in FDM parts exhibited remarkably higher amount of burr formation and rougher surfaces. The FDM printed parts had ununiformed microstructure and the pre-blended chopped carbon fiber in the nylon polymer with continuous fiber bundles between them, resulting in more uncertainty for RUM process. The continuous fiber reinforcement was exposed and could be observed in SEM images (Figure 5-13 (i)). However, burr formation and surface finish was decent with the feedrate of 0.04 mm/s and yielded the best results out the 3 implemented feedrates.

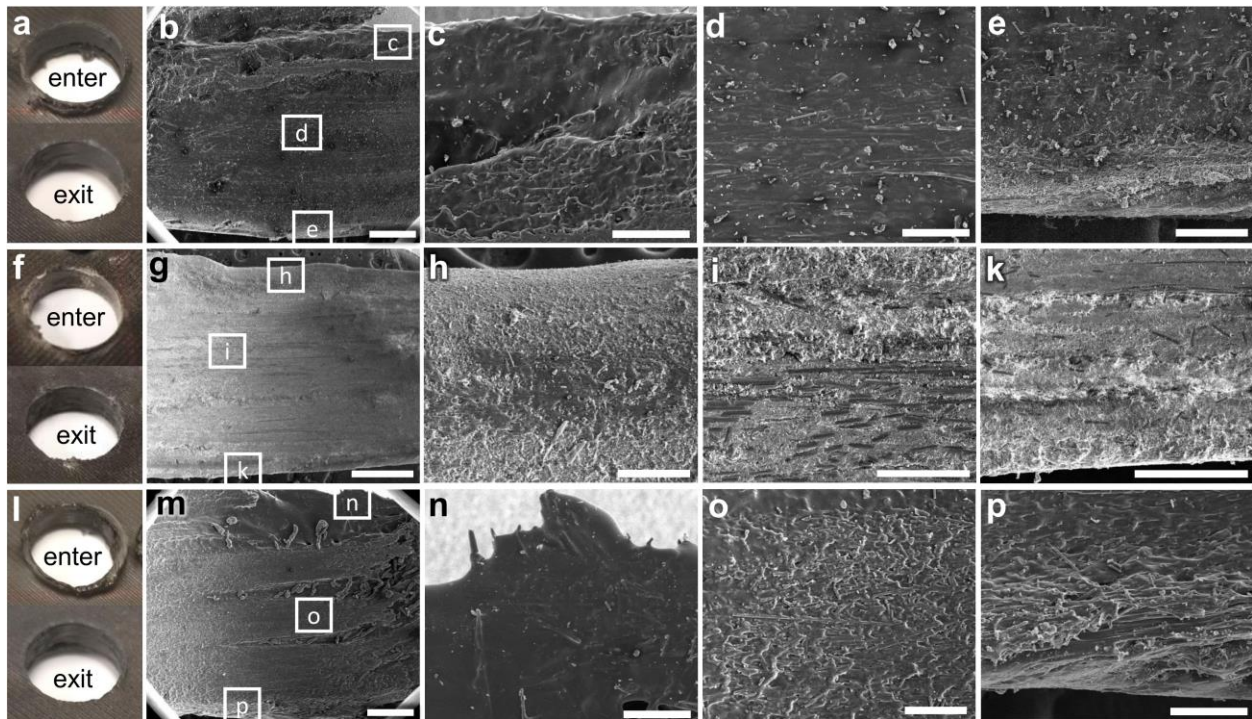


Figure 5-13 The digital photographs and SEM micrographs of the drilled holes in the FDM parts for various feedrates. The optical images of the enter and exit surfaces of drilled holes for FRs of a) 0.02, f) 0.04, and l) 0.06 mm/s. The SEM micrograph of the surface morphology for the FRs of b, c, d, e) 0.02, g, h, i, k) 0.04, m, n, o, p) 0.06 mm/s. The scale bar in b, g, and m are 1 mm and the scale bar in the rest of SEM images are 200 μm .

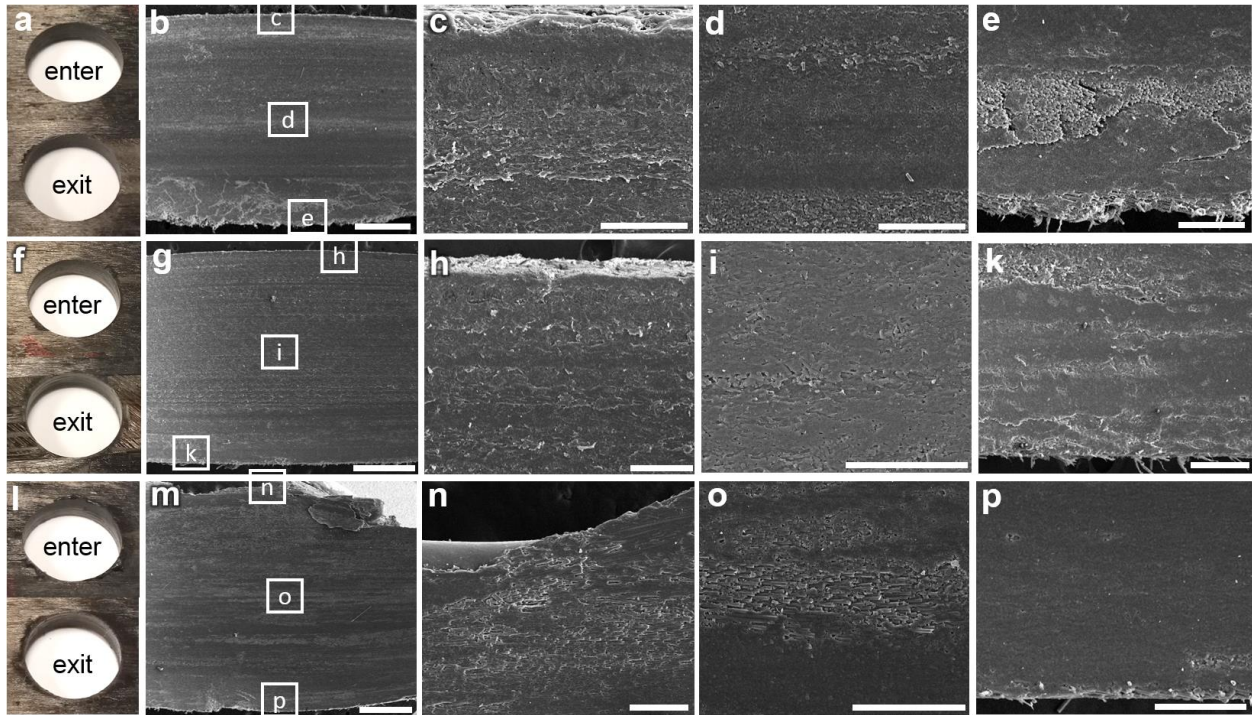


Figure 5-14 The digital photographs and SEM micrographs of the drilled holes in the LA-LOM parts for various tool rotation speeds. The optical images of the enter and exit surfaces of drilled holes for TRSs of a) 2000, f) 4000, and l) 6000 rpm. The SEM micrograph of the surface morphology for the TRSs of b, c, d, e) 2000, g, h, i, k) 4000, m, n, o, p) 6000 rpm. The scale bar in b, g, and m are 1 mm and the scale bar in the rest of SEM images are 200 μ m.

When we look at the surface of the holes with various TRS settings in LA-LOM (Figure 5-14), the finishing surface appeared to be smooth, except for some exposed carbon fiber and relatively rough surface finish with TRS of 2000 rpm. The continuous carbon fiber with 45° angle could be seen in Figure 5-14 (e). The enter and exit surface of the holes were clean and no pull-out delamination were noticed in the CFRP. The surface finish improved with increasing TRS to 4000 rpm and only some minimal surface defects were observed near the bottom of the CFRP plate. As TRS was increased to 6000 rpm, the most significant change was the extra burr formation on the top surface, visible in Figure 5-14 (l) and (m). The integrity of the CFRP laminate was preserved with no trace of delamination. The continuous fiber in 0° and $\pm 45^\circ$ could be observed in Figure 5-14 (o). The surface morphology near the exiting surface was smooth with minimal

defects on the surface. Overall, we could conclude that increasing feedrate in LA-LOM parts resulted in increased burr formation due to the higher cutting temperature in the RUM process. Figure 5-15 demonstrates the surface morphology of the RUM holes in FDM samples with regards to TRS. Although not steady, a trend of increasing surface roughness as TRS amplified could be seen in Figure 5-15. We also noticed increased burr formation on the top and bottom surface of the CFRP plate due to a higher cutting temperature with larger TRS. The hole surface appeared to have less defects with TRS of 2000 and 4000 and exhibit cleaner edges with less burr formation. Yet again we can confirm that the drilled holes in LA-LOM samples using RUM possessed smoother surface with less defects around the machining area, over FDM samples.

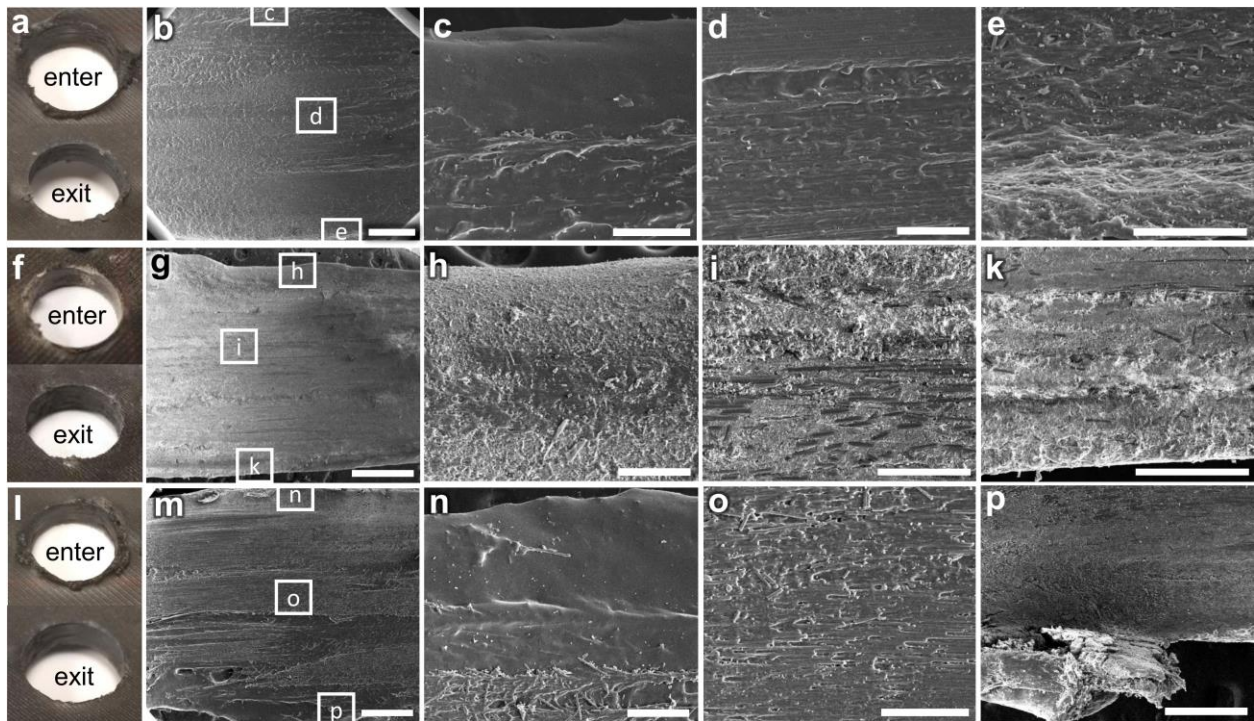


Figure 5-15 The digital photographs and SEM micrographs of the drilled holes in the FDM parts for various tool rotation speeds. The optical images of the enter and exit surfaces of drilled holes for TRSs of a) 2000, f) 4000, and l) 6000 rpm. The SEM micrograph of the surface morphology for TRSs of b, c, d, e) 2000, g, h, i, k) 4000, m, n, o, p) 6000 rpm. The scale bar in b, g, and m are 1 mm and the scale bar in the rest of SEM images are 200 μm .

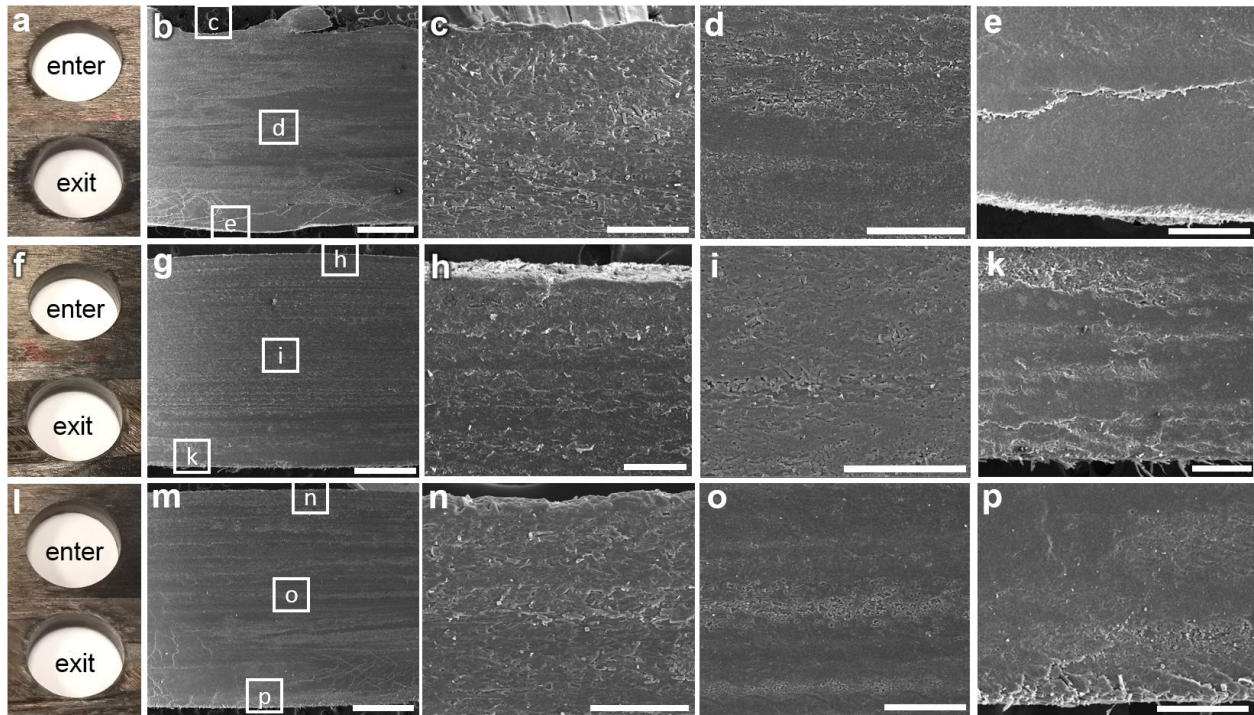


Figure 5-16 The digital photographs and SEM micrographs of the drilled holes in the LA-LOM parts for various ultrasonic powers. The optical images of the enter and exit surfaces of drilled holes for UPs of a) 20, f) 40, and l) 60 %. The SEM micrograph of the surface morphology for the UPs of b, c, d, e) 20, g, h, i, k) 40, m, n, o, p) 60 %. The scale bar in b, g, and m are 1 mm and the scale bar in the rest of SEM images are 200 μm .

The surface characteristics of the RUM holes with respect to ultrasonic power is illustrated in Figure 5-16 for LA-LOM and in Fig 9 for FDM. In LA-LOM samples, with the power of 20% most burr formation occurred and it decreased as power elevated to 40% and 60%. In addition, the area near the exiting surface possessed more defects when the power was set to 20%. The variations in surface roughness appeared to be insignificant in the range of ultrasonic power that was investigated in this study and in average surface finish was smooth in all LA-LOM samples (Figure 5-16). Pull out delamination was non-existent in these samples after RUM that shows the incredible interfacial bonding strength in the modified LA-LOM CFRPs. Overall, we can conclude that LA-LOM did not have a substantial effect on the surface morphology of the holes and high ultrasonic powers are not essential for RUM of additively manufactured CFRP. On the other hand,

RUM holes in FDM samples exhibited rougher surface finish and the surface defects appeared to increase with higher ultrasonic power. We could see that higher ultrasonic powers contributed to higher surface damage and the quality of the drilled holes with the power of 60% was poor. Burr formation was present for all samples; however, it was remarkably higher with 60% ultrasonic power. With higher ultrasonic power, chunks of the polymeric matrix were removed from the surface creating an uneven surface with exposed carbon fiber. Overall, the integrity of the FDM CFRP plates could not be maintained throughout the RUM process and the non-uniform microstructure of these CFRPs further complicated the machining process. We could claim that RUM of FDM parts should be performed with lower ultrasonic power to limit the surface defects, fiber-matrix debonding, and burr formation.

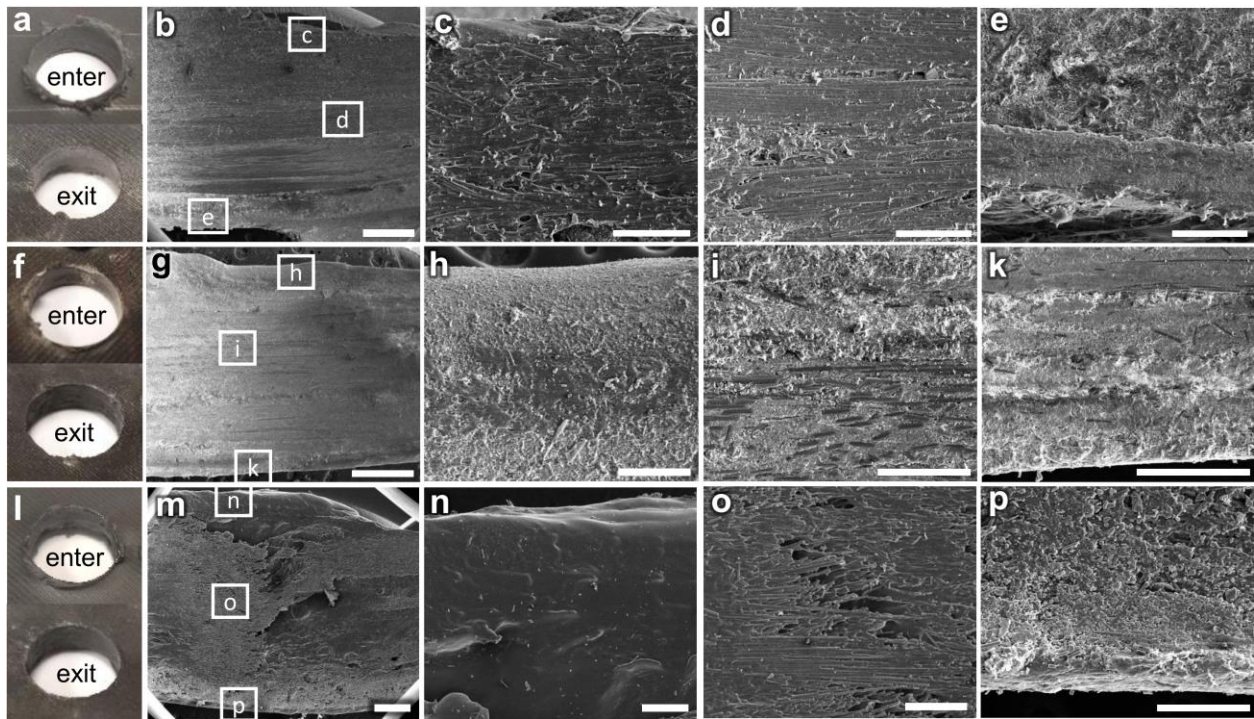


Figure 5-17 The digital photographs and SEM micrographs of the drilled holes in the FDM parts for various ultrasonic powers. The optical images of the enter and exit surfaces of drilled holes for UPs of a) 20, f) 40, and l) 60 %. The SEM micrograph of the surface morphology for the UPs of b, c, d, e) 20, g, h, i, k) 40, m, n, o, p) 60 %. The scale bar in b, g, and m are 1 mm and the scale bar in the rest of SEM images are 200 μm .

Surface Roughness

Typically, the holes made by additive manufacturing does not exhibit smooth surface due to the layer based nature of the process. Thus, surface roughness of the RUM surface in the additively manufacture components is of high significance for engineering applications. The 3D surface profile of the drilled hole surface via RUM was studied in this section for a deeper understanding of the surface morphology in LA-LOM and FDM parts. The measurement area was 1.40 mm by 1.05 mm of the cylindrical surface, inside the drilled holes. The curvature of the drilled hole surface was significant and affected the accuracy of the surface roughness measurements, therefore, the curvature of the surface was removed via software manipulation to acquire a flat image showing the surface features. Figure 5-18 presents the 3D surface profile of LA-LOM parts drilled with the 7 experimental conditions described in Table 5-2. The CFRP layers in LA-LOM samples were clearly recognizable in these images with less variation in surface roughness amongst different experimental conditions compared to FDM samples (Figure 5-19). The surface roughness varied between 0.573–1.706 μm for LA-LOM parts with similar surface features and no apparent surface defects. The RUM surface with experimental conditions 2 and 5 exhibited the smoothest surfaces with R_a values below 1 μm (Figure 5-18 (b) and (e)). It was noticed that the TRS had a positive effect on the surface smoothness and higher TRS contributed to a lower surface roughness. Figure 5-19 shows the 3D surface profiles of the hole surface in FDM samples. The first evident difference with the drilled holes in LA-LOM parts was the rougher surface and larger amount of the surface defect in FDM samples. The R_a values varied in the range of 2.023–6.048 μm with some distinct differences in the surface features across various experimental conditions. The layered structure of the FDM parts are observable in some of the profile images, however, the RUM surfaces were completely altered in some samples due to the cutting forces higher than the

interfacial bonding strength. It could be observe that experimental conditions 2 and 3 resulted in the best surface roughness values which was below 3 μm . Overall, the RUM surface in FDM samples were severely damaged and the most probable explanation is the high cutting force and temperature that overwhelmed the interfacial bonding and the materials used in the FDM CFRP composite. The LA-LOM samples that were additively manufactured in-house was better suited for the RUM process with a stronger interfacial bonding and a higher volume fraction of carbon fiber.

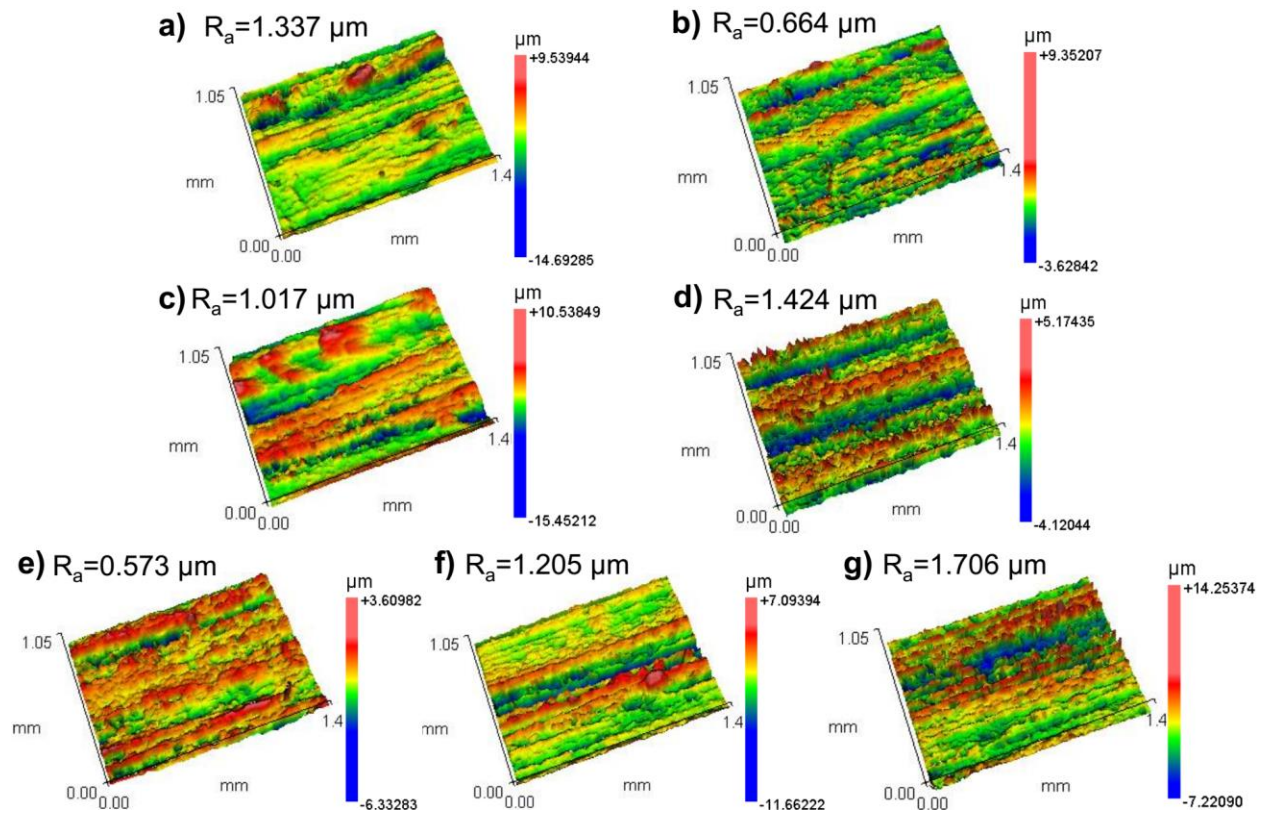


Figure 5-18 3D surface profile and the corresponding surface roughness of the RUM surface for LA-LOM CRFP plates using experimental conditions a) 1, b) 2, c) 3, d) 4, e) 5, f) 6, and g) 7.

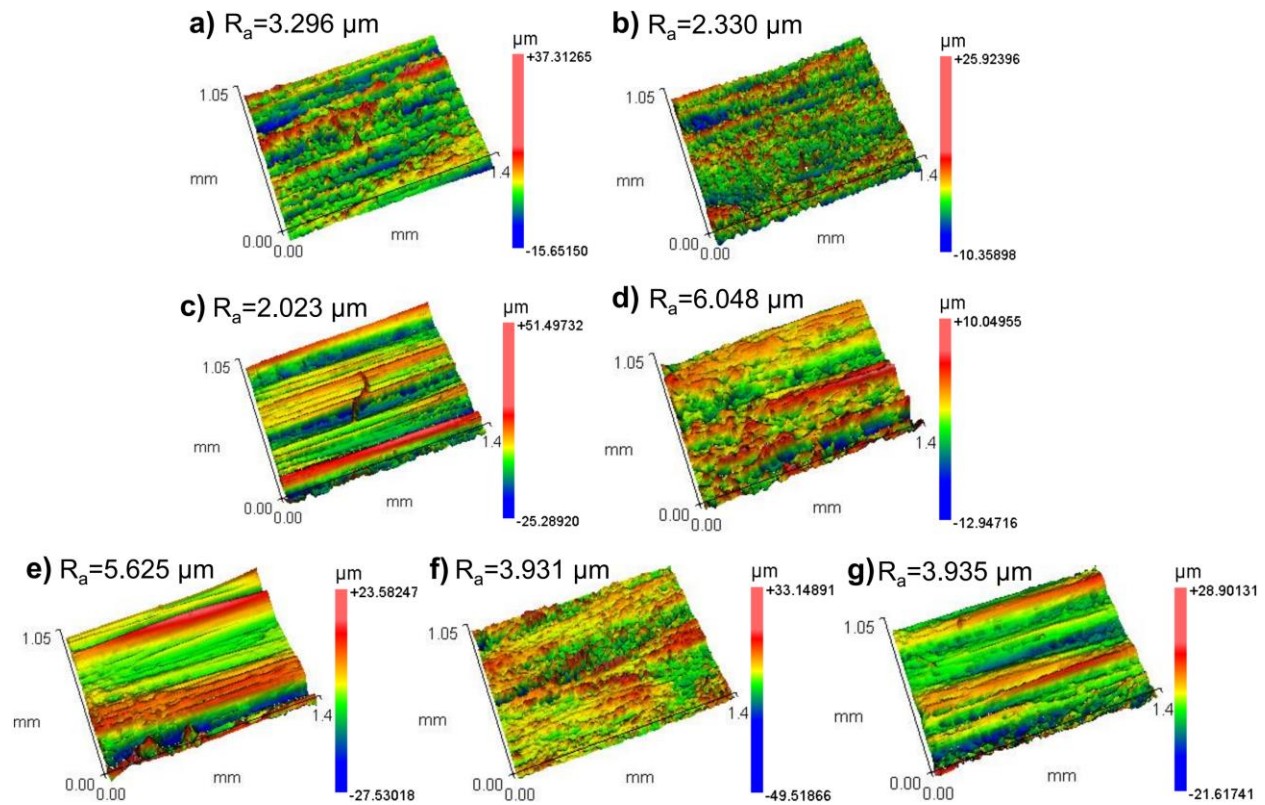


Figure 5-19 3D surface profile and the corresponding surface roughness of the RUM surface for FDM CRFP plates using experimental conditions a) 1, b) 2, c) 3, d) 4, e) 5, f) 6, and g) 7.

In order to investigate the trend of changes in the surface roughness relative to processing conditions, additional 2D surface roughness measurements were carried out. This time, 5 separate measurements were performed from various locations of the cylindrical surface inside the drilled holes for each experimental condition and the average surface roughness values were computed. Figure 5-20 shows the average surface roughness of RUM surface for both FDM and LA-LOM with respect to FR, TRS, and UP. Expectedly, the drilled holes in the LA-LOM samples had overall smoother surfaces over FDM samples, in agreement with the previous 3D measurements. The surface roughness for RUM surface of LA-LOM samples increased with higher feedrates (Figure 5-20 (a)). When changing the FD from 0.02 to 0.04 mm/s the surface roughness slightly decreased but remained below $1 \mu\text{m}$. However, it exhibited a sharp increase to above $1.5 \mu\text{m}$ for the FD of

0.06 mm/s. As expected, with increasing the TRS for LA-LOM parts, from 2000 to 6000 rpm, average surface roughness marginally decreased from about 1 μm to about 0.8 μm (Figure 5-20 (b)). Fig 10c shows that higher ultrasonic powers resulted in a slightly rougher surface, particularly when it was increased from 20% to 40% and ultimately 60%. Surface roughness ranged between 0.8 and 0.9 μm for LA-LOM CRFPs. Overall, the FDM parts exhibited considerably higher surface roughness affected by burr formation and delamination. The best result ($1.17 \pm 0.19 \mu\text{m}$) were obtained with power of 40%, TRS of 4000 rpm, and FR of 0.04 mm/s. The surface roughness of the majority of the other FDM samples were above 2 μm .

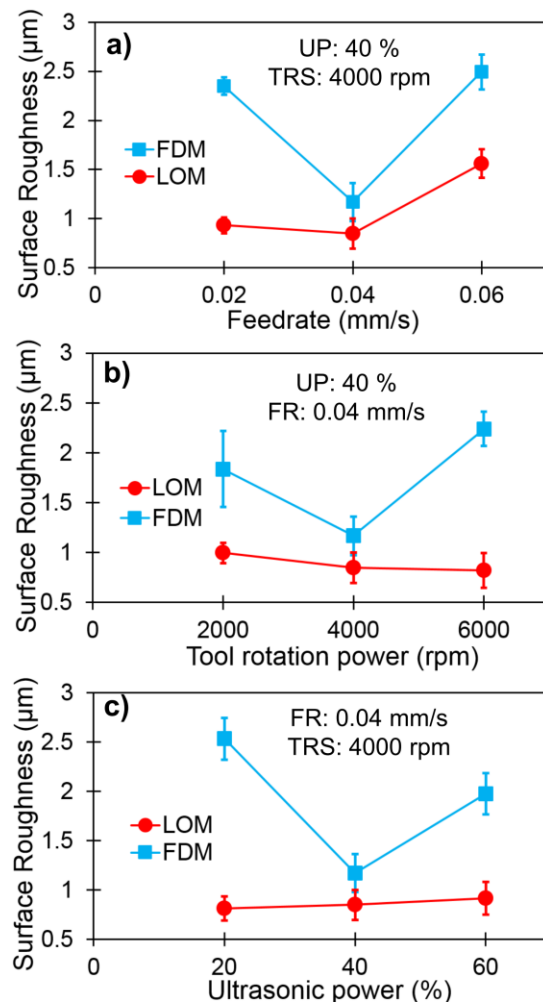


Figure 5-20 The influence of machining conditions, namely, a) feedrate, b) tool rotation speed, and c) ultrasonic power, on the average surface roughness of the drill holes.

Cutting Temperature

Cutting temperature is tremendously important in any machining process and could directly alter microstructure and surface characteristics of the machined surface. In RUM, processing conditions, type of coolant, and material properties are the major determinant factors of cutting temperature. Here, the RUM process used air cooling as oppose to fluid cooling. The decision was made on premise that polymers have high fluid absorbance and it can lead to delamination and affect mechanical properties of CFRP. Figure 5-21 shows the maximum temperature increase in the RUM process with air cooling. We used the temperature increment because the starting temperature can differ significantly between samples. The temperature increment was calculated based on the thermal images obtained from a FLIR camera during the RUM process. As the micrographs of the surface also suggested, the cutting temperature increment was lower for LA-LOM in all cases. Changing feedrate from 0.02 to 0.04 mm/s and ultimately 0.06 mm/s for both LA-LOM and FDM, decreased and increased temperature increment, respectively (Figure 5-21 (a)). TRS of 2000 and 4000 rpm for LA-LOM yielded similar temperature increments for LA-LOM while 6000 rpm TRS decreased it from 57 to 36 °C. For FDM, temperature increment decreased and increased by increasing the TRS from 2000 to 4000 rpm and ultimately 6000 rpm, respectively. On the other hand, ultrasonic power had the least effect on the temperature increment, as it can be observed in Figure 5-21 (c).

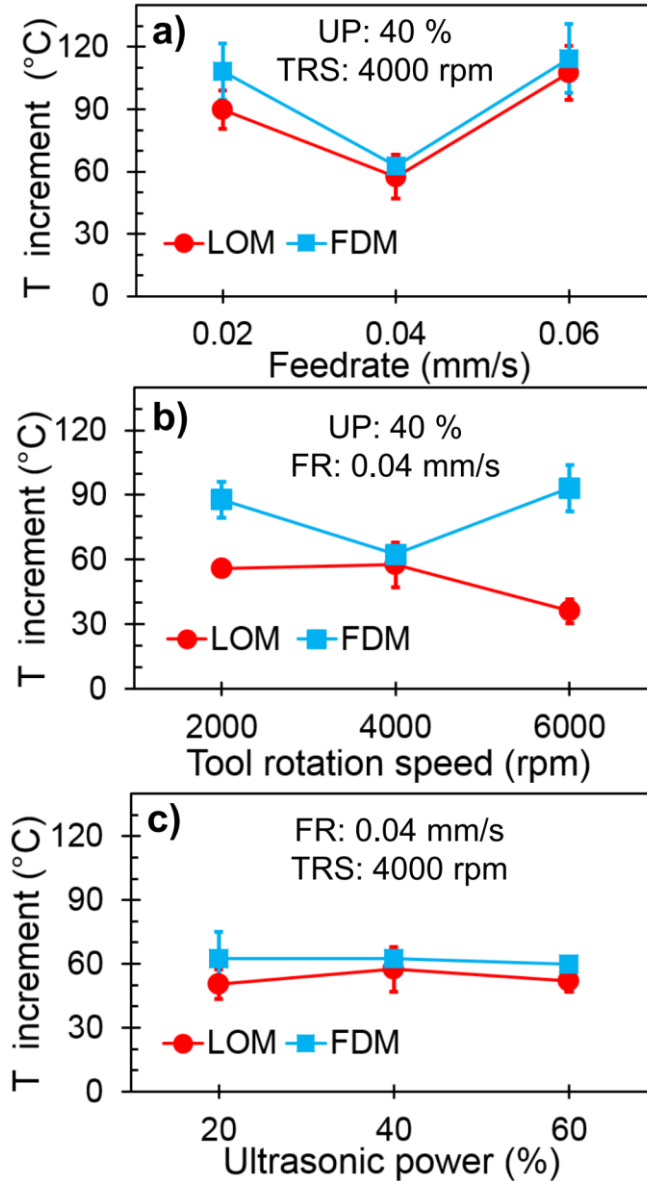


Figure 5-21 The influence of RUM machining conditions, namely, a) feedrate, b) tool rotation speed, and c) ultrasonic power, on the increased temperature during the RUM process. Temperature increment is defined as the temperature difference between the starting point and the highest temperature occurred during RUM process.

High cutting temperatures during the RUM process could be particularly harmful for the polymer matrix of the CFRP composite. It could degrade and melt the matrix resulting in burr formation, rough surface, delamination, and decreased mechanical properties. The effect of process parameter on the temperature increase was already investigated, however, we studied the

maximum temperature occurred during the process for LA-LOM (Figure 5-22) and FDM (Figure 5-23) CFRPs. The temperature observation was performed for all the seven RUM experimental condition described in Table 5-2. With similar processing conditions, RUM of LA-LOM CFRPs resulted in lower cutting temperature relative to FDM CFRPS plates. The cutting temperature results confirmed the significantly higher amount of burr formation, thermal damage, and rougher surface in FDM parts due to a higher cutting temperature. It was observed that as feedrate increased, maximum cutting temperature decreased in LA-LOM parts. The temperature decrease was most probably due to the shorter machining time as feedrate increased. Conversely, the cutting temperature for LA-LOM was increased with higher tool rotation speeds, due to higher friction between tool and CFRP. Interestingly, ultrasonic power for both FDM and LA-LOM had minimal effect on the cutting temperature, as temperature increment analysis suggested in Figure 5-21 (c).

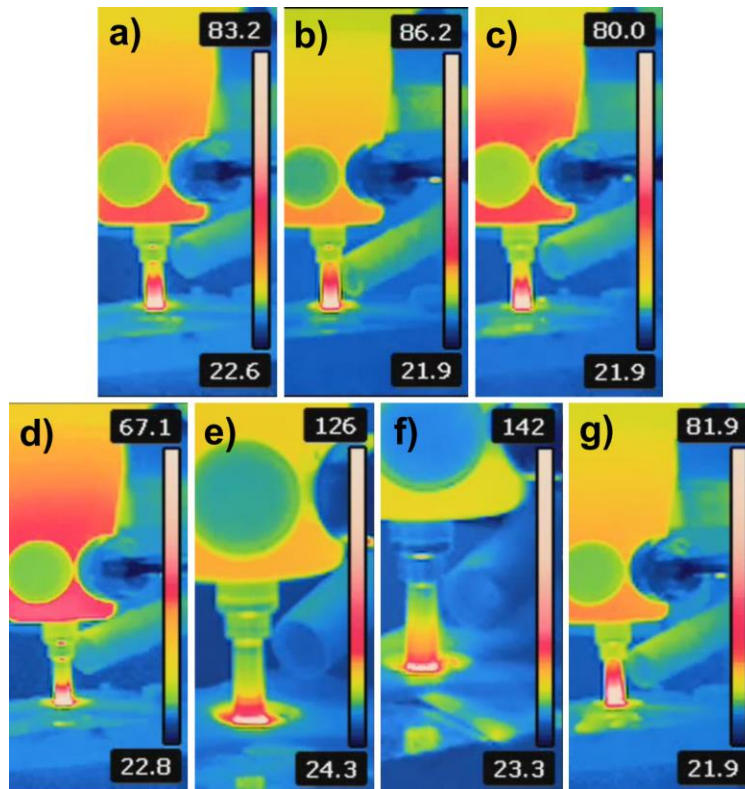


Figure 5-22 The thermal images of the highest temperature (°C) occurred during the RUM of LA-LOM parts for conditions a) 1, b) 2, c) 3, d) 4, e) 5, f) 6, and g) 7, acquired from FLIR thermal camera.

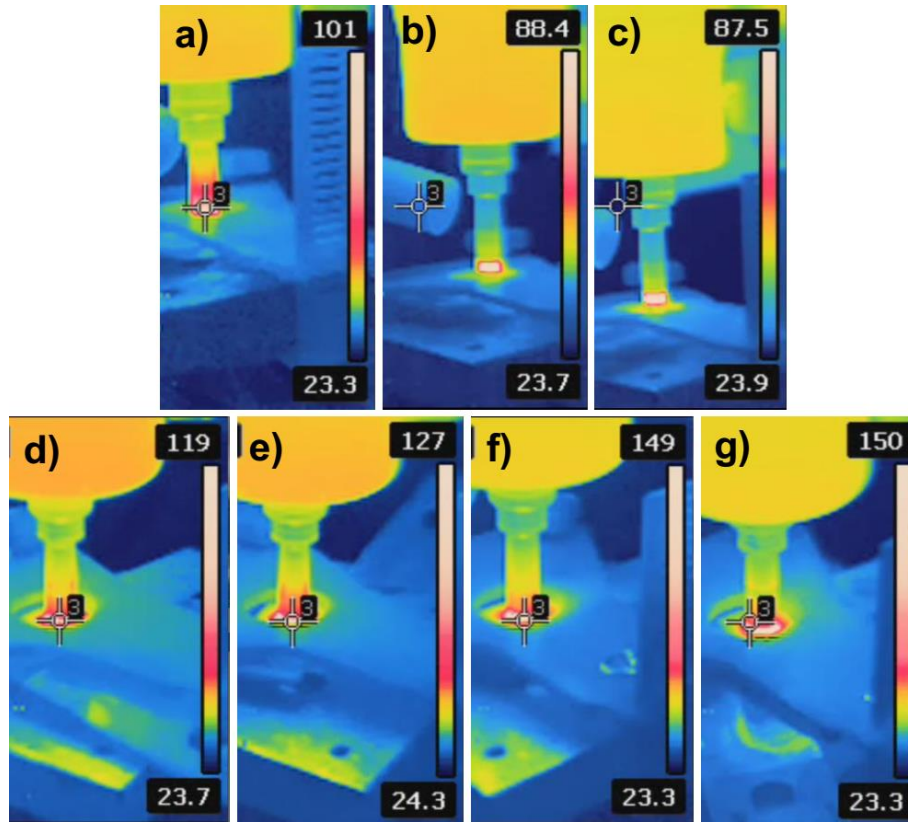


Figure 5-23 The thermal images of the occurred highest temperature (°C) occurred during the RUM of FDM parts for conditions a) 1, b) 2, c) 3, d) 4, e) 5, f) 6, and g) 7, acquired from FLIR thermal camera.

Conclusions

The feasibility of CNC milling and RUM drilling as mechanical finishing processes for 3D printed CFRP composite was studied through an experimental investigation. The 3D printing technology could process complex geometries unattainable by traditional molding methods, however, lacks certain engineering standards for surface finish and tolerance. Mechanical finishing processes could inexpensively improve the surface roughness and engineering quality of 3D printed composites. We employed two distinct 3D printing technologies of FDM and LA-LOM to fabricate the CFRP samples for this work. The CNC finishing process was performed using a 5-axis CNC milling machine with a varying cutting depth (0.1–1.0 mm). Furthermore, three levels

of various RUM parameters, namely feedrate (0.02, 0.04, 0.06 mm/s), tool rotation speed (2000, 4000, 6000 rpm), and ultrasonic power (20, 40, 60 %) was considered for the feasibility study. Both 3D printing technologies were capable of incorporating CCF reinforcement into the fabrication process, however, the mechanisms was entirely different. The LA-LOM process used prepreg CFRP sheets with imbedded CCF and was able to control the fiber alignment in each 3D printed layer. On the other hand, the FDM 3D printer that was used, had two separate nozzles for the CCF and polymeric matrix. LA-LOM could generally offer higher flexibility and CCF concentration than FDM.

The surface morphology and specifically surface roughness of the original 3D printed surfaces and finished surfaces were studied through 3D surface profiles and microscopic images of the respected surfaces. The surfaces parallel (horizontal) and perpendicular (vertical) to the 3D printed layers were studied before and after finishing with varying cutting depths. The surface roughness of unfinished horizontal and vertical LA-LOM surfaces was 2.0 ± 0.2 and 10.0 ± 0.4 μm , respectively. On the other hand, the surface roughness of horizontal and vertical surfaces of FDM components was in the range of 6 – 7 μm . As the result of the finishing process, the average surface roughness of the CFRP composites was improved 70% for FDM and 60% for LA-LOM components. The surface features of the finished CFRPs exhibited no delamination or defects and the integrity of the structure was fully maintained. The proposed finishing method in this work is an inexpensive solution to some of the most prominent drawbacks of 3D printed CFRP composites which are the surface finish and engineering quality. CFRP components with CCF reinforcement could be 3D printed and finished via CNC milling with less cost and waste compared to traditional CFRP production methods and a predictable engineering quality thanks to the mechanical finishing process.

Cutting force was generally higher in RUM of LA-LOM samples relative to FDM. It increased for both FDM and LA-LOM with higher feedrates. Tool rotation speed on the other hand had the opposite effect and the cutting force decreased as tool rotation speed increased, for both LA-LOM and FDM samples. Increasing the ultrasonic power contributed to a higher cutting force in RUM of LA-LOM components. However, the effects of ultrasonic power on cutting force in FDM parts was insignificant. The SEM micrographs revealed that the surface finish of the drilled hole in LA-LOM components was smoother than FDM counterpart with significantly less surface defects, burr formation, and pullout delamination. Higher feedrate and tool rotation speed yielded better surface morphology while the effect of ultrasonic power on the surface morphology was not substantial for both additive manufacturing techniques. The surface roughness of RUM holes was remarkably lower in the drilled hole in LA-LOM samples relative to FDM parts. In LA-LOM parts, surface roughness improved with lower feedrates, while higher tool rotation speed and ultrasonic power slightly increased and decreased the average surface roughness, respectively. The cutting temperature increase during the RUM process was typically higher for FDM samples over LA-LOM. We could conclude that typically higher feedrate increased temperature increment while higher tool rotation speed decreased it. In contrast, ultrasonic power had no significant influence on the temperature increment. In addition to temperature increment, Maximum cutting temperature was also higher in RUM of FDM parts resulting in more thermal damage and burr formation.

References

- [1] P. Parandoush and D. Lin, "A review on additive manufacturing of polymer-fiber composites," *Compos. Struct.*, vol. 182, no. Supplement C, pp. 36-53, 2017/12/15/ 2017, doi: <https://doi.org/10.1016/j.compstruct.2017.08.088>.
- [2] H. L. Tekinalp *et al.*, "Highly oriented carbon fiber–polymer composites via additive manufacturing," *Composites Sci. Technol.*, vol. 105, pp. 144-150, 2014.

- [3] F. Ning, W. Cong, J. Qiu, J. Wei, and S. Wang, "Additive manufacturing of carbon fiber reinforced thermoplastic composites using fused deposition modeling," *Composites Part B: Engineering*, vol. 80, pp. 369-378, 2015.
- [4] M. L. Shofner, K. Lozano, F. J. Rodríguez-Macías, and E. V. Barrera, "Nanofiber-reinforced polymers prepared by fused deposition modeling," *J. Appl. Polym. Sci.*, vol. 89, no. 11, pp. 3081-3090, 2003, doi: 10.1002/app.12496.
- [5] H. S. J. and W. R. B., "Functionalizing stereolithography resins: effects of dispersed multi-walled carbon nanotubes on physical properties," *Rapid Prototyping Journal*, vol. 12, no. 5, pp. 292-303, 2006, doi: doi:10.1108/13552540610707059.
- [6] A. Gupta and A. A. Ogale, "Dual curing of carbon fiber reinforced photoresins for rapid prototyping," *Polym. Compos.*, vol. 23, no. 6, pp. 1162-1170, 2002, doi: 10.1002/pc.10509.
- [7] B. G. Compton and J. A. Lewis, "3D-Printing of Lightweight Cellular Composites," *Advanced Materials*, vol. 26, no. 34, pp. 5930-5935, 2014, doi: 10.1002/adma.201401804.
- [8] R. D. Goodridge *et al.*, "Processing of a Polyamide-12/carbon nanofibre composite by laser sintering," *Polym. Test.*, vol. 30, no. 1, pp. 94-100, 2011/02/01/ 2011, doi: <https://doi.org/10.1016/j.polymertesting.2010.10.011>.
- [9] C. Yan, L. Hao, L. Xu, and Y. Shi, "Preparation, characterisation and processing of carbon fibre/polyamide-12 composites for selective laser sintering," *Composites Sci. Technol.*, vol. 71, no. 16, pp. 1834-1841, 2011/11/14/ 2011, doi: <https://doi.org/10.1016/j.compscitech.2011.08.013>.
- [10] G. D. Goh *et al.*, "Characterization of mechanical properties and fracture mode of additively manufactured carbon fiber and glass fiber reinforced thermoplastics," *Materials & Design*, vol. 137, no. Supplement C, pp. 79-89, 2018/01/05/ 2018, doi: <https://doi.org/10.1016/j.matdes.2017.10.021>.
- [11] X. Tian, T. Liu, C. Yang, Q. Wang, and D. Li, "Interface and performance of 3D printed continuous carbon fiber reinforced PLA composites," *Composites Part A: Applied Science and Manufacturing*, vol. 88, pp. 198-205, 9// 2016, doi: <http://dx.doi.org/10.1016/j.compositesa.2016.05.032>.
- [12] R. Matsuzaki *et al.*, "Three-dimensional printing of continuous-fiber composites by in-nozzle impregnation," *Scientific Reports*, vol. 6, p. 23058, 03/11 2016, doi: 10.1038/srep23058.

- [13] D. Klosterman, R. Chartoff, G. Graves, N. Osborne, and B. Priore, "Interfacial characteristics of composites fabricated by laminated object manufacturing," *Composites Part A: Applied Science and Manufacturing*, vol. 29, no. 9, pp. 1165-1174, 1998.
- [14] F. O. Sonmez and H. T. Hahn, "Thermomechanical analysis of the laminated object manufacturing (LOM) process," *Rapid Prototyping Journal*, vol. 4, no. 1, pp. 26-36, 1998, doi: [doi:10.1108/13552549810197541](https://doi.org/10.1108/13552549810197541).
- [15] P. Parandoush, L. Tucker, C. Zhou, and D. Lin, "Laser assisted additive manufacturing of continuous fiber reinforced thermoplastic composites," *Materials & Design*, 2017/06/06/ 2017, doi: <https://dx.doi.org/10.1016/j.matdes.2017.06.013>.
- [16] A. Boschetto, L. Bottini, and F. Veniali, "Integration of FDM surface quality modeling with process design," *Additive Manufacturing*, vol. 12, pp. 334-344, 2016/10/01/ 2016, doi: <https://doi.org/10.1016/j.addma.2016.05.008>.
- [17] N. Ayrilmis, "Effect of layer thickness on surface properties of 3D printed materials produced from wood flour/PLA filament," *Polym. Test.*, vol. 71, pp. 163-166, 2018/10/01/ 2018, doi: <https://doi.org/10.1016/j.polymertesting.2018.09.009>.
- [18] M. Altan, M. Eryildiz, B. Gumus, and Y. Kahraman, "Effects of process parameters on the quality of PLA products fabricated by fused deposition modeling (FDM): surface roughness and tensile strength," *Materials Testing*, vol. 60, no. 5, pp. 471-477, 2018/04/26 2018, doi: 10.3139/120.111178.
- [19] M. Pérez, G. Medina-Sánchez, A. García-Collado, M. Gupta, and D. Carou, "Surface Quality Enhancement of Fused Deposition Modeling (FDM) Printed Samples Based on the Selection of Critical Printing Parameters," *Materials*, vol. 11, no. 8, p. 1382, 2018.
- [20] C. K. Chua, K. F. Leong, and C. S. Lim, *Rapid prototyping: principles and applications*. World Scientific, 2003.
- [21] L. M. Galantucci, F. Lavecchia, and G. Percoco, "Quantitative analysis of a chemical treatment to reduce roughness of parts fabricated using fused deposition modeling," *CIRP Annals*, vol. 59, no. 1, pp. 247-250, 2010/01/01/ 2010, doi: <https://doi.org/10.1016/j.cirp.2010.03.074>.
- [22] N. Jayanth, P. Senthil, and C. Prakash, "Effect of chemical treatment on tensile strength and surface roughness of 3D-printed ABS using the FDM process," *Virtual and Physical Prototyping*, vol. 13, no. 3, pp. 155-163, 2018.
- [23] A. Boschetto, L. Bottini, and F. Veniali, "Finishing of Fused Deposition Modeling parts by CNC machining," *Robotics and Computer-Integrated Manufacturing*, vol. 41, pp. 92-101, 2016/10/01/ 2016, doi: <https://doi.org/10.1016/j.rcim.2016.03.004>.

- [24] O. Kerbrat, P. Mognol, and J.-Y. Hascoët, "A new DFM approach to combine machining and additive manufacturing," *Computers in Industry*, vol. 62, no. 7, pp. 684-692, 2011/09/01/ 2011, doi: <https://doi.org/10.1016/j.compind.2011.04.003>.
- [25] J. Y. Hascoet, P. Mognol, and O. Kerbrat, "Manufacturability analysis to combine additive and subtractive processes," *Rapid Prototyping Journal*, vol. 16, no. 1, pp. 63-72, 2010/01/19 2010, doi: 10.1108/13552541011011721.
- [26] A. Boschetto and L. Bottini, "Roughness prediction in coupled operations of fused deposition modeling and barrel finishing," *J. Mater. Process. Technol.*, vol. 219, pp. 181-192, 2015/05/01/ 2015, doi: <https://doi.org/10.1016/j.jmatprotec.2014.12.021>.
- [27] H. S. Mali, B. Prajwal, D. Gupta, and J. Kishan, "Abrasive flow finishing of FDM printed parts using a sustainable media," *Rapid Prototyping Journal*, vol. 24, no. 3, pp. 593-606, 2018.
- [28] W.-c. Lee, C.-c. Wei, and S.-C. Chung, "Development of a hybrid rapid prototyping system using low-cost fused deposition modeling and five-axis machining," *J. Mater. Process. Technol.*, vol. 214, no. 11, pp. 2366-2374, 2014/11/01/ 2014, doi: <https://doi.org/10.1016/j.jmatprotec.2014.05.004>.
- [29] T. B. Thoe, D. K. Aspinwall, and M. L. H. Wise, "Review on ultrasonic machining," *International Journal of Machine Tools and Manufacture*, vol. 38, no. 4, pp. 239-255, 1998/03/01/ 1998, doi: [https://doi.org/10.1016/S0890-6955\(97\)00036-9](https://doi.org/10.1016/S0890-6955(97)00036-9).
- [30] J. Liu, D. Zhang, L. Qin, and L. Yan, "Feasibility study of the rotary ultrasonic elliptical machining of carbon fiber reinforced plastics (CFRP)," *International Journal of Machine Tools and Manufacture*, vol. 53, no. 1, pp. 141-150, 2012/02/01/ 2012, doi: <https://doi.org/10.1016/j.ijmachtools.2011.10.007>.
- [31] Q. Feng, W. L. Cong, Z. J. Pei, and C. Z. Ren, "Rotary ultrasonic machining of carbon fiber-reinforced polymer: feasibility study," *Machining Science and Technology*, vol. 16, no. 3, pp. 380-398, 2012/07/01 2012, doi: 10.1080/10910344.2012.698962.
- [32] W. Cong, Q. Feng, Z. Pei, T. Deines, and C. Treadwell, "Rotary ultrasonic machining of carbon fiber-reinforced plastic composites: using cutting fluid vs. cold air as coolant," *J. Compos. Mater.*, vol. 46, no. 14, pp. 1745-1753, 2012, doi: 10.1177/0021998311424625.
- [33] K.-i. Mori, T. Maeno, and Y. Nakagawa, "Dieless forming of carbon fibre reinforced plastic parts using 3D printer," *Procedia Engineering*, vol. 81, pp. 1595-1600, 2014.
- [34] G. W. Melenka, B. K. Cheung, J. S. Schofield, M. R. Dawson, and J. P. Carey, "Evaluation and prediction of the tensile properties of continuous fiber-reinforced 3D printed structures," *Compos. Struct.*, vol. 153, pp. 866-875, 2016.

Chapter 6 - Conclusions

Additive manufacturing (AM), or 3D printing, introduced a new revolutionary concept into the manufacturing industry and made producing complex products with customized features directly from a digital file a reality. Fiber reinforcement significantly improves the mechanical properties of 3D printed parts. It can be implemented in various AM techniques, such as FDM, SLA, SLS, LOM, and extrusion. However, most 3D printing methodologies of composite materials still facing major challenges need to overcome before becoming a mainstream manufacturing method. Void formation during printing, adhesion of fibers and polymer matrix, and challenges in continuous fiber printing are all amongst the existing issues in 3D printing of fiber composites that negatively impact the mechanical properties. Moreover, most of the commercial 3D printers designed for specific resins and introduction of fillers can lead to blockage, wear, non-adhesion, and increased curing times. In this work, a new approach for laser assisted AM of continuous fiber reinforced thermoplastic composites was developed with the motivation of increasing the mechanical properties of additively manufactured fiber reinforced polymer composites. This approach exhibits superior mechanical properties due to continuous fiber reinforcement, high fiber weight ratio, minimized void content, and superior interfacial bonding. In this technique, prepreg composites sheet containing continuous fiber reinforcement is the feedstock. The prepreg sheets are laser cut and laser bonded layer upon layer based on the CAD geometry to obtain the desired geometry. This novel approach was inspired by LOM and used for 3D printing of continuous carbon fiber reinforced thermoplastics (CFRTPs) by impinging prepreg composite sheets.

Glass and carbon fiber reinforced thermoplastics have been implemented in this study. The microstructure of these 3D printed composites were characterized by optical microscopy, scanning electron microscopy (SEM), and micro computed tomography (CT) scans. Superior consolidation of prepreg layers with minimal visible void or gap were observed in the additively manufactured composites. In this work, composite parts can be designed with varying fiber arrangements to meet the requirements of the particular application and the fiber alignment angle for each layer can be easily controlled. The interlayer properties of these materials were tested through various tests, such as T-peel test and lap shear test. In comparison to conventional manufacturing techniques, the interlayer bonding properties were decent and were fairly close to traditional methods. However, the interlayer properties achieved in this work is significantly better than existing AM technologies. In addition, mechanical properties, namely tensile and flexural properties, of bulk composites manufactured by our method is also excellent relative to the strongest 3D printed composites by other techniques. The excellent interfacial bonding strength and high volume ratio of continuous fiber contribute to the highest reported tensile strength of 668.3 MPa and flexural strength 591.16 MPa for our 3D printed carbon fiber composites. In addition, we developed a validated finite element (FE) model capable of predicting temperature distribution in the CFRTP structure during the laser bonding process. Temperature disturbing at the laminate interface is the primary factor in the bonding quality and the FE model could help modifying and optimizing this technique for various structural composites. The temperature profile obtained by the FE analysis were validated at various laser powers and printing speeds to ensure the accuracy of the model. The experimental data was captured using micro thermocouples embedded between layers during the AM process. During this laser assisted 3D printing technique, temperature at the material interface could reach well above the matrix melting point.

AM technologies in general suffers from poor surface quality and uncertain engineering quality. Mechanical finishing processes could concurrently solve these surface issues with the 3D printed composites components. We demonstrated CNC milling and rotary ultrasonic machining (RUM) as two mechanical finishing process to improve the surface finish of the additively manufactured composites. We also compared the surface quality results with FDM CFRTP parts before and after the finishing process. The surface roughness and surface morphology of the original unfinished and finished surfaces with various cutting depths are extensively studied to investigate the feasibility of the proposed finishing technique. A smooth, consistent, and predictable surface morphology is achieved for various surfaces and drilled holes, demonstrating a substantial improvement over the original 3D printed surfaces.

Finally, the AM technique explored in this dissertation is capable of scaling up to meet the demand of high volume productions in automotive, aerospace, marine, and construction industries and provide excellent rigidity, light weight, and versatility of design and material choice. It could also help automated the labor intensive composite manufacturing industry to bring down the cost of production and eliminate waste by streamlining the production. Overall, our proposed new method offer an alternative direction in AM of continuous fiber reinforced thermoplastic polymer composites to solve some of the fundamental issues associated with current techniques.

**Appendix A - Additional Micro CT Scans for continuous carbon
fiber reinforced PA6**

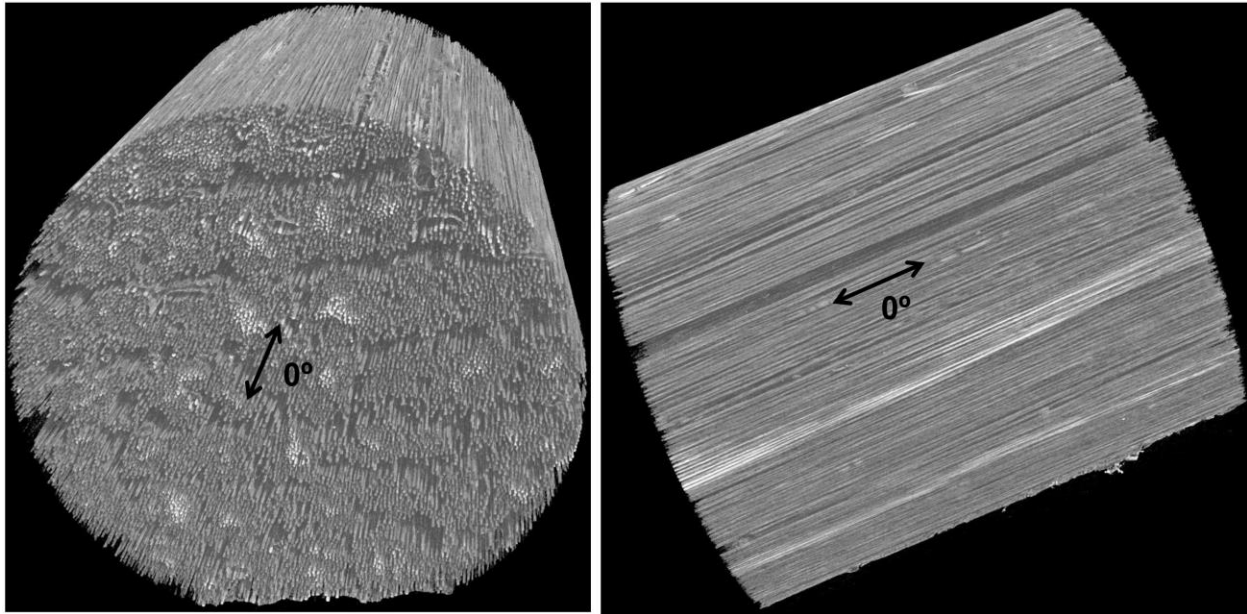


Figure A-1 3D illustration of continuous fiber reinforcement in the 3D printed unidirectional CFRTPs

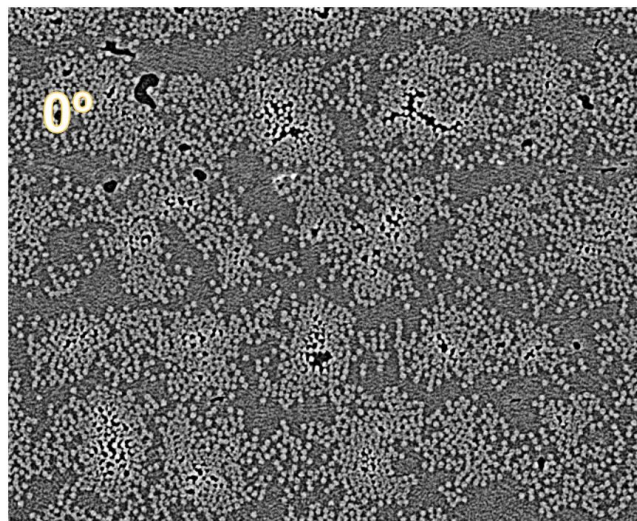


Figure A-2 Cross sectional CT scan of the 3D printed unidirectional CRTPs

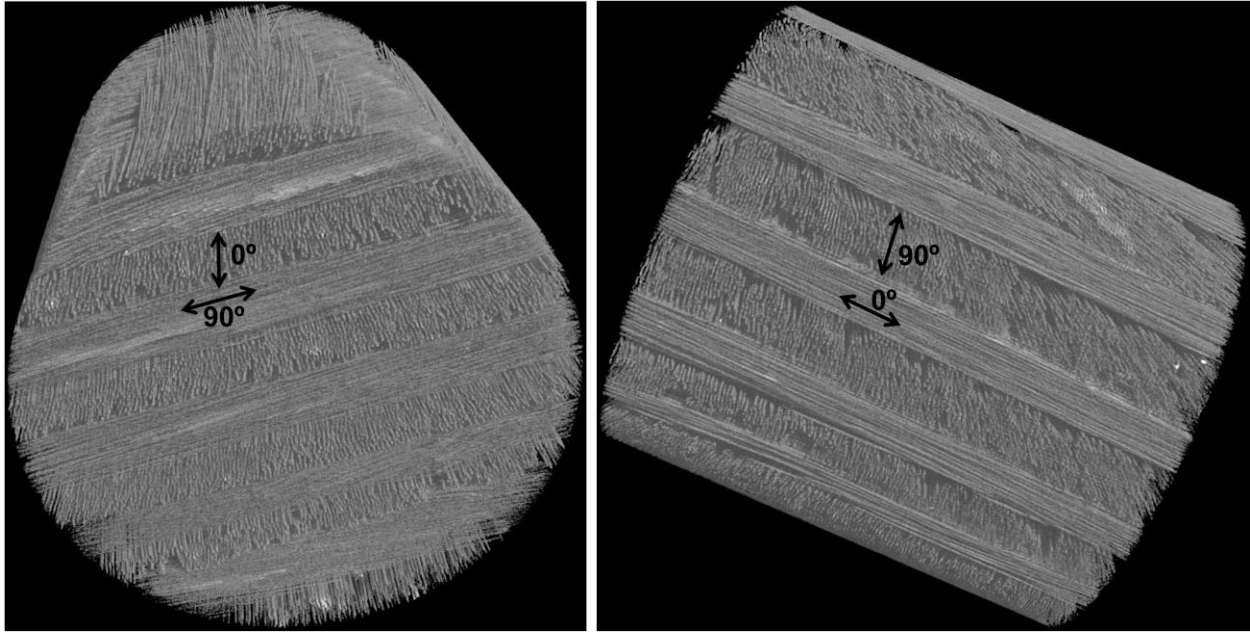


Figure A-3 3D illustration of continuous fiber reinforcement in the 3D printed cross-ply CFRTPs

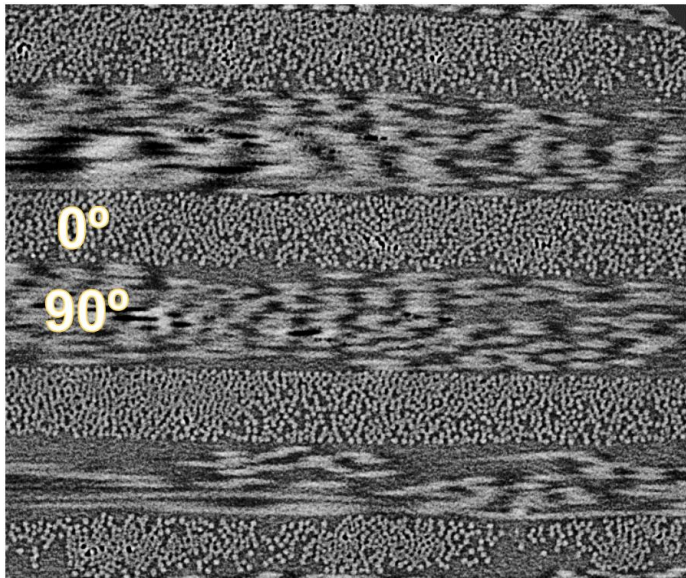


Figure A-4 Cross sectional CT scan of the 3D printed cross-ply CFRTP

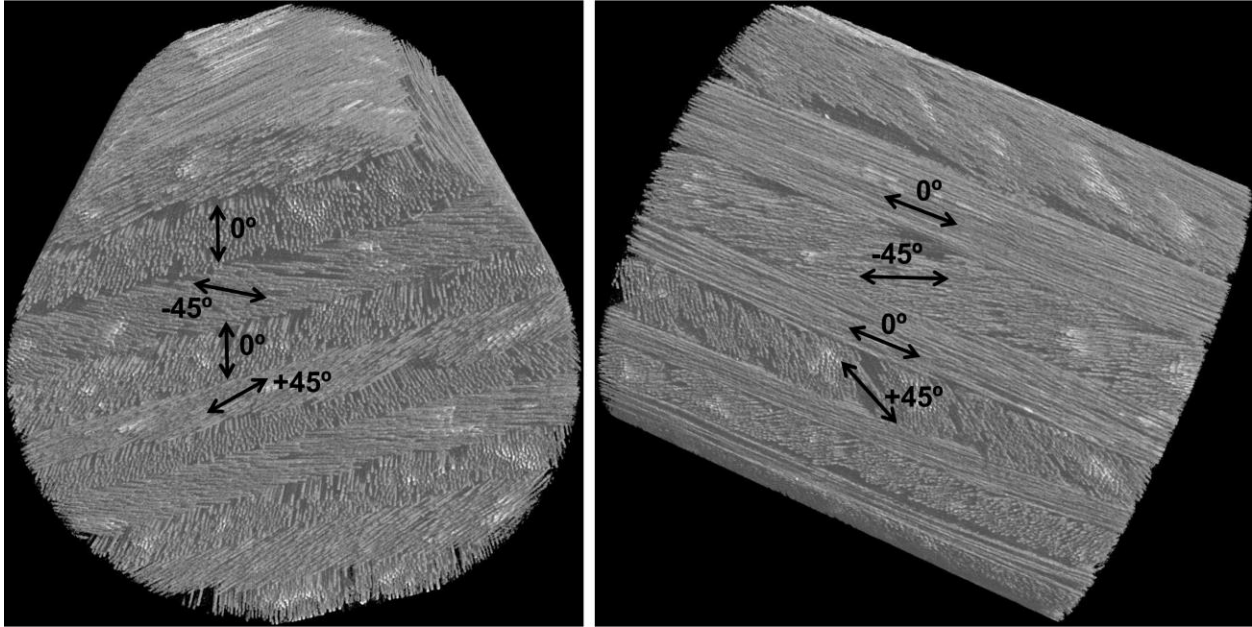


Figure A-5 3D illustration of continuous fiber reinforcement in the 3D printed $[0/-45/0/45]_s$ CFRTPs

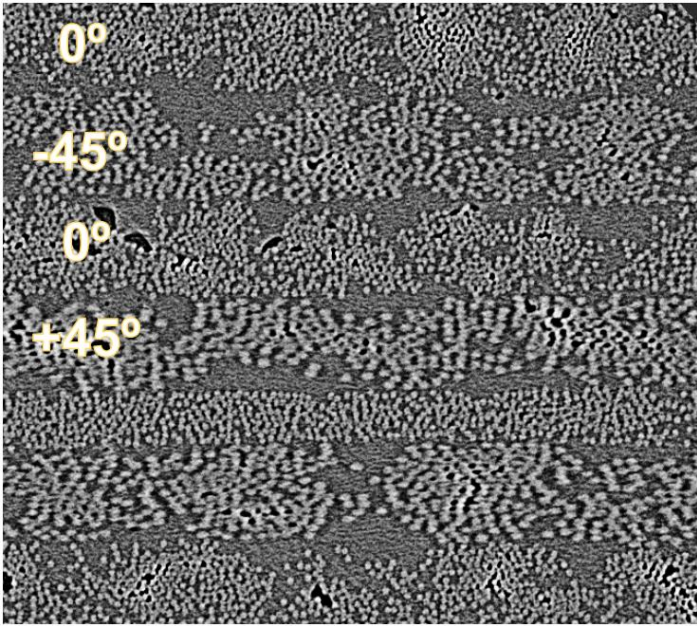


Figure A-6 Cross sectional CT scan of the 3D printed $[0/-45/0/45]_s$ CFRTPs

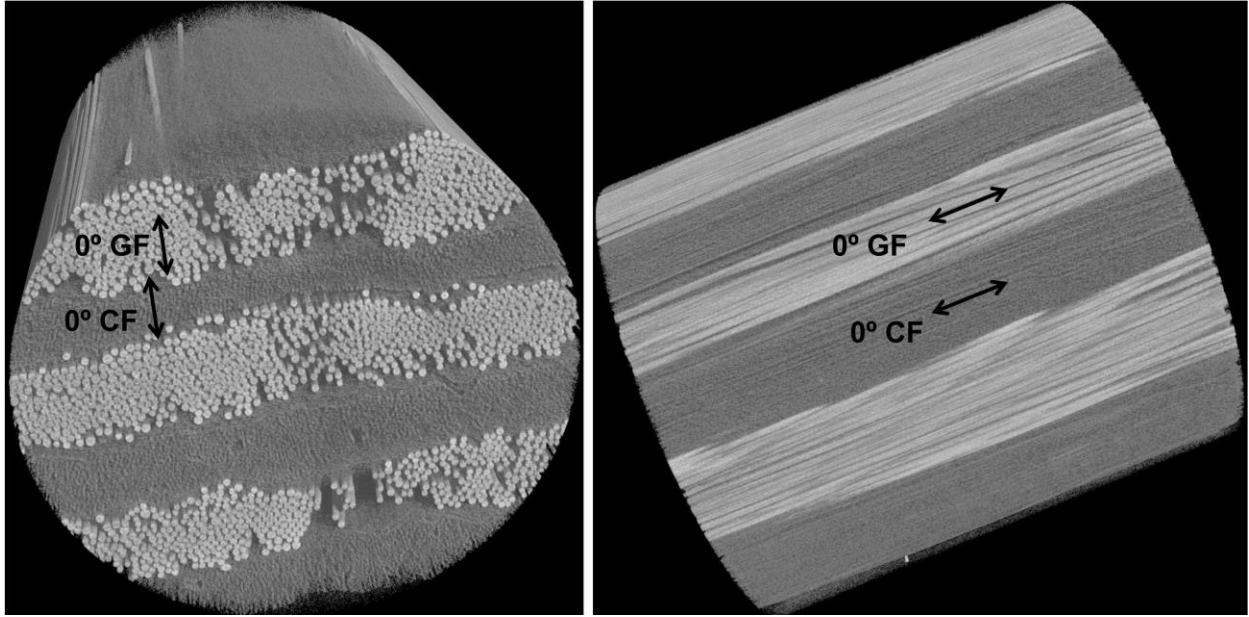


Figure A-7 3D illustration of continuous fiber reinforcement in the G-CF samples

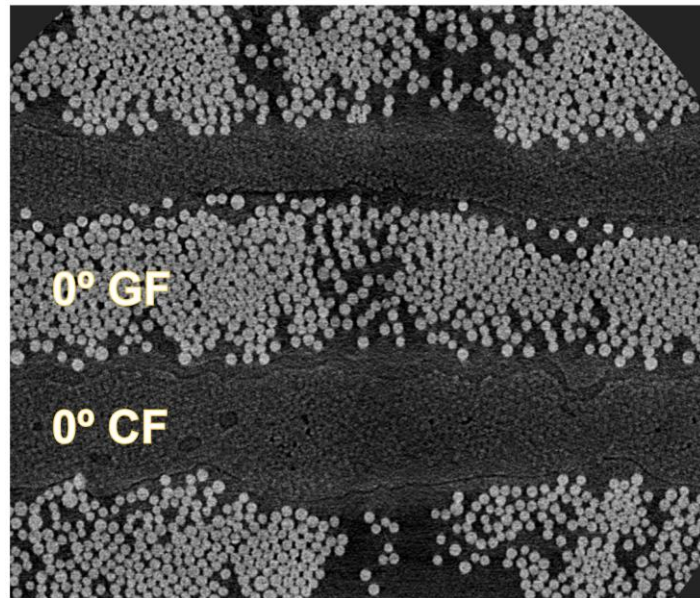


Figure A-8 Cross sectional CT scan of the G-CF samples